A Correlation-based Algebraic Transition Model for Flow over Rough Surfaces

by

Mehrdad NOEI YAZDIAN

THESIS PRESENTED TO ÉCOLE DE TECHNOLOGIE SUPÉRIEURE
IN PARTIAL FULFILLEMENT FOR A MASTER'S DEGREE
WITH THESIS IN MECHANICAL ENGINEERING
M.A.Sc.

MONTREAL, JANUARY 16, 2023

ÉCOLE DE TECHNOLOGIE SUPÉRIEURE
UNIVERSITÉ DU QUÉBEC

BOARD OF EXAMINERS

THIS THESIS HAS BEEN EVALUATED

BY THE FOLLOWING BOARD OF EXAMINERS

Mr. François Morency, Thesis Supervisor
Department of Mechanical Engineering, École de technologie supérieure

Mr. Patrice Seers, President of the Board of Examiners
Department of Mechanical Engineering, École de technologie supérieure

Mr. Giuseppe Di Labbio, Member of the jury
Department of Mechanical Engineering, École de technologie supérieure

THIS THESIS WAS PRESENTED AND DEFENDED

IN THE PRESENCE OF A BOARD OF EXAMINERS AND PUBLIC

ON DECEMBER 1, 2022

AT ÉCOLE DE TECHNOLOGIE SUPÉRIEURE

ACKNOWLEDGMENT

First, I would like to express my gratitude to my supervisor, professor François Morency, for providing guidance, feedback, and encouragement throughout my master's study. I could not have undertaken this journey without him, who generously provided knowledge and expertise.

I would like to show my deep appreciation to my mother, Fatemeh, for her continuous support and encouragement throughout my life. Despite the hundreds of kilometers separating us, I can always feel her presence. Also special thanks to my cousin and roommate, Arash, who made this path easier for me.

Finally, I would like to thank all my family and friends for their help at various stages of my life.

Un modèle de transition algebrique basé sur la correlation pour l'écoulement sur des surfaces rugueuses

Mehrdad NOEI YAZDIAN

RESUME

Le problème du givrage est l'un des défis de l'industrie aéronautique qui n'a pas été complètement résolu. Le givrage des aéronefs peut affecter la sécurité des vols de plusieurs façons. Lorsque l'avion subit du givrage, en raison de changements dans la forme et la rugosité de la surface, le coefficient de portance maximal, la vitesse de décrochage et la pente de la courbe de portance diminuent, tandis que la traînée augmente. Les surfaces rugueuses, telles que la glace, font que l'emplacement de départ de la transition se déplace vers l'amont et que l'écoulement devient turbulent à des nombres de Reynolds inférieurs. Étant donné qu'en écoulement turbulent l'effet, de refroidissement augmente considérablement par rapport à l'écoulement laminaire, il est important de localiser le début de la transition pour la simulation de l'accrétion de glace. Il existe plusieurs modèles de transition pour la moyenne de Reynolds des équations de Navier-Stokes; Cependant, ils sont principalement développés pour des surfaces lisses. Pour un développement ultérieur sur des surfaces rugueuses, le modèle de transition SA-BCM (Spalart-Allmaras Bas-Çakmakçıoğlu avec modifications) a été adopté. Le modèle de transition SA-BCM est classé comme un modèle algébrique ou à zéro équation car il utilise une fonction d'intermittence plutôt que de dériver des équations supplémentaires pour le transport d'intermittence. Le modèle sous-jacent du modèle de transition SA-BCM est le modèle de turbulence Spalart-Allmaras (SA) bien établi et validé. Pour détecter l'emplacement de début de transition, le terme de production de turbulence du modèle SA a été amorti avec une fonction d'intermittence jusqu'à ce qu'il satisfasse aux critères de début de turbulence en utilisant des corrélations empiriques. Tout d'abord, les résultats expérimentaux de la littérature sur une plaque plane rugueuse ont été utilisés comme référence pour développer le modèle SA-BCM afin de tenir compte de la rugosité de surface. Dans cette expérience, l'effet de différentes hauteurs de rugosité sur l'emplacement de début de transition à une vitesse d'écoulement libre constante a été étudié et documenté. La corrélation empirique mentionnée précédemment a été modifiée pour reproduire le même emplacement de transition que les résultats expérimentaux. Le modèle a été calibré par rapport à une plaque plane avec un gradient de pression nulle et

diverses hauteurs de rugosité de grain de sable équivalentes. Dans l'étape suivante, le profil aérodynamique NACA0012 a été choisi pour valider la corrélation de rugosité. La validation se fait en utilisant la même géométrie et deux nombres de Reynolds. Le modèle a pu définir le point de transition entre la région de transition par rapport aux résultats expérimentaux et autres résultats CFD. Cependant, il n'a pas été en mesure de prédire exactement l'emplacement du début de la transition et la fin de la région de transition.

Mots-clés: Rugosité, turbulence, SA-BCM, profil givré, transition laminaire/turbulente

A correlation based algebraic transition model for flow over rough surfaces

Mehrdad NOEI YAZDIAN

ABSTRACT

The problem of icing is one of the challenges in the aviation industry which has not been tackled completely. Aircraft icing can affect flight safety in many ways. When the aircraft undergoes icing, due to the changes in the shape and roughness of the surface, the maximum lift coefficient, critical stall speed and slope of the lift curve decrease, while the drag increase. Rough surfaces, such as ice, cause the transition onset location to move upstream and the flow becomes turbulent at lower Reynolds numbers. Since in turbulent flow, the cooling effect increases significantly compared to laminar flow, it is important to locate the onset of the transition for ice accretion simulation. Several Reynolds-averaged Navier-Stokes transition models exist; However, they were mostly developed over smooth surfaces. For further development over rough surfaces, the SA-BCM (Spalart-Allmaras Bas-Çakmakçıoğlu with Modifications) transition model was adopted. The SA-BCM transition model is classified as an algebraic or zero-equation model since it employs an intermittency function rather than deriving additional equations for intermittency transport. The underlying model for the SA-BCM transition model is the well-established and validated Spalart-Allmaras (SA) turbulence model. To detect the transition onset location, the turbulence production term of the SA model has been damped with an intermittency function until it satisfies a turbulence onset criteria using empirical correlations. First, the experimental results from literature over rough flat plate were utilised as a reference to further develop the SA-BCM model to account for surface roughness. In this experiment, the effect of different roughness heights on the transition onset location at a constant free stream velocity has been studied and documented. The empirical correlation mentioned previously has been modified to mimic the same transition location as the experimental results. The model was calibrated against a flat plate with a zero-pressure gradient and various equivalent sand-grain roughness heights. In the next step, the NACA0012 airfoil has been chosen to validate the roughness correlation. The validation is done using the same geometry and two Reynolds numbers. The model was able to set the transition point in

between the transition region compared to the experimental and other CFD results. However, it was unable to exactly predict the transition onset location and the end of the transition region.

Keywords: Roughness, turbulence, SA-BCM, iced airfoil, Laminar/turbulent transition

TABLE OF CONTENTS

Page

LIST OF TABLES

Page

LIST OF FIGURES

Page

LIST OF ABREVIATIONS

AoA	Angle of Attack
BC	Bas-Çakmakçıoğlu
CFD	Computational Fluid Dynamic
CFL	Courant–Friedrichs–Lewy
CPU	Central Processing Unit
DNS	Direct Numerical Simulation
FSTI	Free Stream Turbulence Intensity
IRT	Icing Research Tunnel
IWT	Icing Wind Tunnel
MPI	Message Passing Interface
MUSCL	Monotone Upstream-Centered Schemes for Conservation Laws
NASA	The National Aeronautics and Space Administration
NS	Navier-Stokes
OS	Orr-Sommerfeld
PDE	Partial Differential Equation
RANS	Reynolds Averaged Navier Stokes
SA	Spalart-Allmaras
SA-BCM	Spalart-Allmaras Bas-Çakmakçıoğlu with Modification
SST	Shear Stress Transport
SU2	Stanford University Unstructured
TI	Turbulence Intensity

LIST OF SYMBOLS

A_p	Projected area in the direction of the freestream velocity vector (m^2)
A_s	Windward surface area of the element seen by the flow (m^2)
c	Airfoil chord (m)
C_d	Drag coefficient
C_l	Lift coefficient
C_p	Pressure coefficient
C_f	Skin friction coefficient
d	Distance to the nearest wall (m)
E	Energy per unit mass ($^J/_{kg}$)
$\vec{F}^c$	Convective fluxes
$\vec{F}^v$	Viscous fluxes
H	Fluid enthalpy ($^J/_{kg}$)
k	Roughness height (m)
k_s	Equivalent sand-grain roughness height (m)
K	Turbulent kinetic energy
$\widetilde{K}$	Favre-averaged turbulent kinetic energy ($^J/_{kg}$)
L	Characteristic linear dimension (m)
Ma	Mach number
P	Static pressure (Pa)
Pr_d	Dynamic Prandtl number

Pr_t	Turbulent Prandtl number
r_0	Mean distance between roughness elements (m)
R	Gas constant for air ($287.06\ {}^{J}/_{kg\ K}$)
Re	Reynolds number
Re_θ	Momentum thickness Reynolds number
$Re_{\theta c}$	experimental transition onset critical momentum thickness Reynolds number
$Re_{\theta v}$	Vorticity Reynolds number
$Re_{\theta c,rough}$	Rough transition onset critical momentum thickness Reynolds number
Re_k	Roughness Reynolds number
Re_{ks}	Equivalent sand-grain roughness Reynolds number
$\widetilde{S_{ij}}$	Favre-averaged strain rate
Su	Sutherland temperature ($273\ K$)
T	Temperature (K)
T_{ref}	Reference temperature (K)
Tu_∞	Free stream turbulence intensity
y^+	Nondimensional wall distance
γ	Specific heat ratio $\gamma = {}^{C_p}/_{C_v}$
δ_{ij}	Kronecker delta function
κ	Von Karman constant (0.41)
λ	Roughness shape parameter
μ_{dyn}	Dynamic viscosity (${}^{N\ s}/_{m^2}$)

μ_{ref}	Reference dynamic viscosity ($^{N\ s}/_{m^2}$)
μ_{tot}	Total viscosity ($^{N\ s}/_{m^2}$)
μ_T	Eddy viscosity ($^{N\ s}/_{m^2}$)
ν	Laminar kinematic viscosity ($^{m^2}/_{s}$)
ν_L	Kinematic molecular viscosity ($^{m^2}/_{s}$)
ν_{tur}	Turbulent kinematic viscosity ($^{m^2}/_{s}$)
$\hat{\nu}$	Eddy viscosity variable
ρ	Density ($^{kg}/_{m^3}$)
σ	Adaptive dissipation function
τ_{ij}	Viscous stress ($^{N}/_{m^2}$)
τ_w	Wall shear stress ($^{N}/_{m^2}$)
υ	Velocity ($^{m}/_{s}$)
υ_∞	Free stream velocity ($^{m}/_{s}$)
χ_1	Calibration constant
χ_2	Calibration constant
Ω	Vorticity

INTRODUCTION

This chapter provides an overview of aircraft icing and the problems it causes, as well as the accidents that result from it. In addition, some recent advances in icing simulation are briefly discussed. Finally, the research objective and outline are presented.

Aircraft icing

The problem of icing is one of the challenges in the aviation industry which has not been tackled completely. Ice accretion on the surfaces of an aircraft flying in icing conditions is referred to as aircraft icing (Cao, Tan & Wu, 2018). Aircraft icing can affect flight safety in many ways. When the aircraft undergoes icing, due to the changes in the shape and roughness of the surface, the maximum lift coefficient and slope of the lift curve decrease, while the drag and critical stall speed increase. If the cockpit crew does not pay attention to differences in airspeed and climb rate at this point, the plane may be nearing the stall boundary (Cole & Sand, 1991). Additionally, asymmetric icing can cause rolling movement of the aircraft and make it impossible to control it and leads to an accident. Figure 0-1 shows the formation of the ice on the wing's leading edge.

Figure 0-1 Ice formation on the wing's leading edge
Taken from AOPA (2008)

The ATR-72 crash in 1994 is an example of an icing accident. The plane experienced a serious icing situation. The combination of the electric heating de-icing system at the leading edge of the wing and natural circumstances created an ice ridge on the second half of the wing, resulting in a negative pressure zone on one side of the aileron. The negative pressure zone caused an automatic deflection of the aileron during a normal maneuver, causing the plane to lose control, roll, capsize, and crash (Cao et al., 2018). From a statistical point of view, between 1990 and 2000, icing was responsible for 12% of all weather-related crashes (AOPA, 2008). Furthermore, several serious incidents were reported in the four years between 2010 and 2014, according to the National Safety Transportation data. A total of 78 lives were lost in the 52 accidents that were documented (AOPA, 2008). As a result, it's critical to research and understand the impacts of icing on aircraft surfaces so that the problem can be dealt with effectively.

There are three main methods for evaluating the effects of ice accretion on aircraft surfaces: flight testing, wind tunnel testing, and numerical modeling. The most trustworthy iced-aircraft aerodynamic data comes from flight testing, but it comes at a considerable price (Cao, Wu, Su & Xu, 2015). NASA's tests on the DHC-6 twin otter aircraft provide the most complete flight data (Cao et al., 2018). Figure 0-2 shows the aircraft used by NASA. The aircraft's performance was examined in detail under various icing situations and with various ice shapes, and the aerodynamic derivatives were derived using the modified maximum likelihood estimate technique and modified stepwise regression (Ratvasky & Ranaudo, 1993).

Figure 0-2 NASA icing research aircraft
Taken from Reehorst et al. (2005)

Icing wind tunnels such as the IRT wind tunnel at NASA Glenn Center and the IWT wind tunnel in Italy offer reliable results at lower costs. However, since it's difficult to build an icing wind tunnel, simulated ice shapes are frequently utilized, which affects the accuracy of the results (Tagawa, 2021). Computational Fluid Dynamics (CFD) has grown in popularity in recent decades, and it is increasingly being used in multidisciplinary design and analysis of aerospace products (Spalart & Venkatakrishnan, 2016).

In numerical simulations, ice surfaces are treated as rough surfaces. To study roughness, there are some questions that need to be answered. To begin, there's the issue of characterizing the roughness itself: its height, width, shape, uniformity, and so on (Langel, Chow, Van Dam & Maniaci, 2017). Next, roughness has to be defined clearly since nothing is truly smooth from the microscopic point of view. Finally, one should decide what effects need to be studied. In the current study, roughness is referred to the uniform obstacles which the flow faces over the surfaces of the flat plate and airfoil. The feature that has been studied in this research is the effect of the roughness height on the transition onset location. The motivation behind the current work is that the flow is laminar, but the presence of ice causes a rapid transition to turbulence and in turbulent flow, the cooling effect and heat transfer change significantly. Therefore, it is important to locate the transition point to improve the heat transfer prediction needed for the calculation of ice accretion. A transition model, which has been coupled with a

turbulence model, is chosen and the effect of the roughness height on the transition point has been implemented into the transition model using the available experimental data as the reference. Similar to the underlying transition model, the sharp rise of the skin friction coefficient is used as the guide to locate the start of the transition point. In the current work, the effect of the roughness on the flow characteristic after the transition point is not studied. However, enabling a transition model to take the roughness into account make it possible to couple the current study with a fully turbulent model, which takes the roughness into account, such as the work of (Tagawa, Morency & Beaugendre, 2018).

Thesis outline

This thesis is divided into three chapters. In chapter one, a literature review is presented. It starts by explaining the transition process and the Reynolds experiments. An overview of the literature including the natural, bypass, and other paths from laminar to turbulent flow is given. Then, it is continued by presenting seventeen related transition models, and the advantages and weaknesses of each model are discussed. After that, the effect of isolated and distributed roughness on the transition process is presented. Finally, eight of the currently available roughness models are discussed.

Chapter two presents the methodology used in this research to extend the use of a transition model over rough surfaces. This chapter holds six main sections starting with the presentation of the Reynolds-Averaged Navier Stokes (RANS) equations. In the second step, the mathematical model used for the Spalart-Allmaras (SA) turbulence model is shown. Next, the modifications to the SA model in order to implement the transition onset correlation are presented. This is then followed by our proposed model to extend the transition model over the rough surfaces. Then, SU2 as our flow solver is introduced and finally, the numerical model used in this study is presented.

Chapter three presents the results. In each section and before presenting the results, the computational domain is presented to show the problem with the related boundary conditions.

Moreover, a mesh study is performed to find out the relative error using different mesh sizes from the coarsest to the finest. The chapter starts by presenting the results of the model calibration against a flat plate. After that, the validation of the model is done over the NACA 0012 airfoil at two Reynolds numbers.

CHAPTER 1

LITERATURE REVIEW

A review of the literature is given in chapter one. The transition process and the Reynolds experiments are explained at the beginning. A summary of the literature is provided, including the natural, bypass, and further ways from laminar to turbulent flow. Seventeen similar transition models are then addressed, and the advantages and disadvantages of each model are discussed. Following that, a presentation of the impact of isolated and distributed roughness on the transition process follows. Finally, eight of the roughness models that are currently available are discussed.

1.1 Transition process

The study of the transition process started in 1883 with the Reynolds experiments. He observed that the streak of colour stretched in a straight line across the tube when the velocity was low enough (figure 1-1). Additionally, he reported that as the velocity was raised in incremental steps, the colour band would mix up with the surrounding water at some point in the tube and fill the rest of the tube with a mass of coloured water (figure 1-2). The Reynolds number has been constructed as a result of his experiments which is a relation between flow velocity, density, viscosity, and characteristic length (Reynolds, 1883).

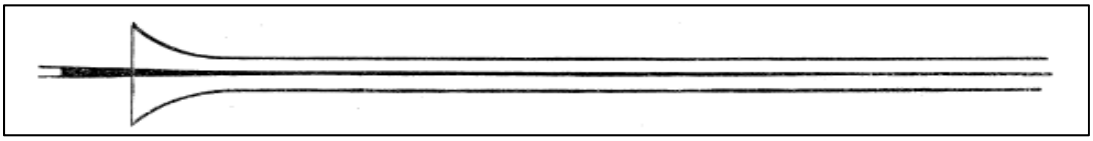

Figure 1-1 Streak of colour in a tube at low velocity
Taken from Reynolds (1883)

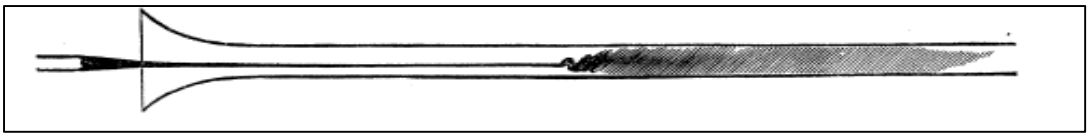

Figure 1-2 Mix of colour and water in a tube
Taken from Reynolds (1883)

The Navier-Stokes (NS) equations, as well as the mass and energy conservation equations, are the fundamental equations in fluid dynamics. A complete analytical solution is basically unachievable due to the system's complexity. In order to analyse the boundary layers, incompressibility and locally parallel flow are frequently simplified. The Orr-Sommerfeld (OS) equation is obtained by applying linear stability analysis methods to the simplified NS equations (Langel et al., 2017).

Around the start of the twentieth century, Lord Rayleigh researched the inviscid OS equation thoroughly and established that a laminar boundary layer should stay stable unless there is an inflection in the velocity profile (Rayleigh, 1879). In 1904, Prandtl indicate the effect of viscosity on transition and formed the boundary layer theory (Prandtl, 1904). Until the experiment of Schubauer and Skramstad in 1947, the destabilising impact of viscosity and the existence of wave-like disturbances causing transition were contested. They concluded that the velocity changes caused by a wave traveling downstream through the boundary layer are known as laminar boundary-layer oscillations. A vibrating object in the boundary layer, such as a vibrating ribbon, or disturbances from the outside, such as stream turbulence and sound, can cause the wave to form. When the amplitude is large enough, a wave in the boundary layer creates a disturbance that causes transition on a flat plate with zero pressure gradient. Transition can also be caused by a sufficiently large random disturbance. Additionally, it has been concluded that boundary-layer oscillations might be caused by internal as well as exterior disturbances, such as surface imperfections. A randomly distributed small roughness may produce effects similar to mild turbulence in an air stream (Schubauer & Skramstad, 1947).

Figure 1-3 illustrates the natural transition stages which have been shown schematically by Schlichting in 1968. He claimed six stages for the natural transition of the flow from laminar

to turbulent over the flat plate. First, the flow is stable and laminar until it reaches the leading edge of the plate. In the next step, the Tollmien-Schlichting waves start to appear. Next, unstable, laminar, three-dimensional waves are developed. Followed by the turbulence bursts at places with high local vorticity. In the next step, turbulent spots are formed at zones with large turbulent velocity fluctuations which leads to a fully developed turbulent boundary layer (Schlichting, 1968). If the freestream turbulence intensity is relatively low ($< 1\%$), the natural transition process occurs. In highly turbulent environments or in the presence of external forcing factors such as surface roughness, one or more of the early stages might be skipped, result in forming the secondary instabilities without the amplification of Tollmien-Schlichting waves (Langel et al., 2017).

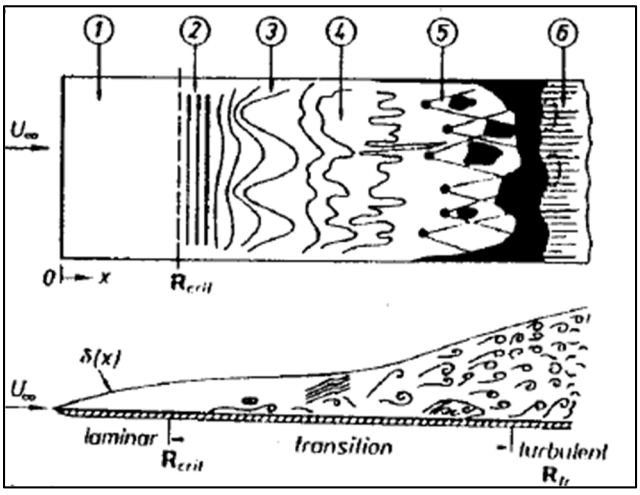

Figure 1-3 Stages of natural transition process
Taken from Schlichting (1968)

In 1969, Morkovin has introduced a term called receptivity to the transition procedure (Morkovin, 1969). This part of the transition process explains how the external disturbances such as sound or vorticity are transformed into a flow perturbation. It establishes the initial conditions for breakdown of the laminar flow (Morkovin, 1994). Figure 1-4 illustrates the boundary layers transition, qualitatively. The initial amplitude grows schematically from left to right in Figure 1-4. These disturbances may be too small to detect at first, and they are only detected after the onset of an instability. A number of instabilities can arise independently or

simultaneously, and the occurrence of any given form of instability is dependent on Reynolds number, wall curvature, roughness, and initial conditions. If weak disturbances are introduced into Figure 1-4 and path A is taken, the initial growth of these disturbances is explained by the linear stability theory of primary modes. Secondary instabilities emerge as the amplitude increases, resulting in three-dimensional and nonlinear interactions. At this stage, the disturbance grows quickly and breaks down into turbulence (Saric, Reed & Kerschen, 2002). When freestream disturbances are strong enough, linear disturbances are bypassed (Morkovin 1969 & 1994), and turbulent spots or subcritical instabilities form, the flow becomes turbulent rapidly. Although the phenomenon is not fully understood, it has been reported in cases of roughness and high freestream turbulence, and it corresponds to path E in Figure 1-4 (Saric et al., 2002).

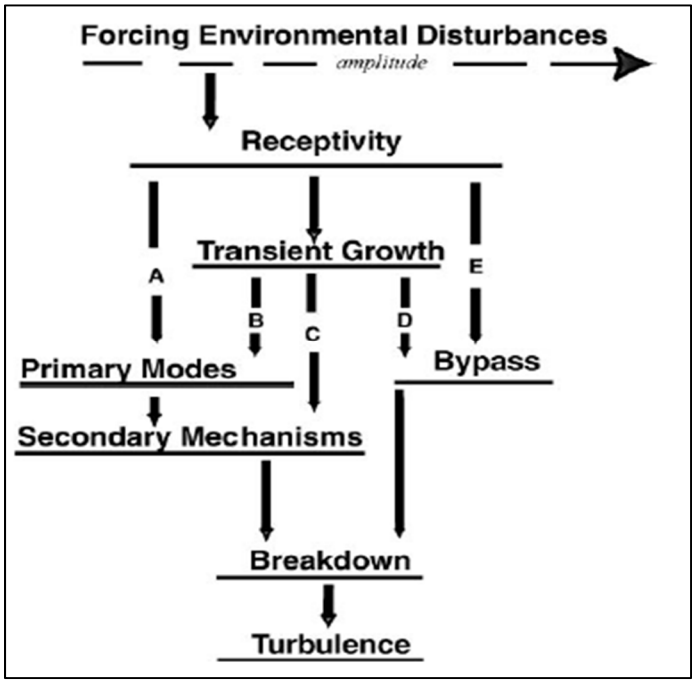

Figure 1-4 The paths from receptivity to turbulence
Taken from Saric et al. (2002)

When two nonorthogonal stable modes interact, they grow algebraically and then decay exponentially, resulting in transient growth. When the boundary layer is given with appropriate initial conditions, studies have demonstrated that large amplitudes can be achieved through

transient growth. As a result, the range of initial conditions is determined by receptivity. Transient growth can lead to spanwise modulations of two-dimensional waves (way B), direct distortion of the fundamental state that leads to secondary or subcritical instabilities (path C), or direct bypass (path D), depending on amplitude (Saric et al., 2002)

1.2 Transition prediction models

This section is devoted to describe three kinds of transition models in the literature. It is divided into three sub-sections including transition models based on linear stability, correlation-based transition models, and transition models compatible with CFD. Since the transition models should rely only on local variables and also not be restricted to only 2-D geometries, the last sub-section presents the models which meet the requirements for implementation into fully parallel 3-D RANS codes.

1.2.1 Transition models based on linear stability

In 1956, Van Ingen suggested a model, called e^N, which was restricted to two-dimensional and incompressible flow based on the boundary layer stability theory. The model was calibrated against a flat plate by calculating the amplification of unstable oscillations in the boundary layer and comparing the results with the experimental determinations of the transition region. Validation of the model was done over EC 1440 airfoil and in some cases, the same amplification ratio at transition was found as for the flat plate. However, differences exist, and the author concluded that these differences might be due to the lack of sufficient numerical results of the stability theory (Van Ingen, 1956). In the same year, Smith and Gamberoni, investigated a method for predicting transition that was founded on the theory of boundary layer stability. They discovered a strong correlation between experimental results with this theory. The e^N method is predicting the transition onset by assuming that the most unstable Tollmein-Schlichting wave in the boundary layer has grown by some factor usually

taken to be e^9. The correlation is then used to predict transition for a variety of flows in wind tunnels and in flight and the predictions are reported to agree well with the experiment.

The "full" e^N method is when the growth rate is directly calculated by the Orr-Sommerfeld equation. Because numerically solving the OS equation is computationally costly, certain simplifying assumptions must be made in the majority of implementations. In the "envelope" version of the e^N method, the maximal amplification ratio for each particular frequency as interpolation points for an approximate curve is used (Langel et al., 2017). In 1987, a linear envelope version of the e^N method was developed by (Drela & Giles, 1987) to compute disturbance growth rates given the kinematic shape factor (H_k) and momentum thickness Reynolds number (Re_θ).

Using a database to determine the amplification rates is an alternative to the envelope e^N method simplifications. In 2007, Mayda created a database of disturbance growth rates based on Mach number at the boundary layer edge, kinematic shape factor (H_k), displacement thickness Reynolds number ($Re_{\delta*}$), and disturbance frequency. He then used the RANS code ARC2D to implement an interpolation approach for this database. The developed database model has been tested on a variety of real-world problems such as steady and unsteady airfoils and the predictions agreed well with the experimental data (Mayda, 2007).

Although extremely effective in 2-D configurations, the extension to 3-D is one of the most major difficulties for an e^N type method. Much of the boundary layer analysis is naturally limited to two dimensions, and while specific flows may be simplified to two dimensions, creating a generalised formulation is extremely difficult. Another limitation is the dependency on integral boundary layer quantities, which makes it difficult to employ with parallel computing (Langel et al, 2017).

1.2.2 Correlation based transition models

Correlation-based models are based on the idea that certain local properties may be utilised to approximate the relative stability of the boundary layer at a given location. The momentum thickness Reynolds number, Re_θ, is used in most correlation-based transition models. The transition onset momentum thickness Reynolds number, $Re_{\theta t}$, is defined by a transition prediction model as the value at which the laminar boundary layer begins to transition. Figure 1-5 shows the behavior of the momentum thickness Reynolds number (Langel et al., 2017).

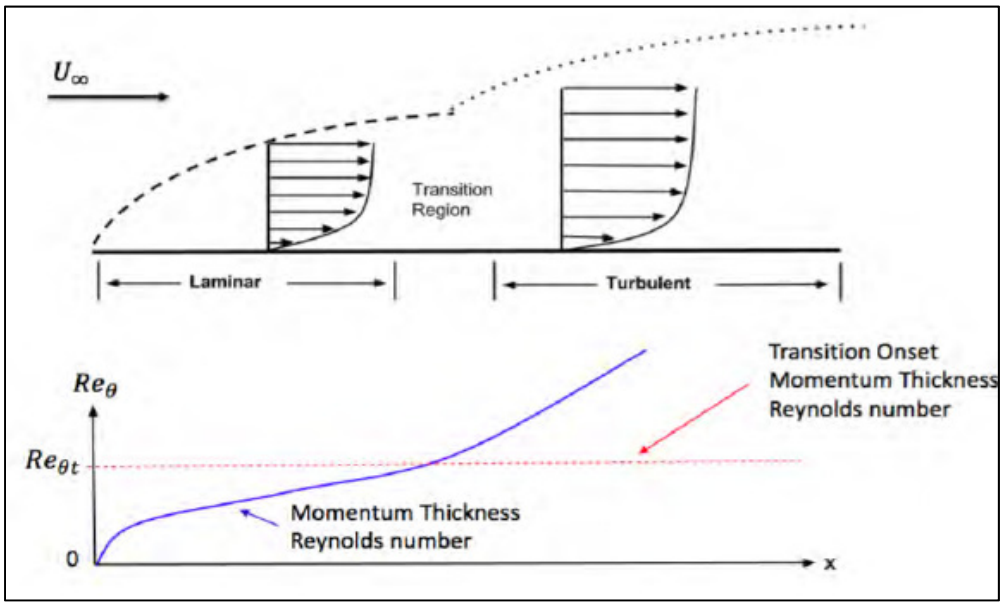

Figure 1-5 Sketch of the momentum thickness Reynolds number behavior
Taken from Langel et al. (2017)

In 1991, Mayle introduced a simple correlation which was a direct relationship between free stream turbulence intensity and $Re_{\theta t}$. He came to the conclusion that the freestream turbulence intensity, the periodic unsteady effects of wakes and shock waves, and whether the acceleration is more or less than that for reverse transition determine the onset of transition in gas turbines. Additionally, he concluded that the length of the transition in gas turbines is solely determined by freestream turbulence and pressure gradient (Mayle, 1991).

A more complete correlation has been introduced by Abu-Ghannam and Shaw which includes the pressure gradient in addition to the free stream turbulence intensity (Abu-Ghannam &

Shaw, 1980). Figure 1-6 illustrates the behavior of these correlations over the zero-pressure gradient flat plate along with the experimental data. Free stream turbulence intensity is shown in the X direction and the momentum thickness Reynolds number associated with the onset and the end of the transition is plotted in the Y direction. Curve number 1 shows the correlation between the onset of the transition point and the free stream turbulence intensity. Curve number 2 presents the correlation between the end of the transition and the free stream turbulence intensity. Curve number 3 is provided to compare the Abu-Ghannam and Shaw correlation (curve 2) with the previous correlation of (Hall & Gibbings, 1972) which was based on the limited amount of experimental data. One should notice the rapid changes in the momentum thickness Reynolds number at lower turbulence intensity values. It has to be mentioned that turbulence intensity is typically an input by the user in flow simulations. Small changes in entering this value can leads to a completely different result.

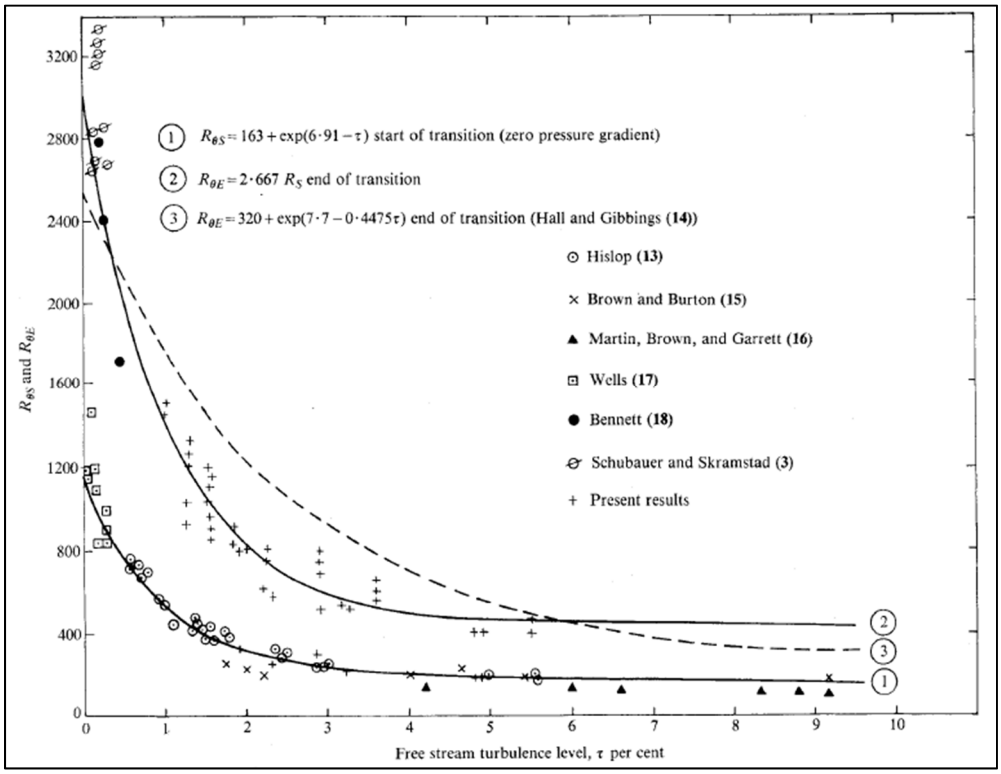

Figure 1-6 $Re_{\theta t}$ against free stream turbulence intensity
Taken from Abu-Ghannam & Shaw (1980)

The above-mentioned correlations predict the onset of the transition. To predict the transition evolvement, Dhawan and Narasimha introduced an intermittency function based on the flat plate experiment (Dhawan & Narasimha, 1958). Since the distance from the transition point has been included in the function, it was difficult to implement the model into CFD code. Steelant and Dick used this correlation and developed a model which includes a transport equation for the intermittency factor. The turbulent spot growth rate is represented by the source term in this equation, which is dependent on the acceleration parameter and the turbulence level (Steelant & Dick, 1996).

Many attempts have been made to develop a transition model that includes a correlation for both the onset and the extent of transition. Cho and Chung proposed a set of equations for kinetic energy, k, the dissipation rate, ε, and the intermittency factor, γ. This helped to apply the intermittency effect in the $k-\varepsilon$ turbulence model (Cho & Chung, 1992). In 2000, Suzen and Huang combined the Steelant and Dick and Cho and Chung models to propose a new transport equation for intermittency factor which was capable of reproducing the intermittency factor in streamwise and cross-stream directions. This model is coupled with the SST turbulence model to obtain the eddy viscosity (Suzen & Huang, 2000). Although both of the above-mentioned models can successfully predict the transition process, the need to calculate the momentum thickness Reynolds number and comparing it with the critical momentum thickness Reynolds number make them dependent to nonlocal data which is incompatible with general purpose of CFD codes (Çakmakçıoğlu, Bas & Kaynak, 2018).

1.2.3 Transition models compatible with CFD purpose

The computational cost of solving the RANS equations on large computational grids drives the urge to maintain compatibility in parallel codes. Models must rely on the local parameters to be compatible with parallel codes. A single CPU is insufficient in many applications to provide a solution in a realistic time period. Quantities such as the boundary layer edge, as well as the directly calculated momentum and displacement thickness, are difficult to compute in a

parallel environment since the grid topology does not clearly reveal the direction and bounds of the integration. Additional line searches or other auxiliary computations must be conducted, potentially across many CPUs, and information must then be transmitted throughout the domain. This not only wastes CPU time from the computations, but it also has the potential to generate a bottleneck for the global iteration (Langel et al., 2017). In this section, some of the well-known transition models are presented briefly. These models are depending on local variables and are compatible with 3-D geometries.

(Walters & Leylek, 2004) developed a two-equation transition model which employs the local variables to predict the boundary layer transition. This model is developed based on the laminar-kinetic-energy, k_L model which has been first proposed by (Mayle & Schulz, 1997). This technique incorporated two fundamental principles. The first is the use of a novel transport equation to represent the development of nonturbulent, streamwise variations in the pre-transitional boundary layer. The second step is to incorporate fluctuation increase caused by a splat mechanism. The model has been validated against two test cases including a flat heated wall with free stream turbulence intensity raising from 0.2 to 6% and a turbine stator vane with Free stream turbulence intensity ($FSTI$) from 0.6 to 20% (Walters & Leylek, 2004). Walters and Cokljat improved the above-mentioned method in order to overcome the issues regarding complex flow conditions and the attached boundary layer transition to exhibit nonphysical sensitivity to the freestream turbulence length scale. The third transport equation is used to predict the magnitude of low-frequency velocity variations in the pre-transitional boundary layer, which have been identified as transition precursors. The model term closure is based on a physics-based rather than solely empirical approach. It has been applied to the flat plate with and without pressure gradient and different airfoil geometries with different Reynolds numbers, $FSTI$s, and angles of attack (Walters & Cokljat, 2008).

Langtry and Menter developed a correlation-based transition model called $\gamma - \widetilde{Re}_{\theta t}$ which is the most widely used 3-D RANS compatible transition model based on (Langel et al., 2017). The model is solving two equations in addition to the base $k - \omega$ turbulence model, one for the intermittency and one for the transition location. In this model, the vorticity Reynolds

number, Re_v, is used (Langtry & Menter, 2009). Studies have shown the relation between Re_v and momentum thickness Reynolds number, Re_θ, with less than 10% error for moderate pressure gradient (Menter & Langtry, 2004. Wilcox, 1993. Menter, Esch & Kubacki, 2002). The model's weaknesses are cross-flow instability and the transition correlations being non-Galilean invariant (Langtry & Menter, 2009).

Medida used the $\gamma - \widetilde{Re}_{\theta t}$ concept and recalibrated the transport equations for Spalart-Allmaras (SA) turbulence model. Since the SA model is a one-equation turbulence model, solving one fewer transport equation is an advantage of the $\gamma - \widetilde{Re}_{\theta t} - SA$ model over the original $\gamma - \widetilde{Re}_{\theta t}$. The model was first calibrated against the zero-pressure gradient flat plate and then validated over a variety of airfoil geometries and Reynolds numbers (Medida, 2014). Although the model is giving the same results as the original $\gamma - \widetilde{Re}_{\theta t}$ model, it cannot be considered a new transition model. It can be considered as an extension to the $\gamma - \widetilde{Re}_{\theta t}$ transition model (Langel et al., 2017).

Menter et al. further developed the $\gamma - \widetilde{Re}_{\theta t}$ model in 2015. In the new γ transition model, only one transport equation for the intermittency is solved which is one of the advantages of the γ model over the $\gamma - \widetilde{Re}_{\theta t}$ model in terms of computational cost. Additionally, unlike the $\gamma - \widetilde{Re}_{\theta t}$ model, the γ transition model is Galilean invariant, and it can be applied to the problems which move relative to the coordinates system (Menter et al., 2015).

(Çakmakçıoğlu et al., 2018) introduced a correlation-based algebraic transition model named B-C. Since this model is not solving any transport equation for intermittency nor transition onset location, it is referred to as a zero-equation (algebraic) transition model. The idea behind this model is to dampen the turbulence production in the underlying turbulence model until it reaches the transition point. After the transition point, the damping function will be disabled and will let the flow to be solved fully turbulent. The Spalart-Allmaras turbulent model has been chosen by the authors as the base model. One of the advantages of this model over the $\gamma - \widetilde{Re}_{\theta t}$ is the computational cost which is lower in the SA-BC model. First, the model is calibrated against the zero-pressure gradient flat plate test case of Schubauer and Klebanoff

and then validated against other flat plate test cases with different Reynolds numbers and $FSTI$s. Additionally, this model was successfully validated over Eppler E387 airfoil, T106 turbine cascade, and DLR-F5 wing. The model is using the local variables to predict the transition onset location (Çakmakçıoğlu et al., 2018). However, using the velocity to calculate one of the variables made it non-Galilean invariant. Additionally, the implementation of one of the calibration constants into the flow solver was different from the article. The inclusion of the freestream Reynolds number might make the model dependent on the arbitrary reference length. To overcome these shortcomings, the B-C model name has changed to SA-BCM and one of the calibration constant definition has changed. The model has been recalibrated against the zero-pressure gradient flat plate (Mura & Çakmakçıoğlu 2020). Since the SA-BCM model is the baseline of the current study, the mathematical model is presented in detail in chapter two.

1.3 Roughness effect on transition process and boundary layer

The effect of roughness on laminar-turbulent transition has been studied for decades. Generally, surface roughness causes the flow to transition from laminar to turbulent at lower Reynolds numbers. Additionally, it affects the fully turbulent boundary layer. It has been observed that roughness increases the turbulence fluctuations and kinetic turbulent energy in a fully developed turbulent boundary layer (Dryden, 1958). Early transition and modifications to an airfoil's fully turbulent boundary layer can increase drag, modify stall characteristics, change the lift-curve slope, and even cause the flow to become unsteady (Langel et al., 2017). Roughness elements below the viscous sublayer's height have little impact on the transition process since the disturbances are dissipated due to the high levels of viscous damping (Merkle & Kubota, 1973). Roughness heights are often nondimensionalized in terms of displacement thickness (k/δ^*) or defined using a roughness Reynolds number (Re_k). Roughness has been divided into two distinct categories. A single hemisphere, cylinder, or other three- or two-dimensional form is an example of isolated roughness. There's also distributed roughness,

which is a three-dimensional occurrence that includes any form of a clustered group of roughness elements (Langel et al., 2017).

1.3.1 Isolated roughness

Two-dimensional roughness creates pockets of divided flow both downstream and upstream of the rough element (Langel et al., 2017). The downstream separation can go far beyond the trip strip or other isolated 2-D feature's location. The inflection in the velocity profile caused by the flow separation results in an inviscid Rayleigh instability. 2-D isolated roughness, although creating a significant disturbance, does not instantly introduce turbulent areas into the boundary layer, but rather increases the amplification of naturally occurring Tollmien-Schlichting waves (Klebanoff & Tidstrom, 1972). By increasing the momentum deficit downstream of the roughness, the separated region increases receptivity to external disturbances such as freestream turbulence and sound pulses. A 2-D isolated feature might thus enhance the possibility of a bypass transition in an external environment, despite being an ideal way to accelerate the natural transition process in a closed controlled environment such as a low turbulence wind tunnel (Ergin & White, 2006).

The effects of a three-dimensional rough feature on boundary layer flow differ significantly from those of a two-dimensional disturbance. Although a separation pocket usually appears after the isolated element, its downstream reach is much smaller than that of a 2-D disturbance. In addition, different flow characteristics occur at the isolated feature's position. Qualitatively, isolated rough components of varied symmetrical forms have been found to introduce similar vortical patterns, while differences in critical roughness Reynolds numbers, $Re_{k,crit}$, have been observed (Acalar & Smith, 1987). Gregory and Walker (1956) used a rough cylindrical element to investigate flow characteristics, whereas Mochizuki (1961) used a single sphere with changing diameters and smoke visualisation to investigate flow characteristics. The two research findings reveal similar flow characteristics. The flow characteristic that distinguishes an isolated element, is a primary vortex filament wraps around the sphere, forming two

symmetric tail vortices on either side. The downwash in the wake is caused by the symmetric vortices behind the element. Due to its form, the induced flow structure has been given the term horseshoe vortex. Figure 1-7 shows smoke streaks at various heights that provide details of the overall structure (Mochizuki, 1961).

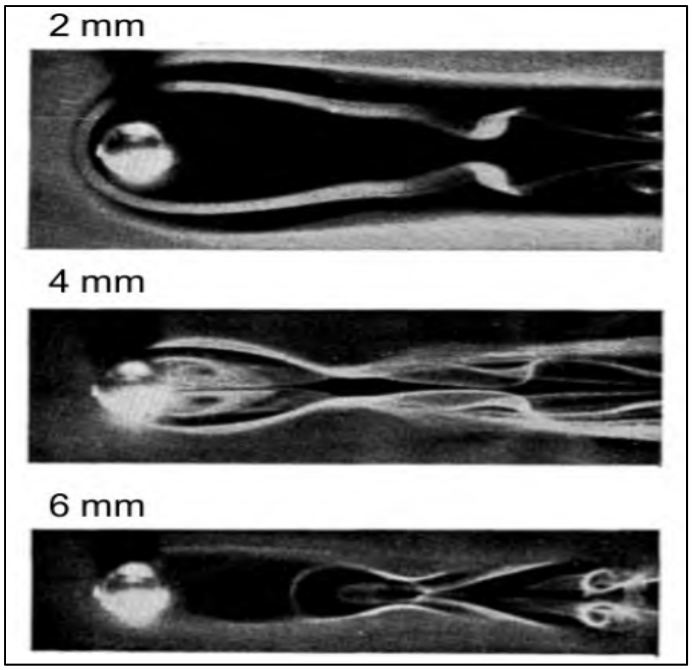

Figure 1-7 Horseshoe vortex at different roughness heights
Taken from Mochizuki (1961)

The impact of varying freestream velocity on the flow behind the rough element is seen in Figure 1-8. It can be seen how a single smoke trail appears behind the rough element at low freestream velocities. The trailing vortices continue to regularly deform as the velocity increases, generating hairpin vortex structures. The system of vortices is stable at low Re_k levels and has little effect on the flow around them. Until they are pushed up out of the shear layer and dissipated, the vortex structures stay isolated. The horseshoe vortex arrangement becomes unstable as Re_k grows, and the protuberance begins to shed hairpin vortices on a regular basis. Because the vortices' shedding frequency is greater than the essential disturbance band for Tollmien-Schlichting wave amplification, the transition process is only slightly

accelerated in this range of Re_k. A further increase in Re_k to the critical range causes a turbulent wedge to emerge behind the rough element. The wedge expands quickly, forming a transitory boundary layer that bypasses the traditional 2-D amplification process (Langel et al., 2017).

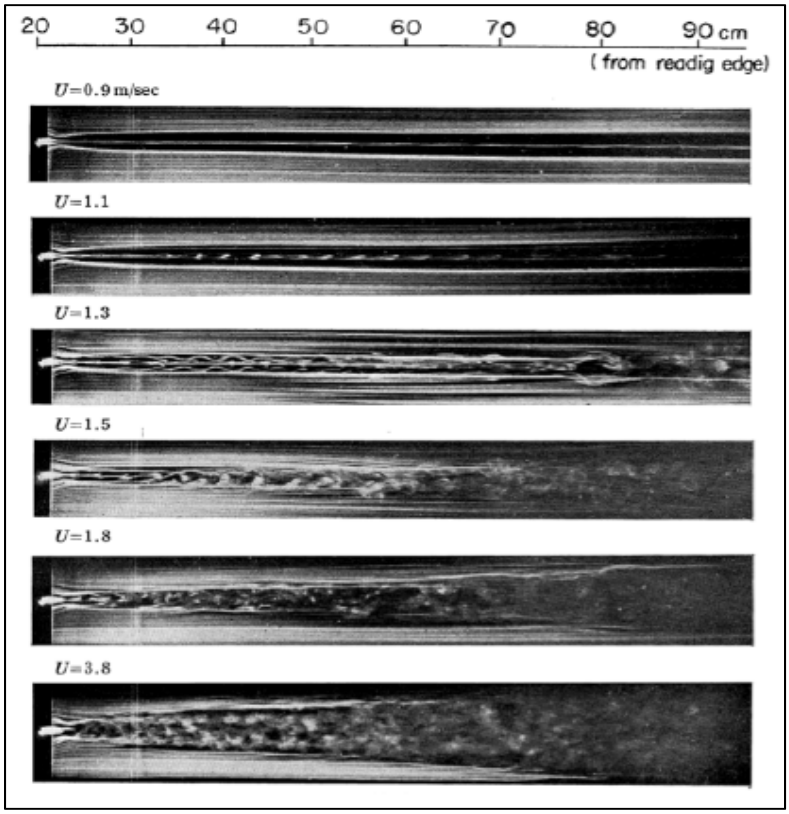

Figure 1-8 Flow behind a roughness element at different freestream velocities
Taken from Mochizuki (1961)

1.3.2 Distributed roughness

The flow behavior over distributed roughness is different from the one over an isolated roughness. When several clustered roughness elements are present, the well-behaved and well-understood vortex patterns found in the presence of single 3-D roughness vanish. In 1933, Nikuradse started the study of distributed roughness. The early studies were primarily focused

on studying the practical friction factor increases in pipe flows, rather than studying the impact of roughness on transition or providing a detailed analysis of the surrounding flow field (Nikuradse, 1933). In 1937, Schlichting developed the equivalent sand-grain roughness (k_s), an idealised roughness determined from the real roughness height using empirical correlations based on Nikuradse's data. The height, shape, and density of roughness all impact k_s, according to him (Schlichting, 1937). Dirling (1973) presented a correlation that translates topological characteristics into the k_s.

Feindt published one of the earliest studies on the impact of distributed roughness on the transition process in 1956. He established the effect of modifying the roughness Reynolds number on the transition onset position by utilising various roughness heights across the length of a flat plate. For various pressure gradients, he was able to link the Reynolds number based on the equivalent sand roughness height, Re_{k_s}, with the Reynolds number based on the transition onset location, Re_x. In addition, the study found that roughness had no effect on the position of transition for flow over a surface with a $Re_{k_s} < 120$ (Feindt, 1956).

With Re_k values of 10 and 150, (Levanthal & Reshotko, 1981) work gave greater insight into the effects of distributed roughness. The boundary layer profiles seen at the $Re_k = 10$ value were Blasius in shape, while the mean profile remained unaffected. The mean profile for the initial laminar portion of the boundary layer was seen to be Blasius in shape at the $Re_k = 150$ value, with the exception that it was displaced upwards. The initial disturbances' amplification rate was also found to be three times higher than that of smooth Tollmien-Schlichting waves. The frequencies amplified by distributed roughness were all lower than the normal Tollmien-Schlichting frequencies, showing that the mechanism influencing transition was different from that of an isolated roughness element at $Re_k = 300$ (Levanthal & Reshotko, 1981). Kendall's research confirmed the existence of an outwardly displaced Blasius profile in the Re_k intermediate range (Kendall, 1990). The roughness-influenced boundary layer's receptivity to external disturbances was investigated by Corke, Bar-Sever, and Morkovin. The low inertia fluid below the top of the roughness was thought to make the fluid more susceptible to freestream disturbances (Corke, Bar-Sever & Morkovin, 1986).

Moving on to more complicated geometries, most of the research focuses on quantifying the impact of roughness on practical performance measures including lift and drag. The effects of ice on airfoil applications have inspired a lot of research, but many tests, especially in the early years of roughness research, did not detail the effects of roughness on the transition process. Kerho and Bragg performed a case study that documented the development of a boundary layer over the surface of an airfoil with large-scale leading edge erosion. In this study hot-wire anemometry was used to measure the boundary layer on a two-dimensional NACA 0012 airfoil at three different Reynolds numbers using distributed roughness at different locations over the airfoil. Mean and fluctuating velocity, turbulence intensity, flow field intermittency, and associated integral parameters were measured. The transitional boundary layer caused by large distributed roughness differs significantly from the smooth model Tollmein-Schlichting induced transition process, according to the findings. There were no fully developed turbulent boundary layers around the roughness location. Rather, the large dispersed roughness was shown to cause a transitional boundary layer to develop at or near the roughness location. To reach a fully developed turbulent state, this transitional boundary layer required a significant chordwise extent. In comparison to the smooth model transitional region, streamwise turbulence intensity levels in the roughness induced transitional region were found to be comparatively low (Kerho & Bragg. 1997). The results of this study are used to validate the roughness correlation model in the current work.

1.4 Roughness models

Many early roughness models consisted of nothing more than a single variable describing the critical roughness Reynolds number, $Re_{k,crit}$, which would trip the flow. Because it has long been known that roughness causes highly complicated flow behaviour, researchers did not seek to go beyond these simple critical value type correlations at first. The creation of roughness models has been facilitated by the growth of both RANS type simulations and analytical knowledge of the transition process. The creation of models that view roughness as a change

in the spectrum of the OS equation has been prompted by improvements in our knowledge of transient growth as a path to transition. There is no method to directly model the effects of roughness other than discretizing each roughness element and performing a highly resolved DNS simulation. Understanding the specific physical mechanism connected with the disturbances roughness introduces into the flow has importance, but accounting for each particular perturbation is not practicable today from a modelling perspective. RANS techniques are the current state of the art for flow simulations; therefore, it makes sense to try to create roughness models that are RANS compatible (Langel et al., 2017).

Modifications to the governing equations in RANS simulations can be divided into two different sections. First, turbulent boundary layer modification to take the roughness effect into account. Second, modifications to the transition onset location cause by the roughness. This section is devoted to review the related literature regarding these modifications.

1.4.1 Turbulent boundary layer modification in RANS simulation

Roughness causes a change in the log layer of a turbulent boundary layer, according to several studies. The "law of the wall" equation for turbulent boundary layers is changed in the presence of roughness by a function of the roughness parameters (Langel et al., 2017). This shift may be mimicked in eddy-viscosity based turbulent simulations by modifying the turbulence model's boundary condition over a rough wall. Wilcox (1988) introduced a roughness adjustment for the $k-\omega$ model in 1988, and the results were satisfactory. Wilcox's model, on the other hand, does not work well with the $k-\omega$ SST model, according to Hellsten and Laine (1998). As a result, they presented a modification to the $k-\omega$ SST model that adjusts the surface value of ω to account for roughness. Similarly, Knopp et al. (2009) improved not only model compatibility with the $k-\omega$ SST, but also a weakness in Wilcox's model: the necessity of a significantly finer near-wall grid resolution for rough walls than smooth walls.

ONERA and Boeing independently developed two different extensions for the Spalart-Allmaras turbulence model (Aupoix & Spalart, 2003). Both models are based on the commonly used equivalent sand grain technique, k_s, which is employed in the turbulent model to approximate the shear friction increase. k_s yielded overestimated heat flux values, according to Aupoix (2015). To enhance estimations, the author presented a Prandtl number adjustment based on a large database obtained using the discrete element approach.

1.4.2 Modification to transition onset location

While changes to the turbulence model boundary conditions can modify mean profiles once the boundary layer has transitioned completely, the acceleration of the transition process requires additional considerations. Elsner and Warzecha (2014) and Stripf, Schulz, Bauer and Witting (2009) suggested a direct change of the transition onset criterion based on roughness height and displacement thickness. The introduction of the displacement thickness into the calculation requires a non-localizing integral computation. A more subtle disadvantage is that attempting to obtain an exact number, where a rough surface would transition, effectively negates flow history effects. Dassler, Koluvic, and Fiala (2010 & 2012) took a similar technique to model roughness by introducing a field variable regulated by an extra transport equation that defines a roughness influence region. After that, the scalar field is employed to change the transition onset criterion. By changing the parameters, Langel et al. (2014) extended the model to include airfoils. This model is then implemented into the RANS-based in-flight icing code by Min and Yee (2021) and improved the ice shape prediction on airfoils.

1.5 Research objective

In this literature review, studies concerning the transition process and the effect of roughness on it have been discussed and some of the CFD compatible models were presented. The SA-BCM transition model is chosen as the underlying model in this study since it is considered as

an algebraic model and therefore the computational cost is lower compared to the other available transition model. Additionally, this model was implemented and available in SU2 which is an open-source flow solver. The main objective of this research is to propose a correlation to enable the SA-BCM transition model to take the roughness effect into account. This objective solely concerns the transition onset location and the effect of roughness on the flow after the transition point is not an objective here. Two sub-objectives are accomplished in order to achieve the main objective. First, an existing transition correlation is modified to mimic the transition points of the experimental data over a rough flat plate. Second, the suggested model is validated against 2-D rough airfoil results.

CHAPTER 2

MODEL AND METHODOLOGY

This chapter presents the methodology used in this research to extend the use of a transition model over rough surfaces. This chapter holds six main sections starting with the Reynolds-Averaged Navier Stokes (RANS) equations. In the second step, the mathematical model used for the Spalart-Allmaras (SA) turbulence model is shown. Next, the modifications to the SA model in order to implement the transition onset correlation are presented. This is then followed by our proposed model to extend the transition model over the rough surfaces. Then, SU2 as our flow solver is introduced and finally, the numerical method used in this study is presented.

2.1 Reynolds-Averaged Navier Stokes (RANS) equations

In turbulence, being unsteady is a characteristic of the flow, in other words, eddies of various sizes are constantly generated and dispersed. Looking at the flow as a mixture of both a time-averaged flow and a fluctuating component is one way to eliminate the temporal characteristic (Langel et al., 2017). Reynolds proposed that the equations of motion be averaged by dividing the quantities into the mean and the fluctuation portions. The Reynolds-Averaged Navier-Stokes equations are the result of this process, which is known as the Reynolds decomposition (Reynolds, 1894)

$$v_i = \overline{v_i} + v_i'' \tag{2.1}$$

where the bar is denoting the mean velocity value which is $\overline{v_i} = \frac{1}{T}\int_0^T v_i dt$. The fluctuation is shown by a double prime. It must be noted that the time averaging of a fluctuating component is equal to zero by definition.

Applying the Reynolds decomposition process to the Navier-Stokes variables and time averaging the entire equations will result in the Reynolds-Averaged-Navier-Stokes (RANS) equations. According to Blazek (2015), it is advised to use the Reynolds averaging for density and pressure in compressible flows when the density is not constant, whereas the Favre averaging is used for the other variables, resulting in:

$$\frac{\partial \bar{\rho}}{\partial t} + \frac{\partial}{\partial x_i}(\bar{\rho}\tilde{v_\iota}) = 0 \tag{2.2}$$

$$\frac{\partial}{\partial t}(\bar{\rho}\tilde{v_\iota}) + \frac{\partial}{\partial x_j}(\bar{\rho}\tilde{v}_j\tilde{v}_i) = -\frac{\partial \bar{p}}{\partial x_i} + \frac{\partial}{\partial x_j}(\tilde{\tau}_{ij} - \bar{\rho}v_i''v_j'') \tag{2.3}$$

$$\frac{\partial}{\partial t}(\bar{\rho}\tilde{E}) + \frac{\partial}{\partial x_j}(\bar{\rho}\tilde{v}_j\tilde{H}) = \frac{\partial}{\partial x_j}(k\frac{\partial \tilde{T}}{\partial x_j} - \bar{\rho}v_j''h'' + \tau_{ij}v_i'' - \bar{\rho}v_j''K) + \frac{\partial}{\partial x_j}[\tilde{v}_i(\tilde{\tau}_{ij} - \bar{\rho}v_i''v_j'')] \tag{2.4}$$

In which $\bar{\rho}$ is the mean density, $\tilde{v}_i$ is the mean velocity, $\bar{p}$ is the mean pressure, K is the turbulent kinetic energy, k is the thermal conductivity coefficient and h is the enthalpy. In the above equations, the bar shows the Reynolds-averaged values, the tilde illustrates the Favre-averaged values, and the double prime denotes the fluctuating parts. Favre-averaged Reynolds stress tensor is defined as:

$$\tau_{ij}^F = -\bar{\rho}v_i''v_j'' = 2\mu_{tur}\tilde{S}_{ij} - \left(\frac{2\mu_{tur}}{3}\right)\frac{\partial \tilde{v}_k}{\partial x_k}\delta_{ij} - \frac{2}{3}\bar{\rho}\widetilde{K}\delta_{ij} \tag{2.5}$$

In which $\mu_{tur}$is the eddy viscosity, $\tilde{S}_{ij}$ is the Favre-averaged strain rate and $\widetilde{K}$ is the Favre-averaged turbulent kinetic energy.

2.2 Spalart-Allmaras (SA) turbulence model

An extra turbulent model is needed to solve the new unknowns which have been yielded from developing the RANS equations. These unknowns which are called Reynolds stresses arise from the averaging process in the derivation of the RANS equations.

In this study, the Spalart-Allmaras (SA) turbulence model (Spalart & Allmaras, 1994), a one-equation model, is used as the base model. This model has been developed by Spalart and Allmaras in 1994 to take the Reynolds stresses into account. The SA model uses one additional transport equation and is implemented in an open-source CFD code named Stanford University Unstructured (SU2) by Palacios et al., (2013). The governing equation of the SA model for the working variable ν_T is (Çakmakçıoğlu et al., 2018):

$$\frac{\partial \nu_T}{\partial t} + \frac{\partial}{\partial x_j}(\nu_T u_j) = C_{b1}\tilde{S}\nu_T - C_{w1} f_w \left(\frac{\nu_T}{d}\right)^2 + \frac{1}{\sigma}\left[\frac{\partial}{\partial x_j}\left((\nu_L + \nu_T)\frac{\partial \nu_T}{\partial x_j}\right) + C_{b2}\frac{\partial \nu_T}{\partial x_j}\frac{\partial \nu_T}{\partial x_j}\right] \tag{2.4}$$

in which the eddy viscosity is given by:

$$\nu_t = \nu_T f_{v1} \text{ where } f_{v1} = \frac{\phi^3}{\phi^3 + C_{v1}^3} \text{ and } \phi = \frac{\nu_T}{\nu_L} \tag{2.5}$$

ν_L is the kinematic molecular viscosity and d is the distance to the wall in the above equations. The function f_w is given as:

$$f_w = g\left[\frac{1 + C_{w3}^6}{g^6 + C_{w3}^6}\right]^{\frac{1}{6}}, \qquad g = r + C_{w2}(r^6 - r), \qquad r = \frac{\nu_T}{S\kappa^2 d^2} \tag{2.6}$$

The different constants appearing in equations 2.4 to 2.6 are (Çakmakçıoğlu et al., 2018):

$$\sigma = \frac{2}{3}, C_{b1} = 0.1355, C_{b2} = 0.622$$

$$C_{w1} = \frac{C_{b1}}{\kappa^2} + \frac{1 + C_{b2}}{\sigma} = 3.24, \kappa = 0.41$$

$$C_{v1} = 7.1, C_{w2} = 0.3, C_{w3} = 2.0$$

2.3 SA-BCM (Spalart-Allmaras Bas-Çakmakçıoğlu with modification) transition model

The idea behind the SA-BCM transition model is to damp the turbulence production until it reaches the transition onset. After that point, the damping function will be disabled, and the flow is allowed to be fully turbulent. This purpose is achieved by multiplying an intermittency function by the production term of the SA turbulent model:

$$\frac{\partial \nu_T}{\partial t} + \frac{\partial}{\partial x_j}(\nu_T u_j) = \gamma_{BC} C_{b1} \tilde{S} \nu_T - C_{w1} f_w \left(\frac{\nu_T}{d}\right)^2 + \frac{1}{\sigma}\left[\frac{\partial}{\partial x_j}\left((\nu_L + \nu_T)\frac{\partial \nu_T}{\partial x_j}\right) + C_{b2}\frac{\partial \nu_T}{\partial x_j}\frac{\partial \nu_T}{\partial x_j}\right] \quad (2.7)$$

γ_{BC} is defined as below

$$\gamma_{BC} = 1 - \exp(-\sqrt{Term_1} - \sqrt{Term_2}) \quad (2.8)$$

in which

$$Term_1 = \frac{\max(Re_\theta - Re_{\theta c}, 0.0)}{\chi_1 Re_{\theta c}} \quad (2.9)$$

where

$$Re_\theta = \frac{Re_\nu}{2.193}, Re_\nu = \frac{\rho d^2}{\mu}\Omega \quad (2.10)$$

In the above equations, χ_1 is the calibration constant, ρ is the local density, μ is the local molecular viscosity, Ω is the vorticity, d is the distance to the nearest wall, Re_v is the vorticity Reynolds number, Re_θ is the momentum thickness Reynolds number, and $Re_{\theta c}$ is the experimental transition onset critical momentum thickness Reynolds number which is defined as:

$$Re_{\theta c} = 803.73 \times (Tu_\infty + 0.6067)^{-1.027} \tag{2.11}$$

in which Tu_∞ is the freestream turbulence intensity.

The physical meaning of $Term_1$ is that it compares the locally computed Re_θ to the experimental correlation $Re_{\theta c}$ to check for the transition's onset point. $Term_1$ becomes greater than 0.0 when the so-called vorticity Reynolds number Re_v surpasses a threshold value, and the intermittency function γ_{BC} is triggered. However, because the Re_v is a function of the wall distance d, it takes a very low value inside the boundary layer (close to the wall). As a result, utilising only $Term_1$ to generate intermittency inside the boundary layer is impossible. To address this, $Term_2$ is introduced in equation 2.12, which aids in the penetration of $Term_1$'s intermittency into the boundary layer. Initially, $Term_2$ was defined as:

$$Term_2 = \frac{max(\nu_{BC} - \chi_2, 0.0)}{\chi_2} \tag{2.12}$$

where

$$\nu_{BC} = \frac{\nu_t}{Ud} \tag{2.13}$$

In the above equations, U is the local velocity magnitude and χ_2 is a calibration constant. The model has been calibrated against the (Schubauer & Klebanoff, 1955) flat plate test case and the calibration constants were given as $\chi_1 = 0.002$ and $\chi_2 = 5.0$.

There were two issues reported in this model. First, the use of velocity in ν_{BC} (eq.2.13) makes the model, not Galilean invariant. As a result, the outcome will be influenced by the frame of reference. This dependency should be avoided in turbulence modeling. Secondly, the calibration constant, χ_2 is reported by the author to be 5.0. However, in the source code $\chi_2 = 5.0/Re$ has been used. This addition of Re might be troublesome since it introduces a potentially non-unique reference length. Normally, turbulence models avoid such a dependency.

2.3.1 SA-BCM source code modification

In this section, the modification to the source code to overcome the above-mentioned problems is reported. These problems have been solved by redefining $Term_2$ and recalibrating the χ_2 by the authors of the original SA-BC model in 2020 (Mura & Çakmakçıoğlu, 2020). New $Term_2$ is defined as follows

$$Term_2 = \max(\frac{\mu_T}{\chi_2 \mu}, 0.0) \tag{2.14}$$

where μ_T is the eddy viscosity, and $\chi_2 = 0.02$. These modifications were not available in the SU2 version 6.2.0. Therefore, the changes have been applied to the source code in SU2. To validate the modifications, the results of the flat plate test cases are shown in chapter three.

2.4 Extension of SA-BCM model over rough surfaces

The development of the SA-BCM transition model to take the surface roughness into account is presented in this study. The idea is to manipulate the transition onset location and calibrate it with the experimental data. As it has been already mentioned in the introduction chapter, the goal of this study is to predict the start of the transition region over rough surfaces. Since the model is not coupled with the extension of the SA turbulent model over rough surfaces

(Tagawa, Morency & Beaugendre, 2021), the values of the skin friction coefficient are not valid in the turbulent region. However, the skin friction coefficient values in the laminar region and before the transition onset point are valid.

The equivalent sand grain roughness, k_s, is used in this study. k_s is first presented in (Schlichting, 1937) as an idealised roughness height that represents the height of a sand grain from (Nikuradse, 1933)'s tests. Translation of the normal height to the sand grain roughness is often done by Dirling's equations (Dirling, 1973).

$$\begin{cases} \frac{k_s}{k} = 0.0164\lambda^{3.78} & \lambda < 4.93 \\ \frac{k_s}{k} = 139\lambda^{-1.90} & \lambda > 4.93 \end{cases} \tag{2.15}$$

in which k_s is the equivalent sand grain roughness, k is the normal height and λ is equal to

$$\lambda = (\frac{r_0}{k})(\frac{A_p}{A_s})^{-4/3} \tag{2.16}$$

In the above equation r_0 is the roughness center to center spacing and $\frac{A_p}{A_s}$ is the ratio of roughness element projected area to windward surface area.

The SA-BCM model locates the transition point by using the Menter's experimental correlation (Menter et al., 2015), (eq. 2.11). In this correlation, the local turbulence intensity (TI), which has been calculated from turbulent kinetic energy, is used to predict the transition onset. However, this variable is not available in the SA model. Similar to Suluksna and Juntasaro (2008) the freestream turbulence intensity ($FSTI$) is used and assumed to be constant similar to Medida's simulations (2014).

In general, the surface roughness causes the transition onset location to move upstream. Due to this, by taking the Menter's correlation (eq. 2.11) and using a variable to decrease the critical momentum thickness Reynolds number to move the transition location upstream we have:

$$Re_{\theta c,new} = 803.73 \times (Tu_{\infty} + 0.6067)^{-1.027} - Re_{\theta c,rough} \tag{2.17}$$

Equation 2.11 is replaced by equation 2.17 and is implemented into the SU2 source code. The experimental results of Feindt (Feindt, 1956) over a flat plate without pressure gradient are used. In the Feindt experiment, the effect of modifying the roughness Reynolds number on the transition onset location has been studied by using various roughness heights across the length of a flat plate. By trial and error, the value of $Re_{\theta c,rough}$ to subtract from the $Re_{\theta c}$ to represent the same transition onset locations for various equivalent sand grain roughness is found.

In the next step, the input values of equivalent sand grain roughness Reynolds numbers are plotted against the values of $Re_{\theta c,rough}$. A roughness correlation to relate the two later-mentioned values is found using Matlab. Calibration of the constants and the roughness correlation results are discussed in the third chapter.

2.5 Flow solver

In this study, the Stanford University Unstructured (SU2) open-source flow solver is used. The SU2 software package was created to solve partial differential equation (PDE), analyses and PDE constrained optimization problems. Although the framework can be extended to solve multiphysics analysis and design problems with arbitrary sets of governing equations, the core of the suite is a Reynolds-averaged Navier–Stokes (RANS) solver that can simulate compressible, turbulent flows that are common in aerospace and mechanical engineering problems. SU2 is written in standard C++ as specified by the International Organization of Standardization, and it only uses widely available, well-supported open-source softwares, such

as Message Passing Interface (MPI) implementations, mesh partitioning packages, and popular scripting languages, for simplicity of use. As a result, SU2 can run on any machine that has a C++ compiler (Economon, Palacios, Copeland, Lukacyzk & Alonso, 2016).

The inputs of SU2 consist of a configuration and mesh files. The configuration file (name.cfg) is a simple text file that enables the available options in SU2. The mesh file used by SU2 is carrying the extension of .su2 which contains information about both the node locations and their connectivity (Palacios et al., 2013). There are several outputs produced by SU2 including the solution and restart files. Solutions can be visualized using Paraview and the restart file contains information to restart the simulation in SU2.

2.6 Numerical method

In our study, the flow around an airfoil is simulated with the compressible Navier-Stokes equations. Considering the domain of $\Omega \subset \mathbb{R}^3$ physical modeling of the problem will result in PDE system as

$$\partial_t U + \nabla . \overrightarrow{F^C} - \nabla . \overrightarrow{F^v} = Q \; in \; \Omega, \mathrm{t} > 0 \tag{2.18}$$

where U is the vector of state variables, $U = (\rho, \rho v_1, \rho v_2, \rho v_3, \rho E)^T$, $\overrightarrow{F^C}(U)$ shows the convective fluxes, $\overrightarrow{F^v}(U)$ represents the viscous fluxes, $Q(U)$ is the source term, ρ is the density E is the total energy per unit mass and $\vec{v} = (v_1, v_2, v_3) \in \mathbb{R}^3$ is the flow velocity in a Cartesian coordinate system. The convective and viscous fluxes can be written, respectively

$$\overrightarrow{F_i^c} = \begin{pmatrix} \rho v_i \\ \rho v_i v_1 + P\delta_{i1} \\ \rho v_i v_2 + P\delta_{i2} \\ \rho v_i v_3 + P\delta_{i3} \\ \rho v_i H \end{pmatrix} \tag{2.19}$$

$$\overrightarrow{F_i^v} = \begin{pmatrix} 0 \\ \tau_{i1} \\ \tau_{i2} \\ \tau_{i3} \\ v_j\tau_{ij} + \mu_{tot}^* C_p \partial_i T \end{pmatrix}, i = 1, 2, 3. \tag{2.20}$$

where P is the static pressure, H is the enthalpy, δ_{ij} is Kronecker delta function and $\tau_{ij} = \mu_{tot}\left(\partial_j v_i + \partial_i v_j - \frac{2}{3}\delta_{ij}\nabla.\vec{v}\right)$. Recall that the Latin indices $i\,j$ represent 3-D Cartesian coordinates in which repeating indices indicate summation. In the above equations, C_p is the specific heat at constant pressure, $T = P/R\rho$ is the temperature and R is the gas constant in a way that for an ideal gas, $C_p = \gamma R/(\gamma - 1)$ with γ being a constant. To close the equations, the dynamic viscosity, μ_{dyn}, is assumed to satisfy the Sutherland's law (White & Majdalani, 2006) and the turbulent viscosity, μ_{tur}, is calculated in the SA turbulence model and

$$\mu_{tot} = \mu_{dyn} + \mu_{tur}, \mu_{tot}^* = \frac{\mu_{dyn}}{Pr_d} + \frac{\mu_{tur}}{Pr_t} \tag{2.21}$$

in which Pr_d and Pr_t are the dynamic and turbulent Prandtl numbers, respectively. Additionally, the SA turbulence model can be rewritten in the framework of the general convection diffusion equation as

$$\overrightarrow{F^c} = \vec{v}\hat{v}, \overrightarrow{F^v} = -\frac{\nu + \hat{v}}{\sigma}\nabla\hat{v}, Q = c_{b1}\hat{S}\hat{v} - c_{w1}f_w\left(\frac{\hat{v}}{d}\right)^2 + \frac{c_{b2}}{\sigma}|\nabla\hat{v}|^2 \tag{2.22}$$

The Finite Volume method is used to discretize the Partial Differential Equations (PDEs) in SU2. The centroids, faces, and edge-midpoints of all cells sharing a node are connected to generate median-dual control volumes. The semi-discretized integral form of a typical PDE is given by,

$$\int_{\Omega_t}\frac{\partial U}{\partial t}d\Omega + \sum_{j\in\mathcal{N}(i)}\left(\widetilde{F_{c_{ij}}} + \widetilde{F_{v_{ij}}}\right)\Delta S_{ij} - Q|\Omega_i| = \int_{\Omega_t}\frac{\partial U}{\partial t}d\Omega + R_i(U) = 0 \tag{2.23}$$

where U is a vector of state variables and $R_i(U)$ is the residual. $\widetilde{F_{c_{ij}}}$ and $\widetilde{F_{v_{ij}}}$ are the projected numerical approximations of the convective and viscous fluxes, respectively and Q is a source term. ΔS_{ij} is the area of the face associated with the edge ij, Ω is the volume of the control volume and $\mathcal{N}(i)$ are the neighboring nodes to node i(Palacios et al., 2013).

The convective and viscous fluxes are evaluated at the midpoint of an edge and can be discretized using central or upwind methods in SU2. Simple low dissipation AUSM scheme with the alternative pressure flux formulation (SLAU2) (Kitamura & Shima, 2013) flux-difference-splitting approach calculates convective fluxes using flow quantities rebuilt independently on both sides of the control volume's face from values at the surrounding nodes:

$$\widetilde{F_{c_{ij}}} = \tilde{F}_{1/2} = \left(\frac{\dot{m} + |\dot{m}|}{2}\right)\Psi^{+} + \left(\frac{\dot{m} - |\dot{m}|}{2}\right)\Psi^{-} + \tilde{P}N \tag{2.24}$$

where $\Psi = (1, v_1, v_2, v_3, H)^T$ and $N = (0,\ n_x, n_y, n_z, 0)^T$. Pressure flux is defined as

$$\tilde{P} = \frac{P_L + P_R}{2} + \frac{f_P^+ - f_P^-}{2}(P_L - P_R) + \sqrt{\frac{u_{1L}^2 + u_{2L}^2 + u_{3L}^2 + u_{1R}^2 + u_{2R}^2 + u_{3R}^2}{2}}(f_P^+ + f_P^- - 1)\bar{\rho}C_{1/2} \tag{2.25}$$

where $f_P^{\pm} = \begin{cases} \frac{1}{2}\left(1 \pm sign(M)\right), & |M| \geq 1 \\ \frac{1}{4}(M \pm 1)^2(2 \mp M), & otherwise \end{cases}$, $M = \frac{V_n}{C_{1/2}} = \frac{v_1 n_x + v_2 n_y + v_3 n_z}{C_{1/2}}$ and $C_{1/2} = \frac{C_L + C_R}{2}$.

In equation 2.24, the mass flux is defined as

$$\dot{m} = \frac{1}{2}\left\{\rho_L(V_{nL} + |\overline{V_n}|^{+}) + \rho_R(V_{nR} - |\overline{V_n}|^{-}) - \frac{\chi}{C_{1/2}}\Delta p\right\}$$

where $|\overline{V_n}|^+ = (1-g)|\overline{V_n}| + g|V_{nL}|$, $|\overline{V_n}|^- = (1-g)|\overline{V_n}| + g|V_{nR}|$, $|\overline{V_n}| = \frac{\rho_L|V_{nL}|+\rho_R|V_{nR}|}{\rho_L+\rho_R}$, $g = -\max[\min(M_L, 0), -1] . \min[max(M_R, 0), 1]$ and $\chi = (1-\widehat{M})^2$ where $\widehat{M} = \min(1.0, \frac{1}{C_{1/2}}\sqrt{\frac{u_{1L}^2+u_{2L}^2+u_{3L}^2+u_{1R}^2+u_{2R}^2+u_{3R}^2}{2}})$.

In SU2, the values of the flow variables, including the velocity components, dynamic viscosity, and heat conduction coefficient k, are averaged at the cell faces. The gradients of the flow variables are computed at all grid nodes using the least-squares methods, and then averaged to get the gradients at the cell faces (Palacios et al., 2013).

2.7 Summary

In this chapter, the compressible RANS equations have been presented as the governing equations for the turbulent transition problem. To solve the RANS equations, the SA model has been introduced as the turbulence model to solve the Reynolds stresses. The SA-BCM transition model is an algebraic model based on the SA turbulent model as the underlying model. The methodology to extend the SA-BCM transition model to take into account the rough surfaces has been exposed. Finally, the SU2 flow solver provides the numerical methods used in this study.

CHAPTER 3

RESULTS AND DISCUSSION

Chapter 3 shows the model calibration and presents the results. This chapter holds three sections. First, the changes to the source code are validated against the flat plate in order to make sure that the underlying model is behaving as expected. The results of (Mura & Çakmakçıoğlu, 2020) are used as a reference. In the next step, the outcomes of implementing and calibrating the roughness correlation into SU2 code is shown. The zero pressure gradient flat plate with distributed roughness is used to predict the transition points. The results of (Feindt, 1956) are used as a guide. Finally, the model is validated and verified to predict the transition onset location over the NACA0012 airfoil with distributed roughness. The experimental results of (Kerho & Bragg, 1997) and the CFD results of (Langel et al., 2017) are used as a reference.

Each section starts with a presentation of the computational domain and a mesh description. Next, a mesh study is performed to ensure that the simulation results are independent of the grid size. Then the convergence of the simulation is illustrated and finally, the transition points are located and compared to the reference data.

3.1 Validation of the source code changes

This section is devoted to study the underlying (SA-BCM) model to ensure the model is behaving properly. The problem of Galilean invariant has been addressed in chapter 2 (section 2.3). Solution to this problem has been introduced in the section 2.3.1 and in this section, the results obtained with the modified source code are presented and compared to the literature.

3.1.1 Computational domain

Figure 3-1 illustrates the computational domain and the boundary conditions used to validate the source code changes over the 2-D flat plate. Similar to (Mura & Çakmakçıoğlu, 2020), the density is set to $\rho = 1.2\ {}^{kg}/_{m^3}$ and the viscosity is $\mu = 1.8 \times 10^{-5}\ {}^{kg}/_{m.s}$. The values of the free stream turbulence intensity (FSTI) and inlet velocity are shown in table 3.1. The mesh file used for this validation includes 273×193 (225 points on the wall) and was obtained from NASA's turbulence website (Rumsey, 2019). The flat plate is along the lower boundary of the grid (Y=0).

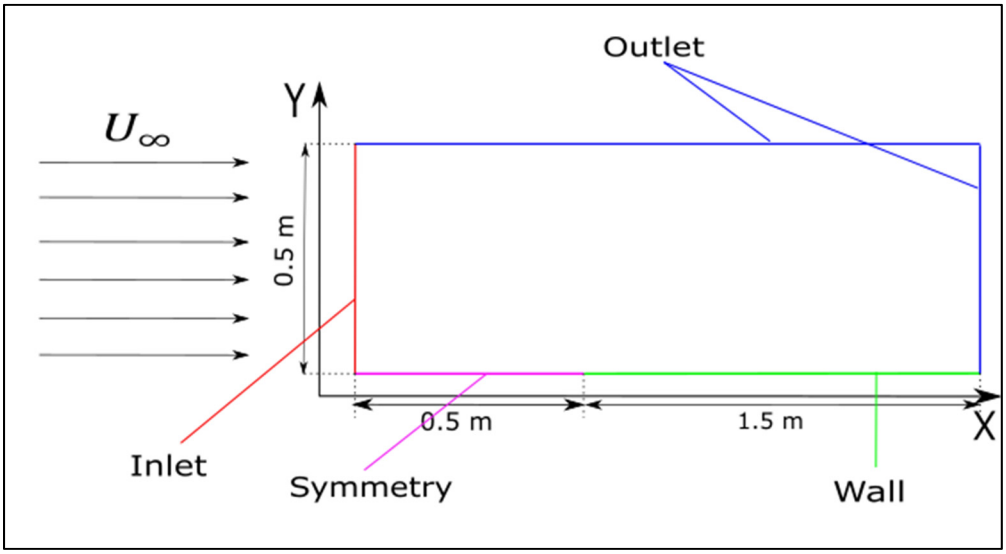

Figure 3-1 Computational domain around the flat plate

Table 3.1 Flat plate test cases

Test case	$U_\infty(^m/_S)$	Re_∞	$FSTI(\%)$
T3A	5.4	3.7×10^5	3.0
T3B	9.4	6.3×10^5	6.0

The simulations were solved iteratively using the incompressible flow, the CFL=1000, and using the FGMRES linear solver with 10 linear iterations and a linear error of 10^{-4}. For solving spatial gradients, the weighted least squares method is employed. FDS without a slope limiter is the convective numerical method for the flow (Roe, 1986). The scalar upwind procedure is adopted for the turbulence model, while Venkatakrishnan (Blazek, 2015) is employed as the slope limiter.

3.1.2 Results of source code modification

In this section, the results for the two test cases including T3A and T3B flat plates are presented and compared to the results of (Mura & Çakmakçıoğlu, 2020) as well as the experimental result. Figures 3-2 and 3-3 show the skin friction coefficient of the T3A and T3B test cases, respectively. In these figures, the skin friction coefficient is the Y-axis and the $Re_x = \frac{XU_\infty \rho}{\mu}$ is the X-axis.

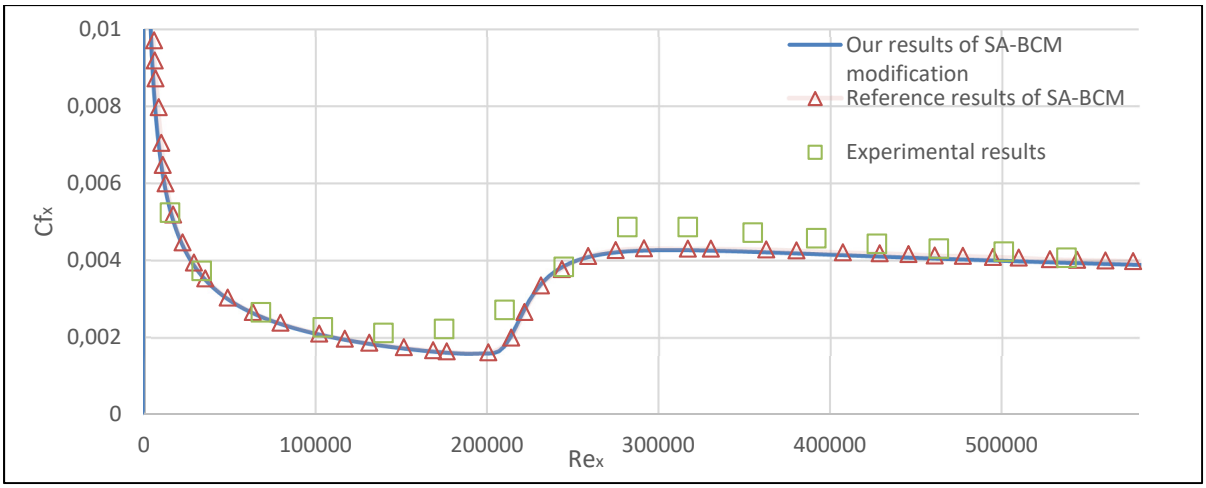

Figure 3-2 Comparison of the T3A test case with reference data

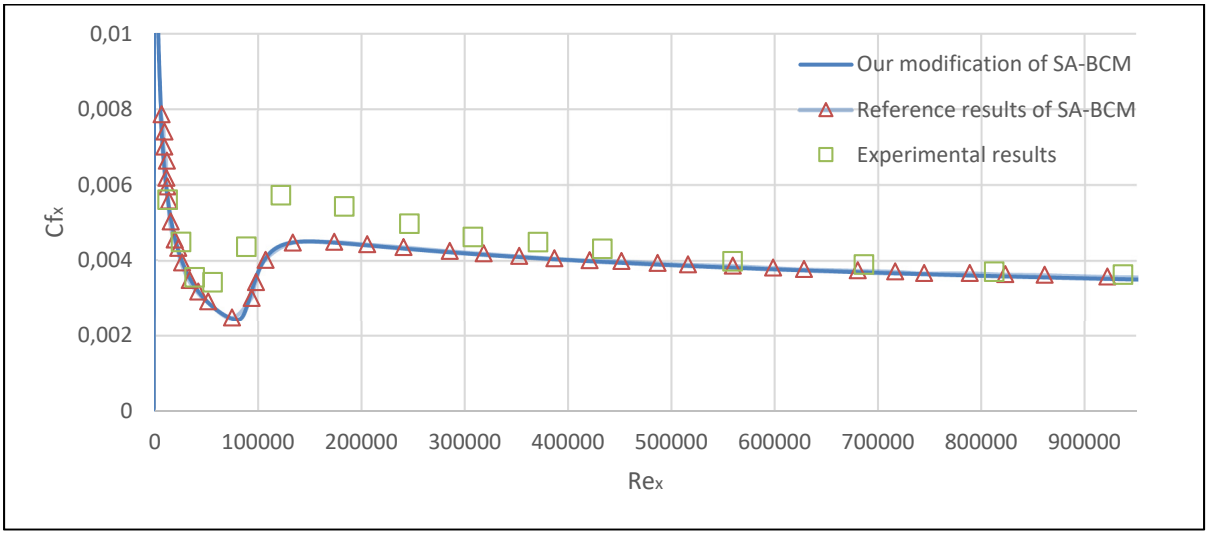

Figure 3-3 Comparison of the T3B test case with reference data

It is clear from both figure that the Modifications are in excellent agreement with the references. In other words, our modifications to the SA-BCM model are reproducing the same results as the references and the model is behaving as expected.

3.2 Roughness correlation and model calibration

As mentioned in section 2.4, Feindt's (Feindt, 1956) experimental results on a flat plate with no pressure gradient are employed. With using varying roughness heights throughout the length of a flat plate, Feindt experiment investigated the effect of altering the roughness Reynolds number on the transition onset position. By recalling the equation 2.17, the values of $Re_{\theta c,rough}$ to subtract from $Re_{\theta c}$ to have the same transition location as the experiment for each sand grain roughness are discovered via trial and error. In order to build the roughness correlation, $Re_{\theta c,rough}$ (equation 2.17), based on the input values of equivalent sand grain roughness, the values of $Re_{\theta c,rough}$ which represent the same transition onset location as experimental data are plotted against k_s in figure 3-4. In this simulation, for an inlet velocity of $U_\infty = 20\ {}^{m}/_{S}$, different input values of the equivalent sand grain roughness are applied. Since the exact value for the free stream turbulence intensity ($FSTI$) was not available in the experimental data, the same procedure used by (Langel et al., 2017) and (Dassler et al., 2010) is used. The $FSTI$ is set over the smooth flat plate in a way that the transition occurs at the same location as the experiments. $FSTI = 0.91\%$ and 1.1% is used by (Langel et al., 2017) and (Dassler et al., 2010), respectively. Our tests show that FSTI=1.07% is giving promising results. The same computational domain, mesh size, boundary conditions, and configuration setting of section 3.1 are used.

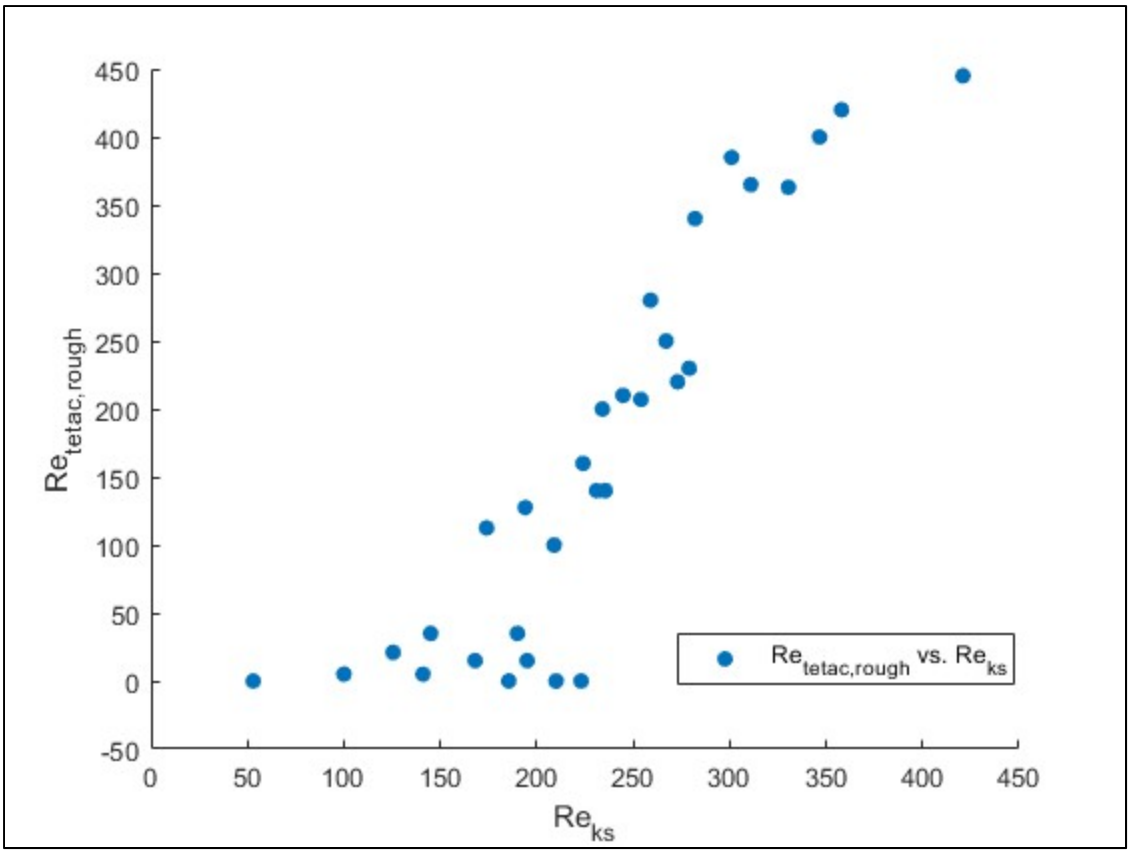

Figure 3-4 $Re_{\theta_{c,rough}}\ vs.\ Re_{ks}$

Figure 3-4 illustrates that small values of the sand grain roughness have no effect on the transition location. However, after $Re_{ks} = 130$, increasing the sand grain roughness, sharply increases the $Re_{\theta c,rough}$. In other words, a small increase in the sand grain roughness has a huge effect on the transition onset location. Additionally, it can be seen that after $Re_{ks} = 280$, the slope of the changes in $Re_{\theta c,rough}$ decrease. Figure 3-4 shows that two regions should be used for the roughness correlation similar to (Langel et al., 2017). For the first region between $Re_{ks} = 0.0$ to $Re_{ks} = 280$ an exponential function seems to fit well with the data and for the region after $Re_{ks} = 280$ a linear function would give promising results. In other words, $Re_{\theta c,rough}$ can be written as

$$Re_{\theta c,rough} = \begin{cases} A \times \exp\left(B \times Re_{k_s}\right) & Re_{k_s} < 280 \\ \left(C \times Re_{k_s}\right) + D & Re_{k_s} \geq 280 \end{cases} \quad (3.1)$$

in which A, B, C and D are the calibration constants. This correlation has been implemented in SU2 in a way that if no roughness is mentioned in the configuration file, the Menter's correlation will be used to determine the transition onset. However, if the roughness is mentioned in the configuration file, the combination of the Menter and roughness correlation will be used as below to locate the transition onset.

$$Re_{\theta c,new} = \begin{cases} Re_{\theta c} - A \times \exp\left(B \times Re_{k_s}\right) & Re_{k_s} < 280 \\ Re_{\theta c} - \left(C \times Re_{k_s}\right) + D & Re_{k_s} \geq 280 \end{cases} \quad (3.2)$$

Matlab is used to find out the calibration constants. Data in the region between $Re_{k_s} = 0.0$ to $Re_{k_s} = 280$ are fitted with an exponential function and data in the region after $Re_{k_s} = 280$ are fitted with one degree polynomial which yield, $A = 2.11$, $B = 0.01885$, $C = 0.2$ and $D = 373$.

Figure 3-5 shows the two functions alongside the $Re_{\theta c,rough}$ data. It can be seen that the exponential and linear functions captured the $Re_{\theta c,rough}$ data. In other words, the constants are calibrated against the flat plate results. It should be noted that the boundary for the functions in $Re_{\theta c,new}$ is set at $Re_{k_s} = 280$ in order to allow the roughness correlation to capture the roughness on the flat plate and the airfoil. In other words, $Re_{\theta c,new}$ has been calibrated against the flat plate with different calibration constants and boundaries and the calibration results have been evaluated against the NACA 0012 airfoil. These trials and errors led to the boundary of $Re_{k_s} = 280$ the calibration constants that are shown above.

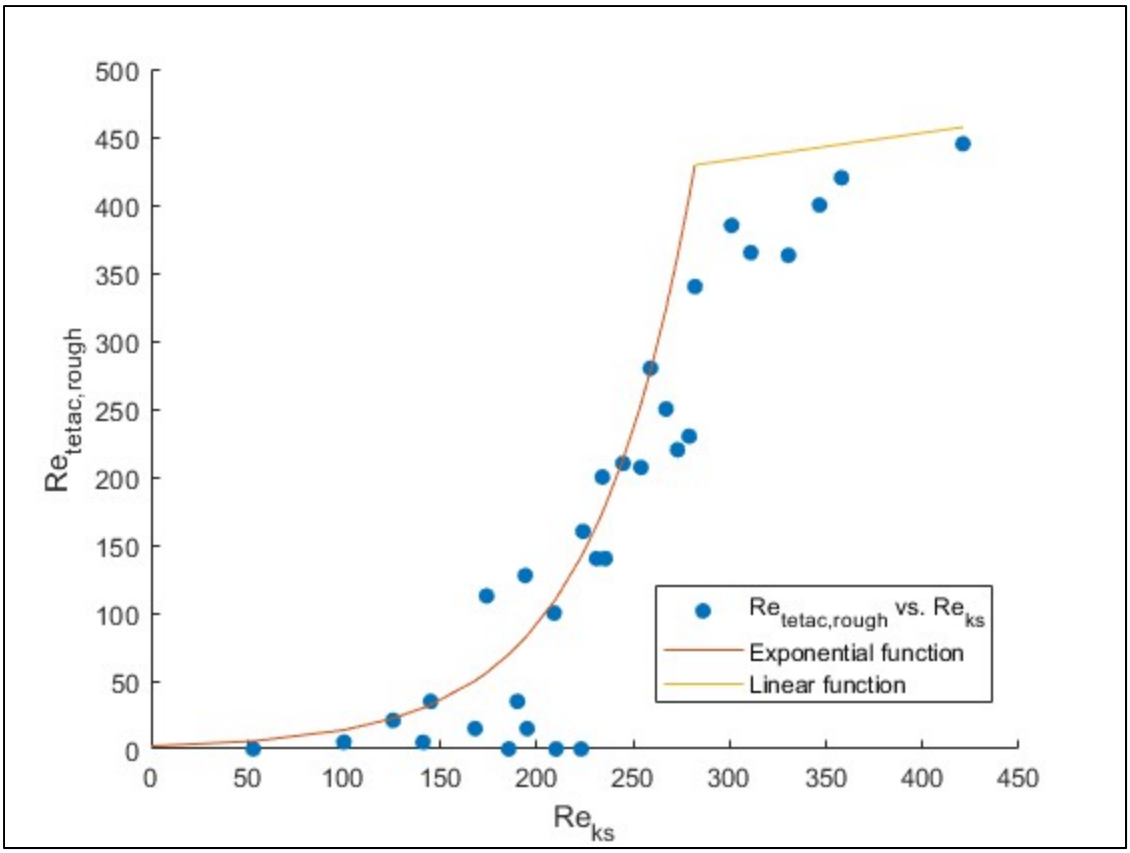

Figure 3-5 $Re_{\theta_{c,rough}}\ vs.\ Re_{ks}$ along with exponential and linear functions

3.2.1 Mesh study

The influence of the mesh size on the transition point and the skin friction coefficient is investigated using a mesh study. This study is done using five different grid sizes including 69×49 (57 points on the wall), 137×97 (113 points on the wall), 273×193 (225 points on the wall), 545×385 (449 points on the wall), and the reference mesh which has been used by (Mura & Çakmakçıoğlu, 2020) containing 41412 quadrilaterals. The finest mesh has minimum spacing at the wall equals to $y = 5 \times 10^{-7} m$ which gives $y^+ = 0.1$. Grid files are obtained from NASA's turbulent website (Rumsey, 2019). This study is performed over a smooth wall to compare the transition locations of different grid sizes using the same computational domain, mesh size, boundary conditions, and configuration setting as in section 3.1.

Before presenting the result, the convergence curves are shown to make sure that the results are converged. It has to be mentioned that only the convergence curves of the finest mesh are shown here. Figure 3-6 illustrates the log of the flow residuals including density, momentum, and turbulence, which are plotted against the number of iterations. The residual flows are shown in the Y-axis and the number of iterations is illustrated in the X-axis. It is clear that, the convergence criteria has been satisfied successfully after 10000 iterations.

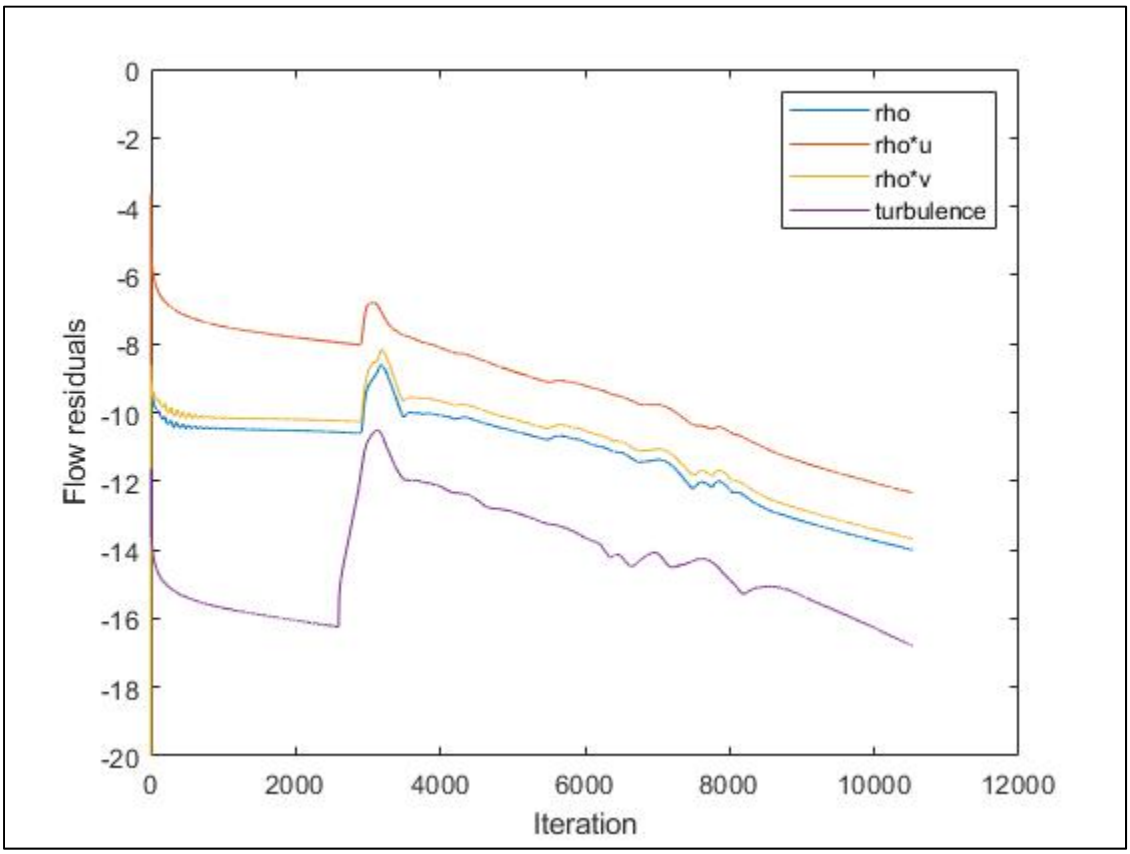

Figure 3-6 Flow residuals for flat plate

In this document, the transition location is referred to as the point where the skin friction coefficient value starts to grow. This is done by a manual inspection of the results. For instance, figure 3-7 demonstrates the transition point alongside one point before and after it for the finest

grid size. The skin friction coefficient is shown on the Y-axis and the Re_x coordinates are shown on the X-axis.

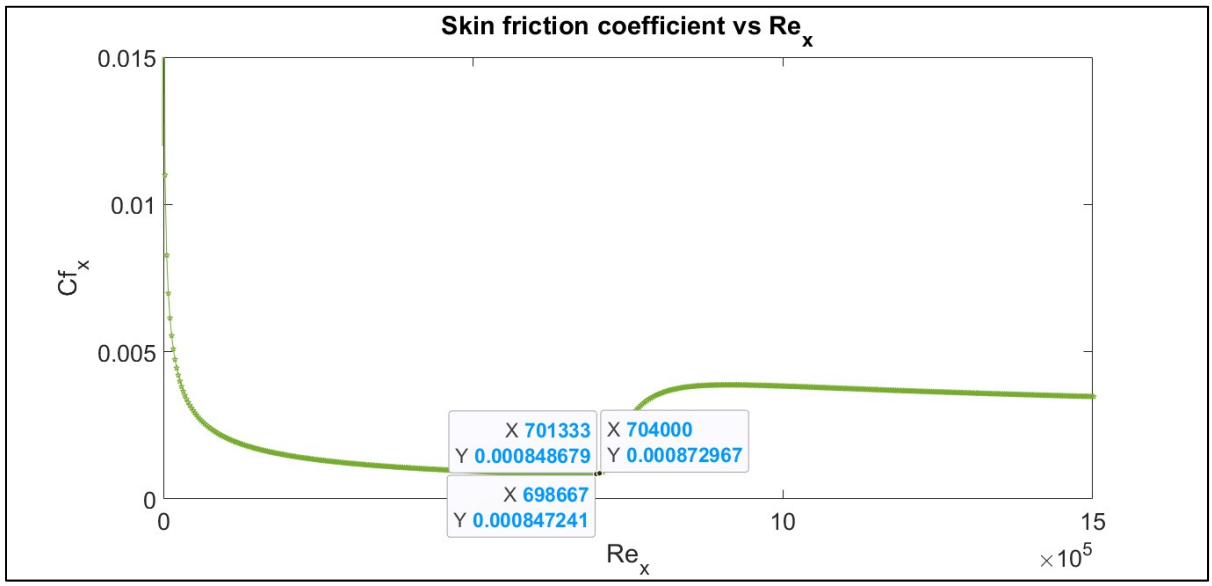

Figure 3-7 Transition onset location along with one point after and one point before it

Figure 3-8 shows the skin friction coefficient over the wall for different grid sizes varying from 69×49 to 545×385. In this figure, the skin friction coefficient is plotted on the Y-axis and the Re_x is plotted on the X-axis. The transition location moves downstream with grid refinement.

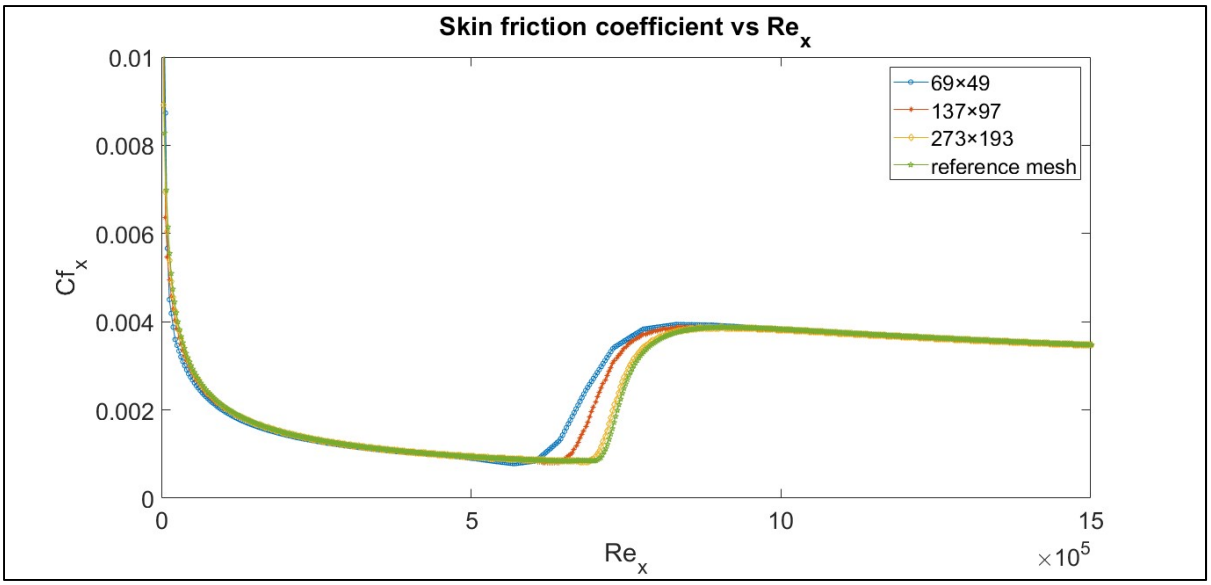

Figure 3-8 Skin friction coefficient vs Re_x for different grid sizes

By taking a closer look around the transition region in Figure 3-9, the transition point of the reference mesh is close to the one with the finest mesh. Table 3.2 compare the transition points for different grid sizes with the reference mesh. It can be seen that the grid file of 273×193 has a 2.23% error.

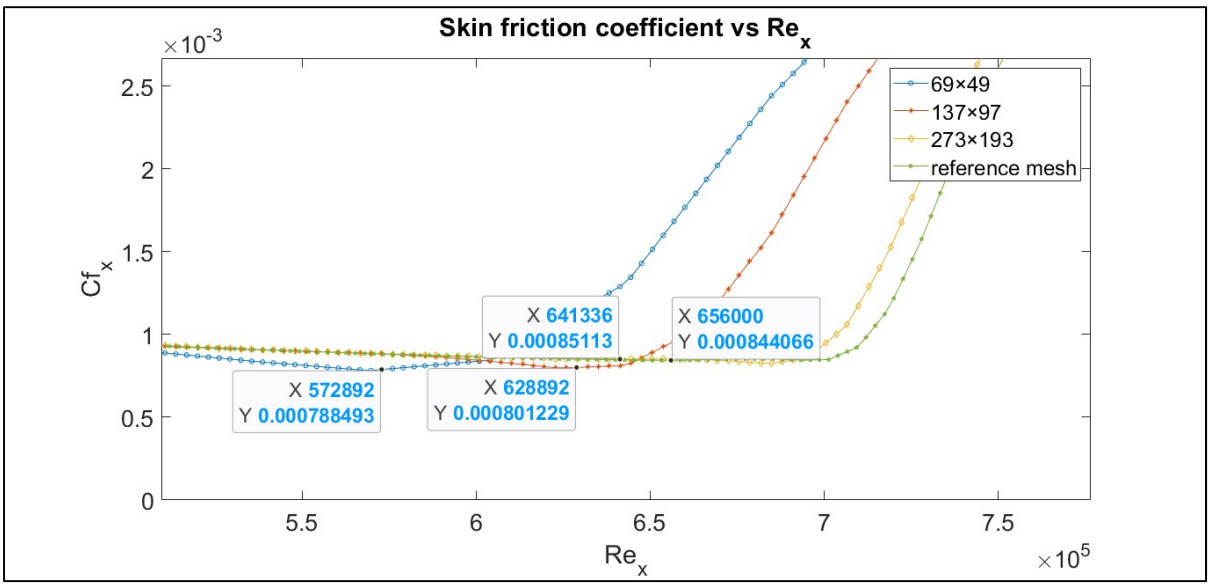

Figure 3-9 Transition point using different grid sizes

Table 3.2 Comparison of the transition point with the reference mesh

Mesh size	Error (%)
69×49	12.67
137×97	4.13
273×193	2.23

3.2.2 Rough flat plate

After the roughness correlation calibration, the effect of the roughness height on the transition point over the flat plate is presented and compared to the experimental and CFD results. The experimental results of (Feindt, 1956) and the CFD results of (Langel et al., 2017) are used as references. Since the results of (Feindt, 1956) were not accessible directly, they are used in a as per (Langel et al., 2017) and (Dassler et al., 2010). In the Feindt's experiment, different ranges of equivalent sand grain roughness height Reynolds numbers ($Re_{k_s} = \frac{u_\infty \times k_s}{\nu}$), are used over the flat plate without pressure gradient to locate the transition locations.

In our simulation, ten equivalent sand grain roughness height Reynolds numbers varying from $Re_{k_s} = 0.0 \ldots 420$ were used. Figure 3-10 represents the effect of Re_{k_s} on the transition onset location. With increasing Re_{k_s}, the transition from laminar to turbulent flow tends to start at a lower Re_x, thus, increasing the equivalent sand grain roughness pushes the transition location upstream. As it is mentioned in the literature, minor roughness heights have a very small influence on the start of the transition (Langel et al., 2017). This trend is obvious in figure 3-10, since there is a small change in the onset of the transition location using the smooth flat plate and using $Re_{k_s} = 50$.

It has to be noted that this study is focused on the transition onset location and that the model is not coupled with the extension of the SA model to study the effect of the roughness into the

boundary layer. Therefore, the current roughness correlation underestimates the values of the skin friction coefficient in the turbulent regime. However, the skin friction coefficients for the laminar regime are valid.

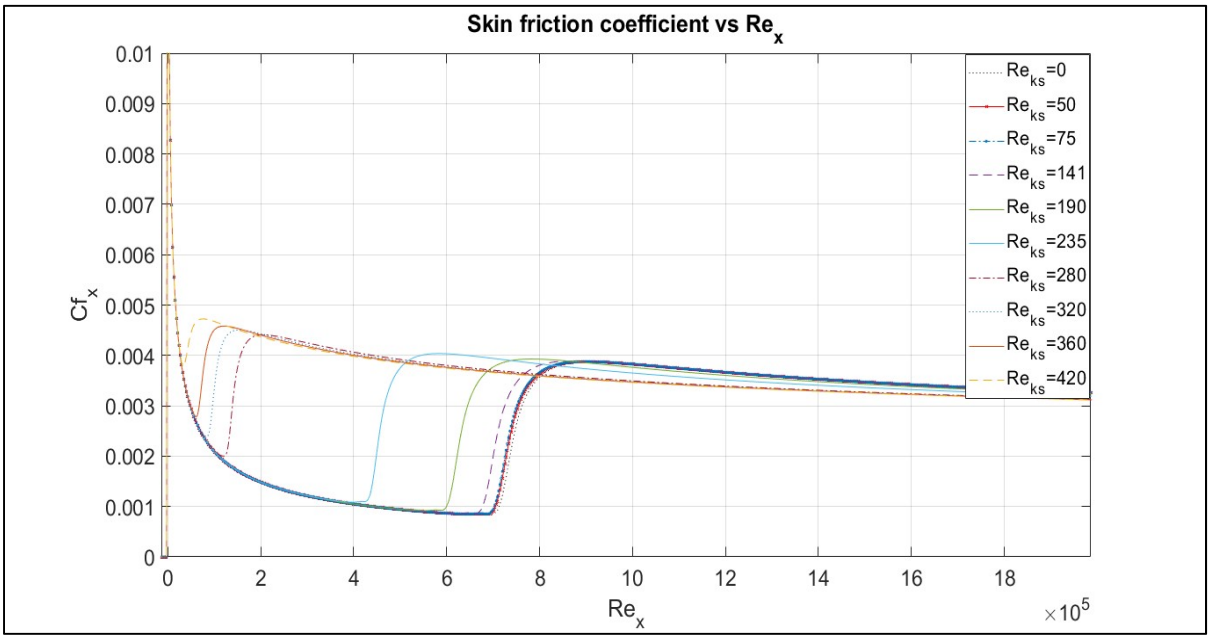

Figure 3-10 Effect of equivalent sand grain roughness Reynolds number on transition location

For the purpose of validating the start of the transition location, the outcomes are plotted alongside the experimental results of (Feindt, 1956) and CFD results of (Langel et al., 2017) in figure 3-11. In this figure, the transition locations (Re_x) are shown on the Y-axis and the equivalent sand grain roughness values (Re_{ks}) are presented on the X-axis.

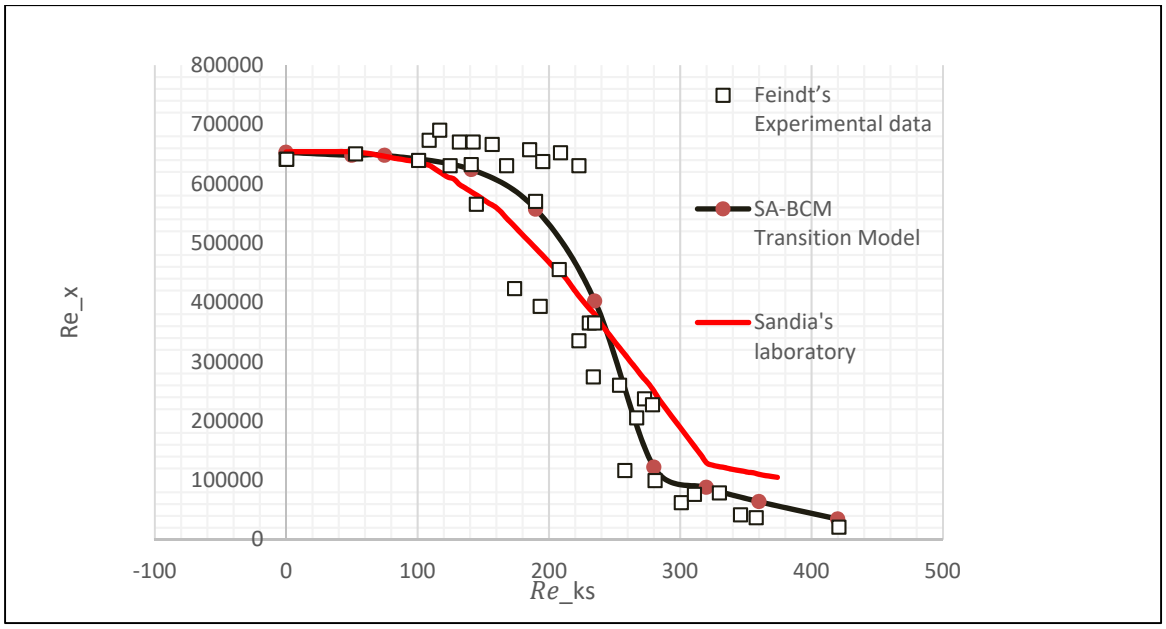

Figure 3-11 Comparison of transition onset location with experimental and CFD data

Although the experimental data is scattered, the roughness correlation was able to capture the onset of the transition. Another trend seen in this figure is that the transition onset location is insensitive to Re_{k_s} when $Re_{k_s} < 120$ (Dassler et al., 2010). On the other hand, after this point, the transition onset shifted sharply upstream by increasing the equivalent sand grain roughness Reynolds number. The smooth switch from cubic to linear functions in the roughness correlation is visible around $Re_{k_s} = 280$.

3.3 NACA 0012 airfoil

The NACA 0012 airfoil is used to validate the roughness correlation at two Reynolds numbers. The experimental results of (Kerho & Bragg, 1997) and the CFD results of (Langel et al., 2017) are used as references. In (Kerho & Bragg, 1997), the experiments were done on a NACA 0012 with a chord length of 0.5334 m. Figure 3-12 shows the roughness tape used in the experiment. Hemispherical shapes were used to simulate the roughness. The roughness strips were nominally 0.35 mm in height and 1.3 mm in center to center space.

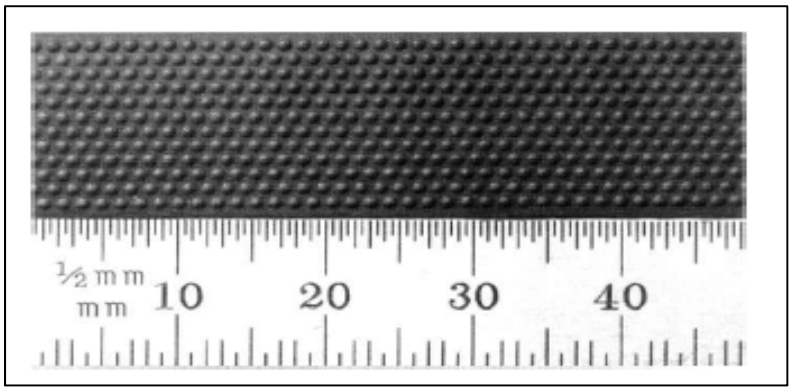

Figure 3-12 Top view of distributed roughness
used for experiment
Taken from Kerho & Bragg (1997)

To obtain the equivalent sand grain roughness, the Dirling's equation (equation 2.15) is used by assuming $\frac{A_p}{A_s} = 0.5$ for hemispherical roughness resulting in $k_s = 6.94 \times 10^{-4}\ m$.

It needs to be mentioned that in the experimental tests, different roughness extents including $^1/_8\ in, ^1/_4\ in$ and $^1/_2\ in$ are placed at different chordwise locations from the stagnation point varying from 4 mm to 24 mm. Figure 3-13 shows the roughness length and location used for the experiment. However, since only the roughness upstream of the transition point affects the flow, a fully rough airfoil is used in this study for simplicity, similar to (Gitsuzo et al., 2021).

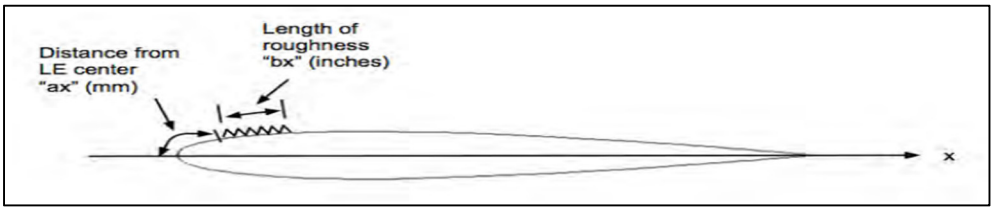

Figure 3-13 Roughness length and location on the NACA 0012
Taken from Langel et al. (2017)

3.3.1 Computational domain and numerical method

Figure 3-14 illustrates the computational domain around the airfoil. The airfoil has a chord, c, of 1 m and the farfield boundary layer is defined approximately 500c lengths away from the airfoil surface. The unstructured mesh files (hexahedra) have been obtained from Nasa's turbulent website (Rumsey, 2019) and contain of $2 \times 449 \times 129$ grid points (2×257 points on the surface of the airfoil) for the coarser mesh and $2 \times 897 \times 257$ grid points (2×513 points on the surface of the airfoil) for the finer mesh.

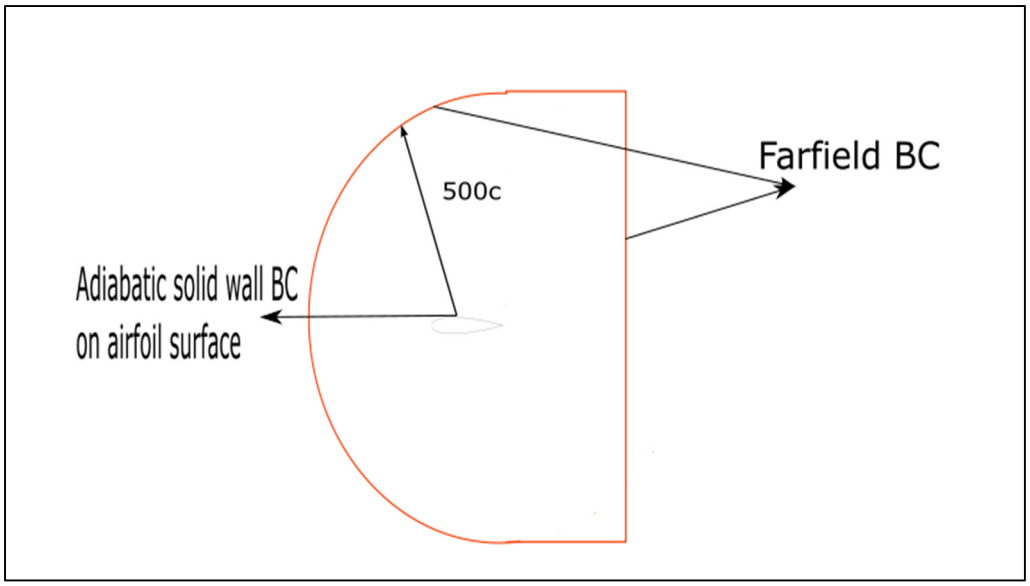

Figure 3-14 Computational domain around the NACA 0012 airfoil

The model is tested for two chord-based Reynolds numbers $Re = \frac{\rho v_\infty c}{\mu_\infty} = 1.25 \times 10^6$ and 2.25×10^6 for the finer mesh and $Re = 1.25 \times 10^6$ for the coarser mesh. The compressible flow with Mach numbers, $Ma = 0.101$ and 0.1818 is used for the finer mesh and $Ma = 0.101$ is used for the coarser mesh. The free stream temperature is set to be 288.15 K and the air's gas constant is $287.058\ {}^{N.m}/_{kg.K}$. Using the above-mentioned information with a

specific heat ratio of $\gamma = 1.4$, leads to the free stream velocity of $v_\infty = Ma\sqrt{\gamma RT} = 34.37$ & $61.866\ {}^{m}/_{S}$ for angle of attack 0°, respectively.

Viscosity is calculated using the Sutherland law with $\mu_{ref} = 1.716 \times 10^{-5}\ {}^{kg}/_{ms}$, Sutherland constant, $S = 110.4$ and Sutherland Temperature, $T_{ref} = 273.15\ K$.

$$\mu_\infty = \mu_{ref}\left(\frac{T_\infty}{T_{ref}}\right)^{3/2}\frac{T_{ref}+S}{T_\infty+S} = 1.7893 \times 10^{-5}\ {}^{N.s}/_{m^2}$$

Based on the above calculated viscosity and Reynolds number, the density is calculated with:

$$\rho_\infty = \frac{Re\mu_\infty}{v_\infty c} = 1.22\ {}^{kg}/_{m^3}$$

The perfect gas law yields $p_\infty = \rho_\infty RT_\infty = 100913\ Pa$.

The simulations have been solved iteratively using the CFL=10 with the linear solver of FGMRES using 20 linear iterations and linear error of 1×10^{-12}. The weighted least squares method is used to solve the spatial gradients. The convective numerical method for the flow is SLAU2 (Kitamura & Shima, 2013) with VENKATAKRISHNAN_WANG (Wang, 2000) as the slope limiter. For the turbulence model, the Scalar upwind method is used with VENKATAKRISHNAN_WANG as the slope limiter.

3.3.2 Mesh study

The mesh study is performed over the NACA 0012 airfoil to choose the appropriate grid size. Three mesh sizes are used including $2 \times 225 \times 65$ (2×129 points on the airfoil surface), $2 \times 449 \times 129$ (2×257 points on the airfoil surface), and $2 \times 897 \times 257$ (2×513 points

on the airfoil surface). In this study, the transition points for the above-mentioned grid sizes without roughness at $Re = 1.25 \times 10^6$ are studied and compared to the literature.

Figure 3-15 compares different flow regions using different grid sizes and experimental data for the smooth NACA 0012. In this figure, the red color is used for the laminar flow, light red is used for the transitional flow, and white is used to show the turbulent region. Similar to the flat plate test cases, the start of the transition region is the point at which the skin friction coefficient value begins to increase, and the end of the transition region is the point at which it stops increasing. This is accomplished through a manual verification of the data.

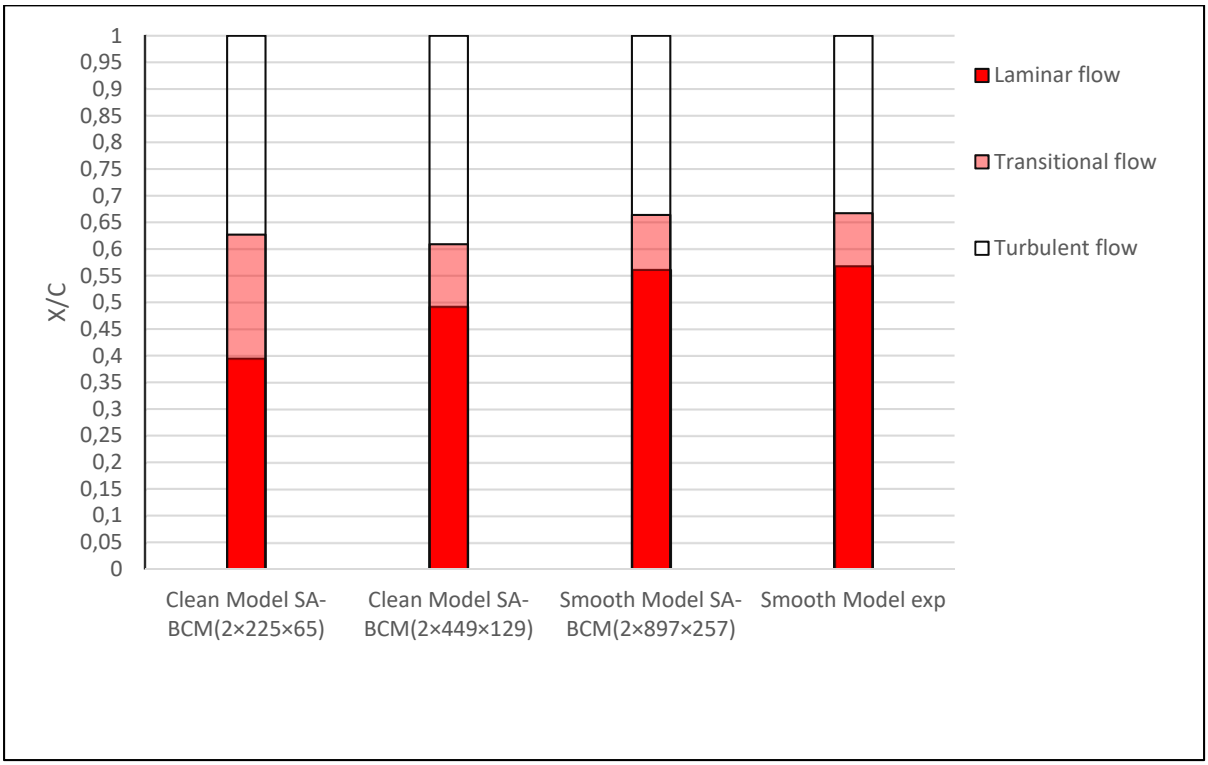

Figure 3-15 Comparison of the flow regions using different grid sizes and experimental data over smooth NACA 0012

It can be seen that refining the mesh size causes the transition onset location to move downstream as observed for the flat plate. Additionally, the transition length is decreased by refining the mesh. The grid size $2 \times 897 \times 257$ predicts the same transition and turbulent flow

onset location as the experimental data, around $\frac{X}{C} = 0.57$ and $\frac{X}{C} = 0.67$, respectively. The finest grid size is used in this study to validate the roughness correlation.

3.3.3 Results at $Re = 1.25 \times 10^6$

3.3.3.1 Smooth NACA 0012 convergence

In this section, the convergence figures for the smooth airfoil simulation using the finest mesh are shown in order to make sure the results are converged. Residual flows including density, momentum, and energy are plotted against the number of iterations in figure 3-16. The flow residuals are shown on the Y-axis and the number of iterations is illustrated on the X-axis. It can be seen that the residuals are constant after 170000 iterations.

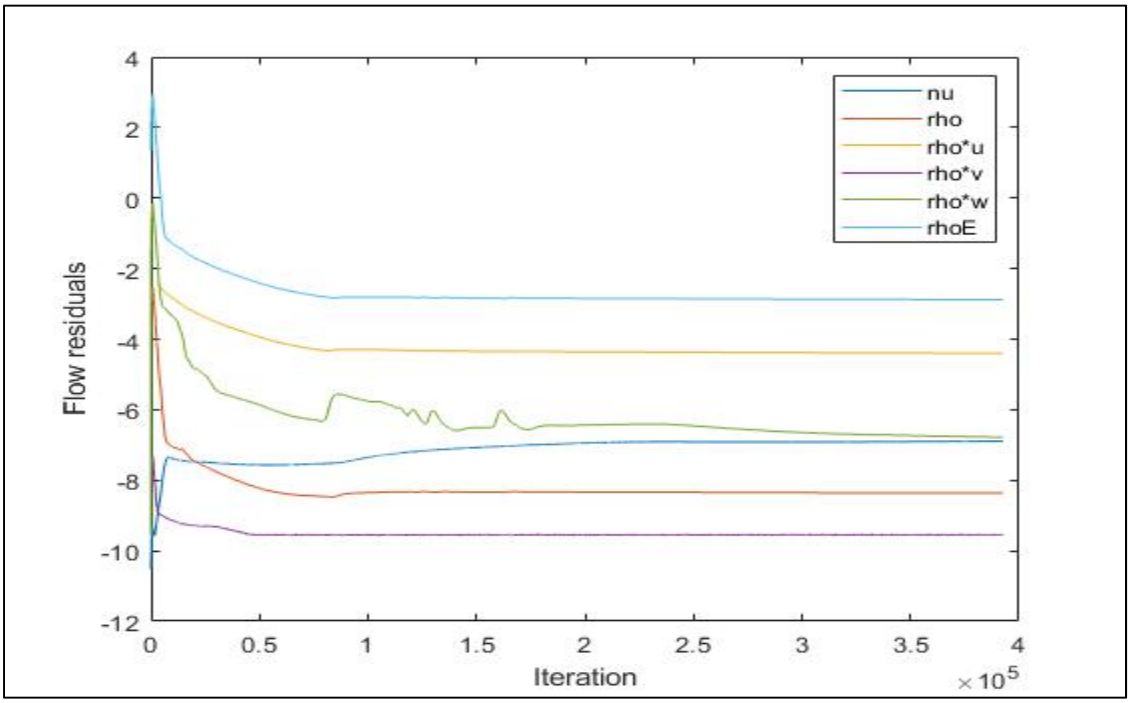

Figure 3-16 Flow residuals vs. number of iterations for smooth NACA 0012 at $Re = 1.25 \times 10^6$

In addition to the flow residuals, the drag and lift coefficients evolutions are plotted in figures 3-17 and 3-18, respectively. In these figures, the drag and lift coefficients are plotted on the Y-axis and the number of iterations is plotted on the X-axis.

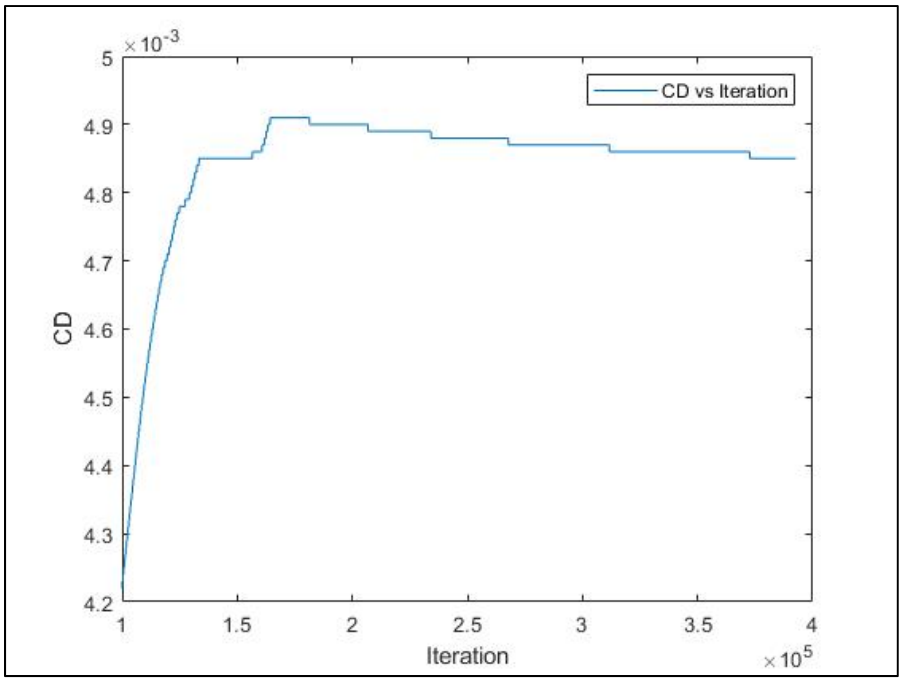

Figure 3-17 Drag coefficient evolution for smooth NACA 0012 at $Re = 1.25 \times 10^6$

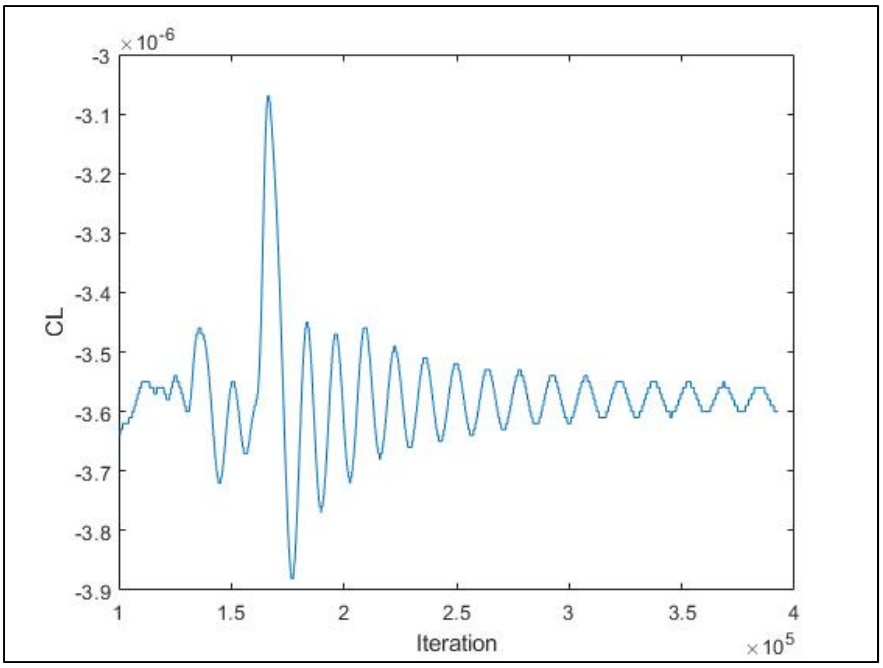

Figure 3-18 Lift coefficient evolution for smooth NACA 0012 at $Re = 1.25 \times 10^6$

In figure 3-17, the drag coefficient does not change significantly after 170000 iterations and is approximately 4.85×10^{-3}. From figure 3-18 it can be understood that the lift coefficient is oscillating. However, the amplitude of the fluctuation is small. The average value of the lift coefficient after 300000 iterations is around 3.65×10^{-6} compared to the literature (Rumsey, 2021) which is 0. Overall, the above-mentioned figures show that the lift and drag coefficients are converged.

3.3.3.2 Smooth NACA 0012 transition point

Figures 3-19 and 3-20 show the pressure coefficient and Mach number iso contours, respectively. In figure 3-19, at the stagnation point, the maximum value of the pressure coefficient occurs. The stagnation point can be found at the airfoil leading edge in figure 3-20.

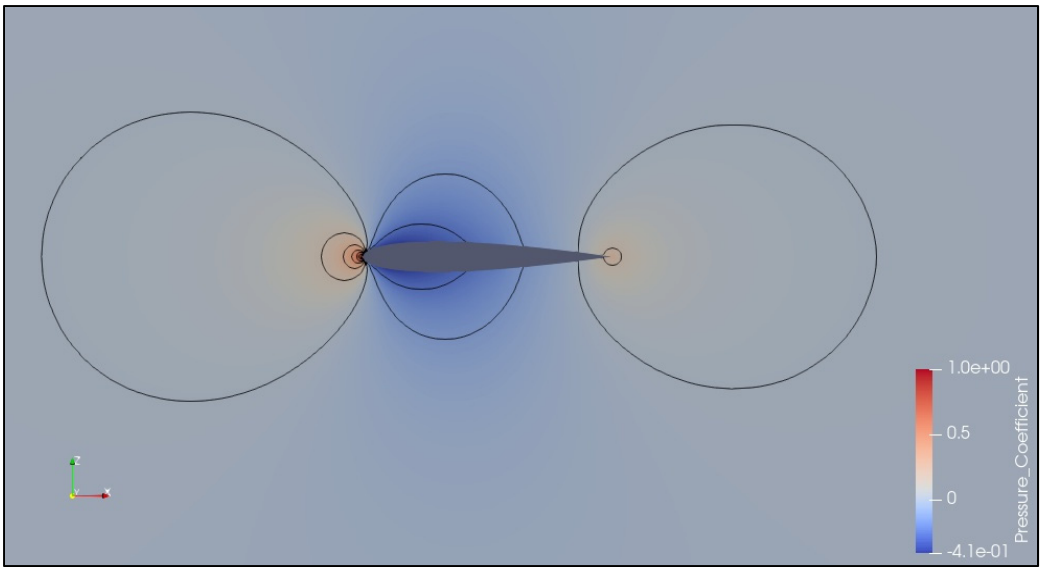

Figure 3-19 Pressure coefficient iso-contour for smooth NACA 0012 at $Re = 1.25 \times 10^6$

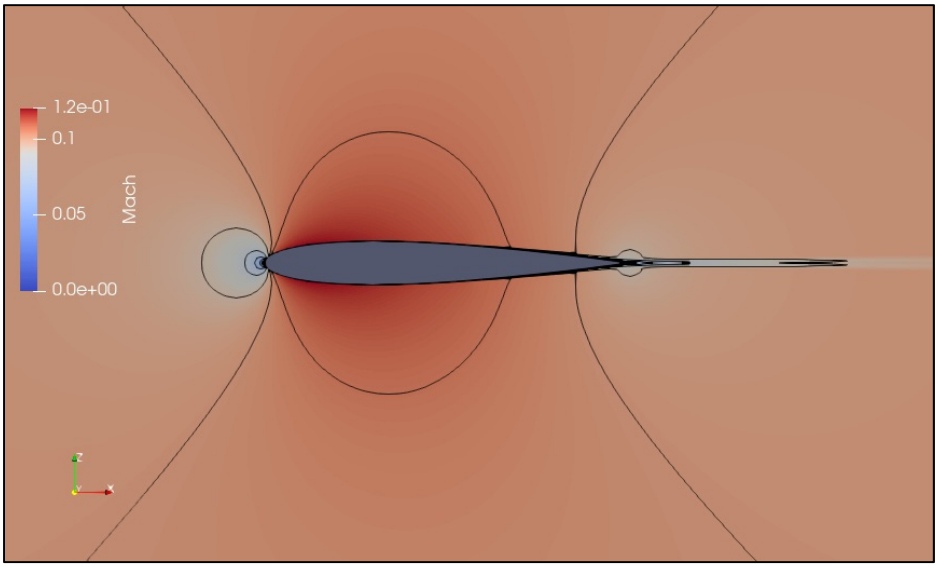

Figure 3-20 Mach number iso-contour for smooth NACA 0012 at $Re = 1.25 \times 10^6$

Figure 3-21 shows the skin friction coefficient of the upper surface against the $\frac{x}{c}$. The flow is laminar until it reaches the transition point at $\frac{x}{c} = 0.561$. The transition region ends at $\frac{x}{c} =$

0.664 where the skin friction coefficient stops increasing. The flow is turbulent after the mentioned point.

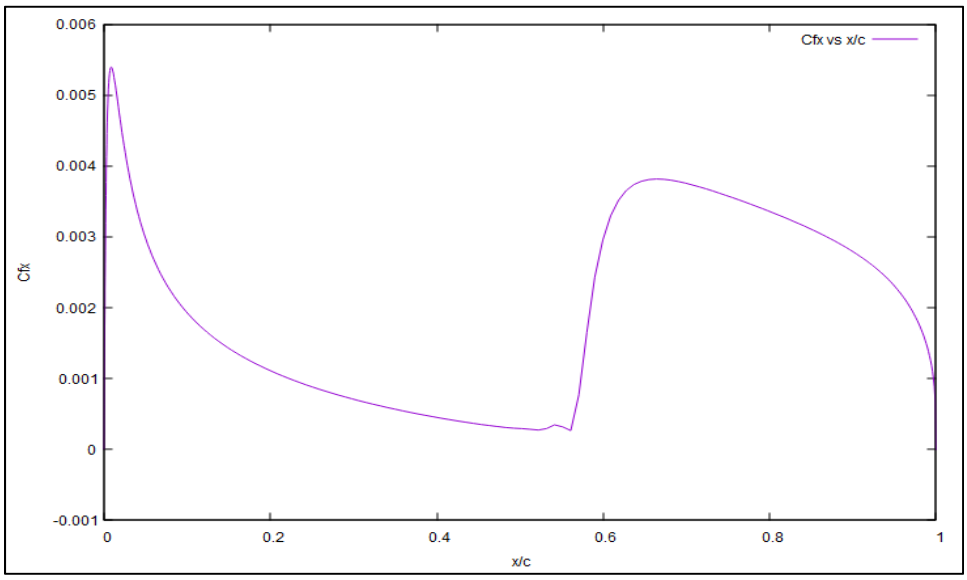

Figure 3-21 Skin friction coefficient versus x/c for smooth NACA 0012 at $Re = 1.25 \times 10^6$

The pressure coefficient is plotted against $\frac{x}{c}$ in figure 3-22. It can be seen that the SA-BCM model captures the transition point at $\frac{x}{c} = 0.561$ which demonstrates the transition onset location.

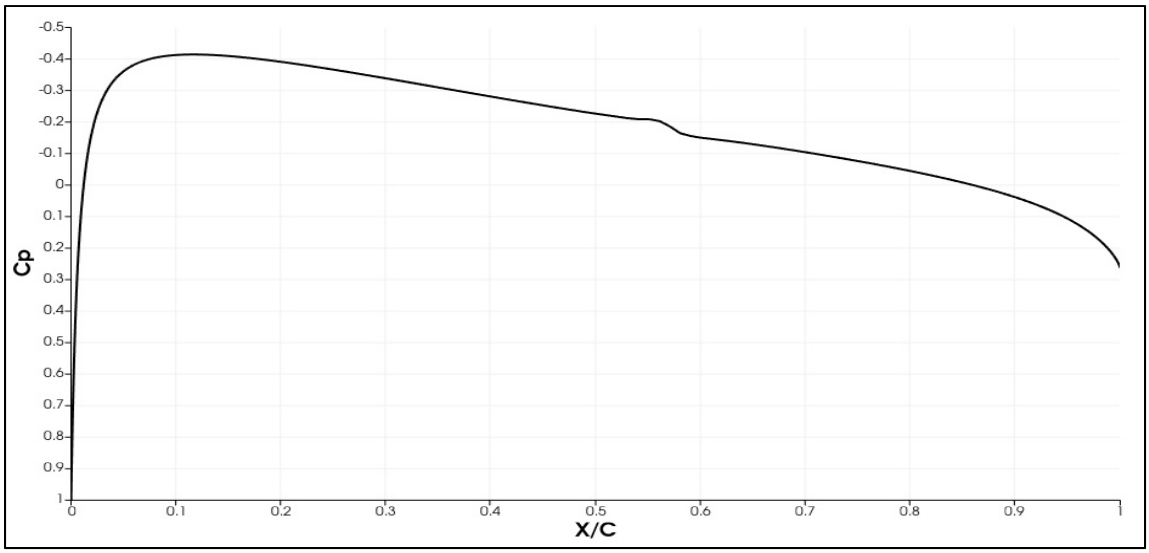

Figure 3-22 Pressure coefficient versus x/c for smooth NACA 0012 at $Re = 1.25 \times 10^6$

Figure 3-23 shows the different flow regions on the NACA 0012. SA-BCM model is compared with the experimental results of (Kerho & Bragg, 1997) and the CFD results of (Langel et al., 2017). It is clear that the SA-BCM model is able to predict the transition location. The model can also estimate when the transition ends as well as the length of the transition region compared to the experimental data. Moreover, it can be seen that the SA-BCM model does a better job in predicting the transition location compared to the CFD results of (Langel et al., 2017) for this test case.

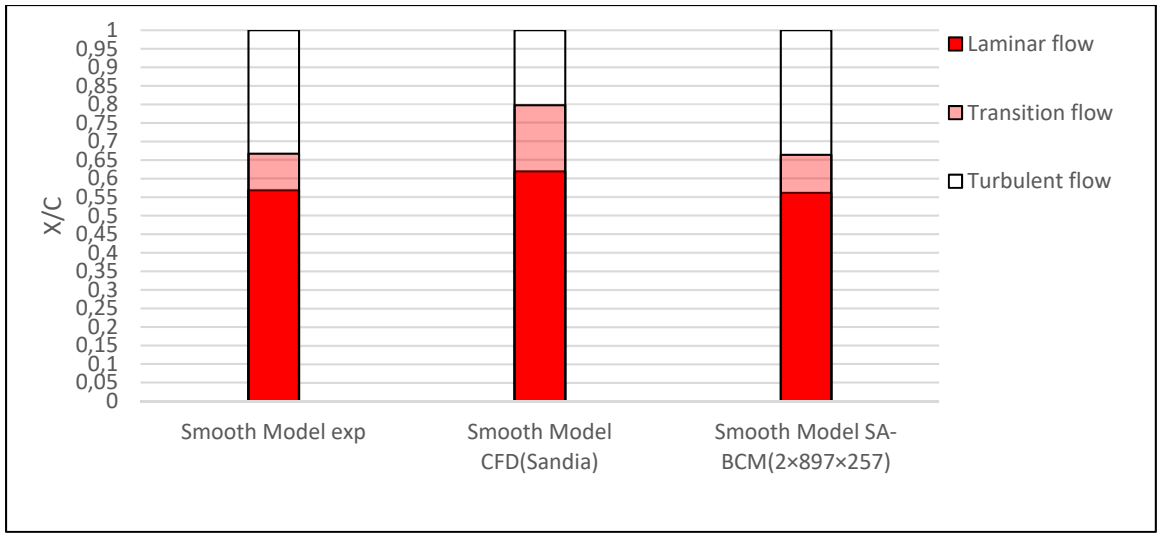

Figure 3-23 Comparison of different flow regions for smooth NACA 0012 at $Re = 1.25 \times 10^6$

3.3.3.3 Rough NACA 0012 convergence

Before illustrating the result of the airfoil with distributed roughness, the convergence of the simulation is studied. This study is done with the roughness correlation activated and applying $k_s = 6.94 \times 10^{-4}\ m$ ($Re_{k_s} = 1626$) over the same grid size ($2 \times 897 \times 257$) as the smooth model. It needs to be noted that the reason for choosing this grid size is that it is assumed that adding roughness would give the same results for the mesh study as section 3.3.2.

Figure 3-24 illustrates the log-residual convergence. It can be seen that the residuals are constant after 50000 iterations. Similar to the smooth model, the drag and lift coefficients evolutions are shown in figures 3-25 and 3-26, respectively.

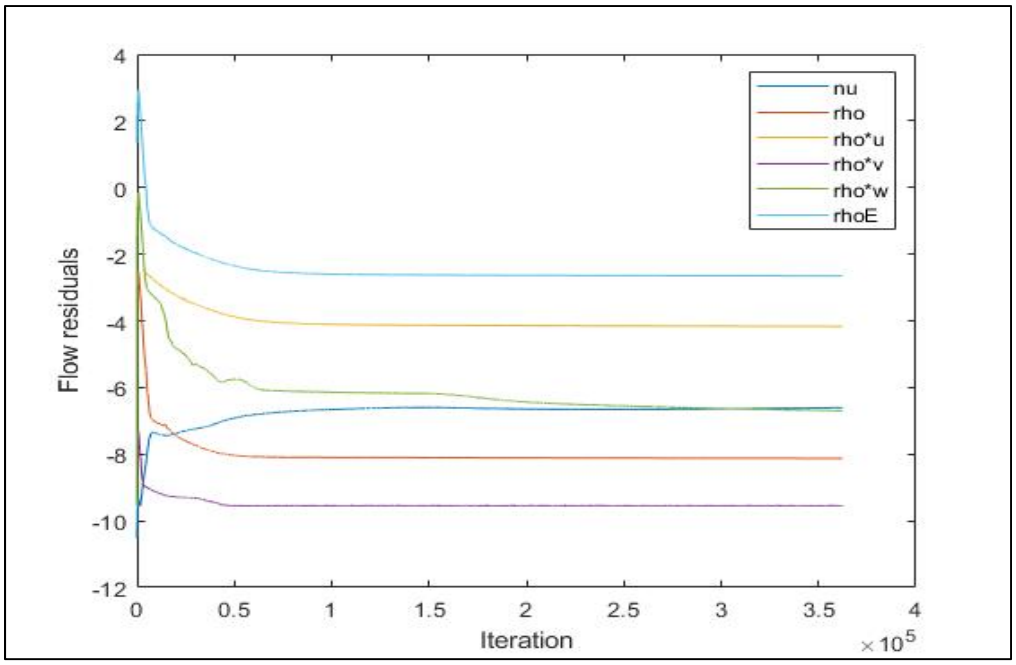

Figure 3-24 Flow residuals vs. number of iterations for rough NACA 0012 at $Re = 1.25 \times 10^6$

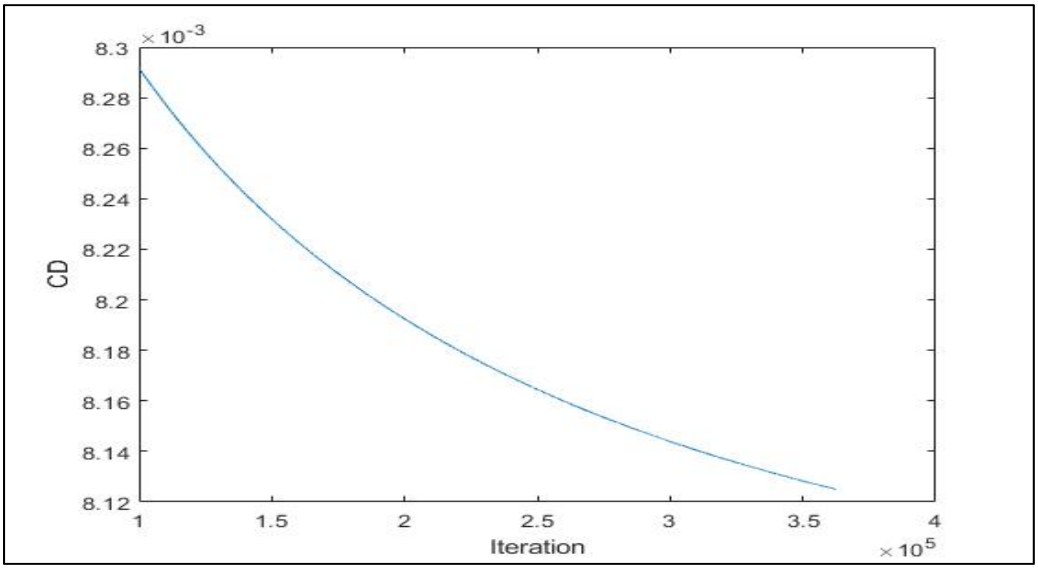

Figure 3-25 Drag coefficient vs. number of iterations for rough NACA 0012 at $Re = 1.25 \times 10^6$

Table 3.3 Drag coefficient variation at different iterations

Iteration variation	Drag coefficient variation
$10^5 - 3.6 \times 10^5$	2.00%
$2.5 \times 10^5 - 3.6 \times 10^5$	0.47%
$3 \times 10^5 - 3.6 \times 10^5$	0.23%

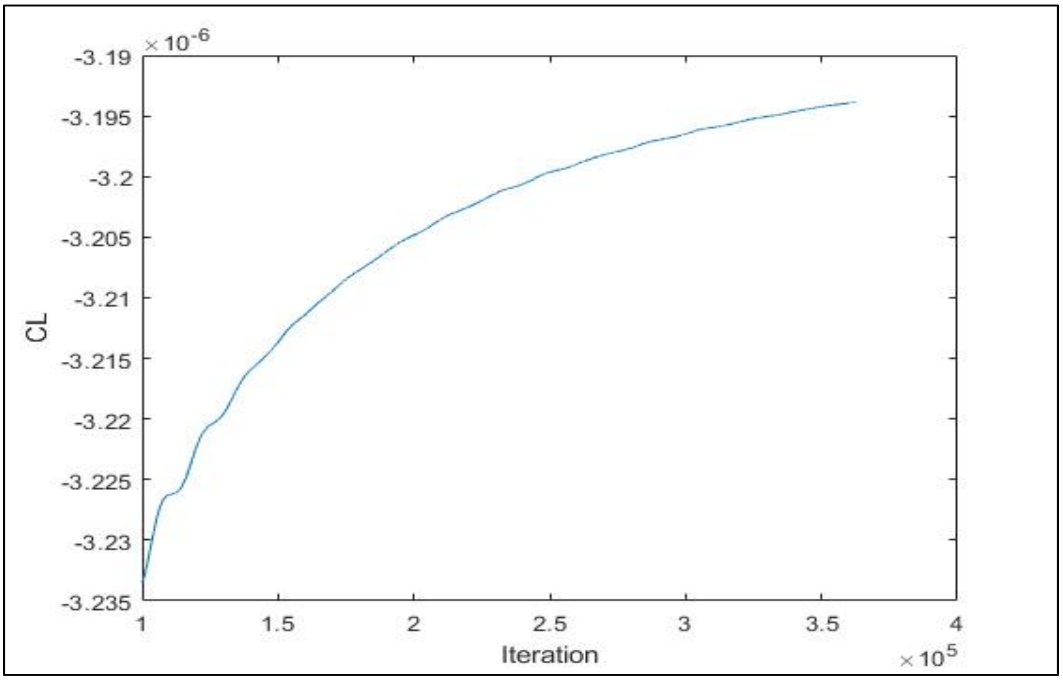

Figure 3-26 Lift coefficient vs. number of iterations for rough NACA 0012 at $Re = 1.25 \times 10^6$

Table 3.4 Lift coefficient variation at different iterations

Iteration variation	Lift coefficient variation
$10^5 - 3.6 \times 10^5$	1.22%
$2.5 \times 10^5 - 3.6 \times 10^5$	0.18%
$3 \times 10^5 - 3.6 \times 10^5$	0.087%

It can be understood from figure 3-25 that the drag coefficient evolved from 0.00823 to 0.008125 over 250000 iterations. Similarly, it can be seen in figure 3-26 that the lift coefficient evolved from -0.000003235 to -0.000003195 over the same number of iterations. Table 3 and 4 show the variation of the drag and lift coefficients at various iterations, respectively. It is clear that, the changes in the lift and drag coefficients are small and it can be concluded that these values are converged.

3.3.3.4 Rough NACA 0012 transition point

The pressure coefficient and Mach number iso-contours are shown in figures 3-27 and 3-28, respectively. Figure 3-27 shows that the highest value of the pressure coefficient occurs near the stagnation point. In figure 3-28, the stagnation point is located near the leading edge of the airfoil.

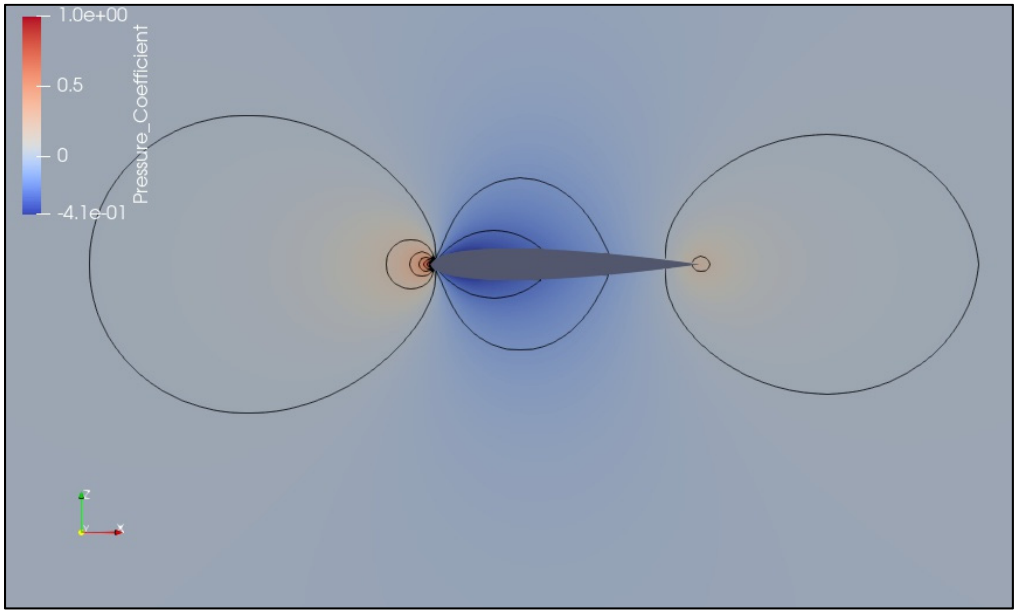

Figure 3-27 Pressure coefficient iso-contour for rough NACA 0012 at $Re = 1.25 \times 10^6$

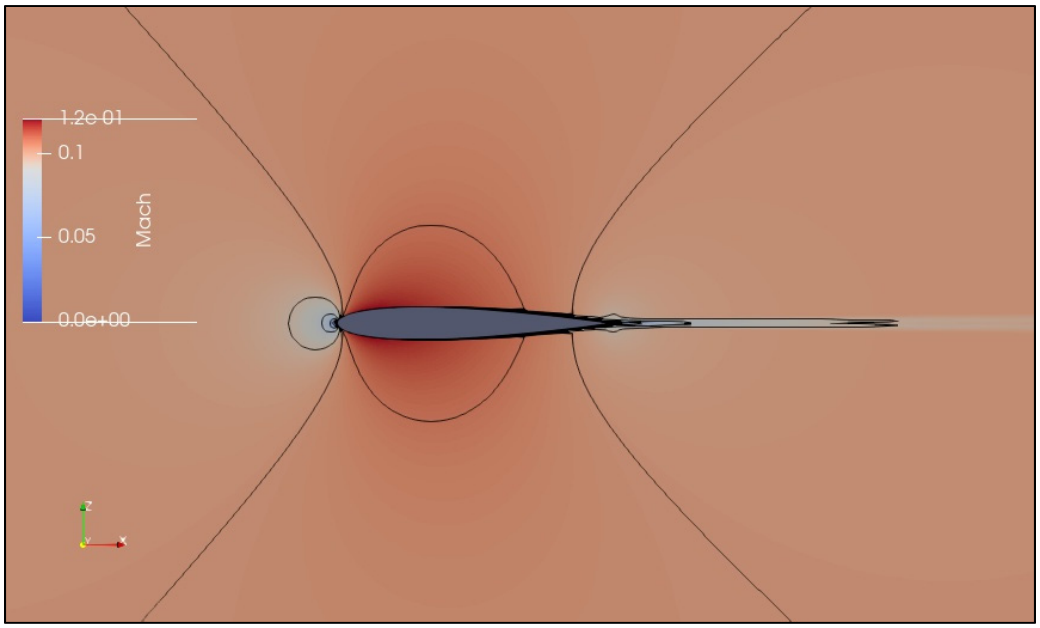

Figure 3-28 Mach number iso-contour for rough NACA 0012
at $Re = 1.25 \times 10^6$

The skin friction coefficient on the upper surface of the rough airfoil is plotted in figure 3-29. The skin friction coefficients are represented on the Y-axis, while the $\frac{x}{c}$ values are plotted on the X-axis in this figure. The flow is laminar until it reaches the transition point at $\frac{x}{c} = 0.17$, as can be seen. After $\frac{x}{c} = 0.23$, the skin friction coefficient stops growing, the flow becomes turbulent, and the transition region ends.

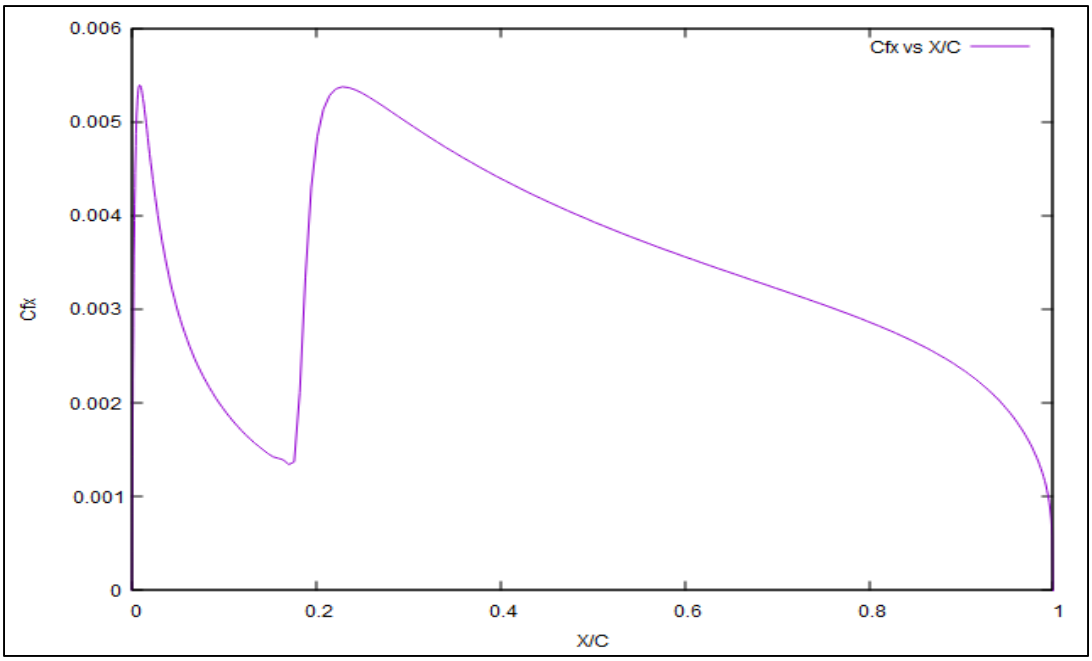

Figure 3-29 Skin friction coefficient in x direction vs. x/c for rough NACA 0012 at $Re = 1.25 \times 10^6$

In figure 3-30, the pressure coefficient is shown versus $\frac{x}{c}$ and the transition point at $\frac{x}{c} = 0.17$ is captured by the SA-BCM model.

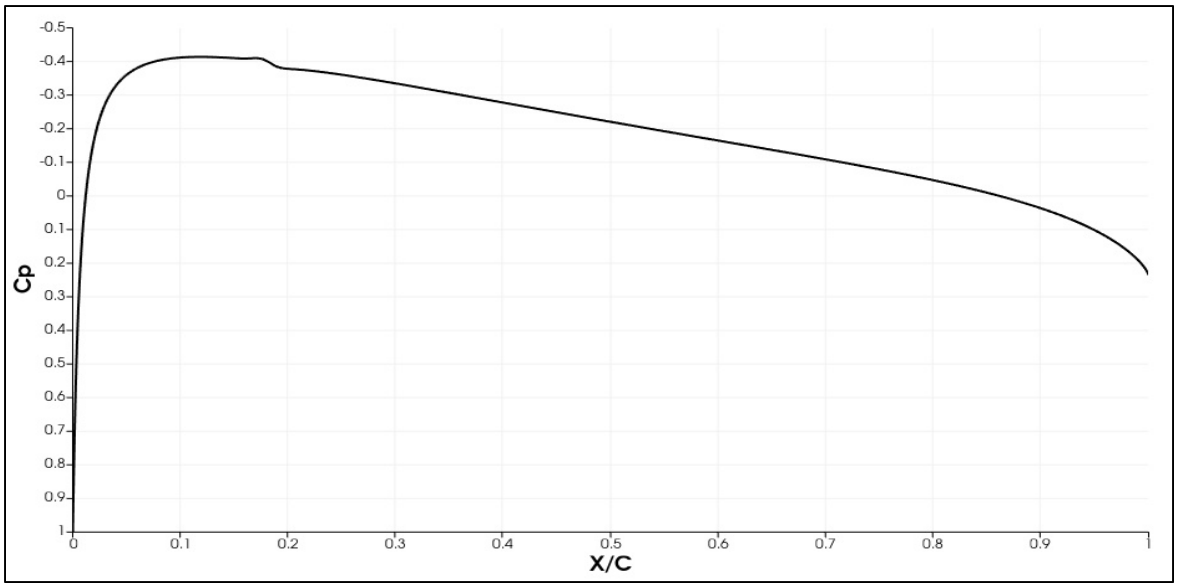

Figure 3-30 Pressure coefficient distribution over NACA 0012 with distributed roughness at $Re = 1.25 \times 10^6$

Figure 3-31 compares different flow regions of our simulation with an activated roughness correlation to the experimental and CFD data. As mentioned in section 3.3, the experimental reference used different roughness lengths and different locations over the airfoil which has been plotted in figure 3-31 to ease the comparison between the fully rough airfoil and the experimental results.

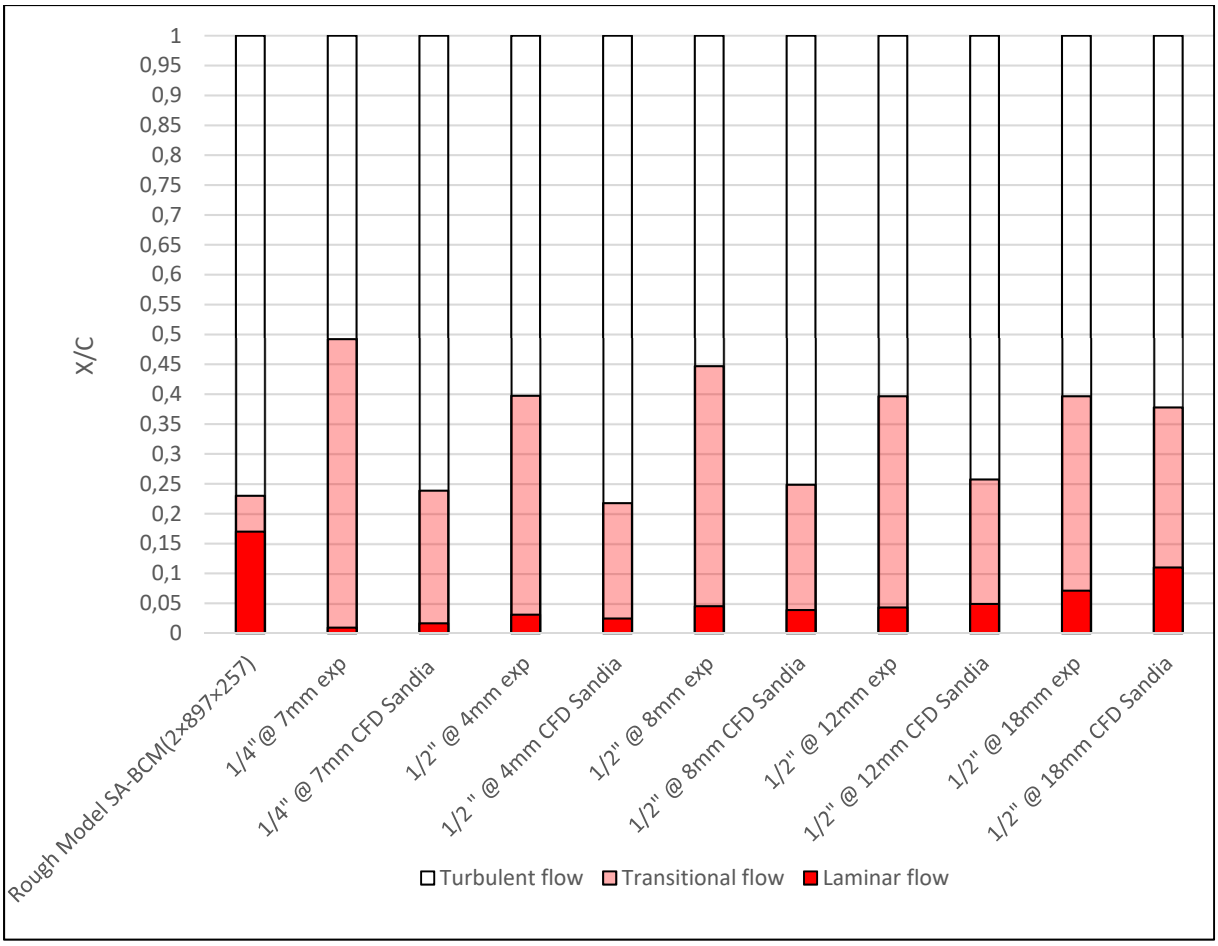

Figure 3-31 Comparison of different flow regions over NACA 0012 with distributed roughness at $Re = 1.25 \times 10^6$

The SA-BCM model is in good agreement with CFD data of (Langel et al., 2017) in terms of locating the start of the turbulent flow in most cases. However, it has a larger delay in predicting the start of the transition region compared to the experimental and CFD results. An important trend that is clear by comparing figures 3-23 and 3-31 is that the transitional region length increases by applying roughness in the experimental results. This can be responsible for the late prediction of the transition location and cause the boundary layer to grow too rapidly in our simulation since there is no parameter in the underlying SA-BCM model to take the transitional length into account. The same problem has been reported in (Langel et al., 2017). Experimental data in figure 3-31 illustrates that the transitional region appears to be insensitive

to the location of the roughness (Kerho & Bragg, 1997). On the other hand, extending the roughness length is shown to decrease the transition region length (Kerho & Bragg, 1997).

3.3.4 Results at $Re = 2.25 \times 10^6$

The same NACA 0012 airfoil is simulated at Reynolds number, $Re = 2.25 \times 10^6$. The same steps as the results for $Re = 1.25 \times 10^6$ are taken to ensure the convergence of the smooth and rough simulations.

3.3.4.1 Smooth airfoil convergence

To ensure that the results are converged, the convergence values for the smooth airfoil simulation using the finest mesh are provided in this section. In figure 3-32, log-residuals such as density, momentum, and energy are displayed versus the number of iterations. The number of iterations is represented on the X-axis, while the flow residuals are shown on the Y-axis. The residuals are constant after about 75000 iterations, as would be observed.

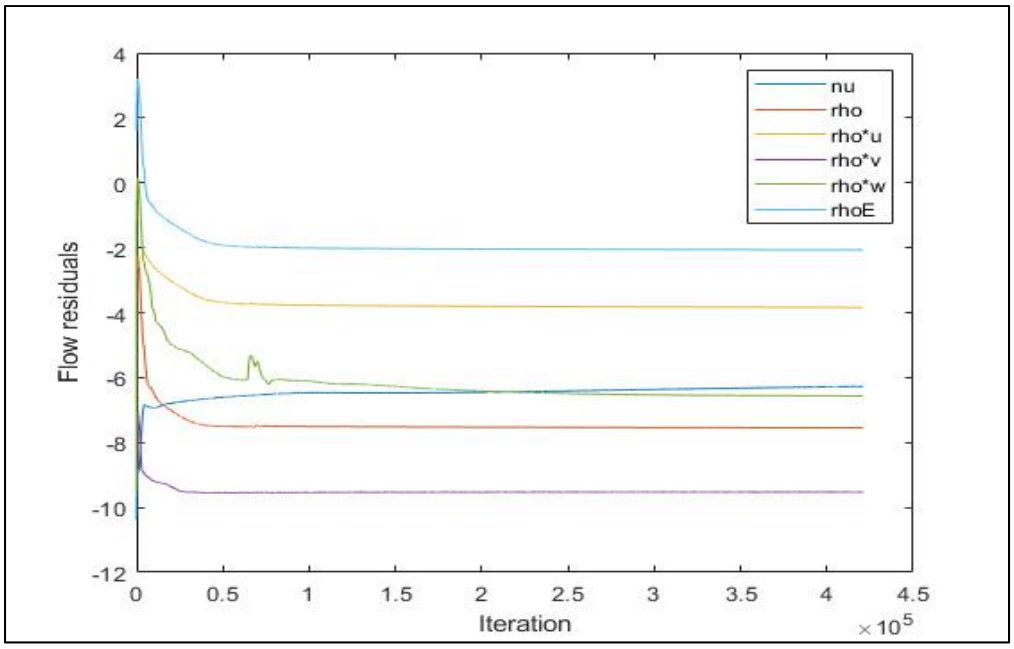

Figure 3-32 Flow residuals vs. number of iterations for smooth NACA 0012 at $Re = 2.25 \times 10^6$

Figures 3-33 and 3-34 show the drag and lift coefficients evolution, respectively. The number of iterations is displayed on the X-axis, while the drag and lift coefficients are plotted on the Y-axis.

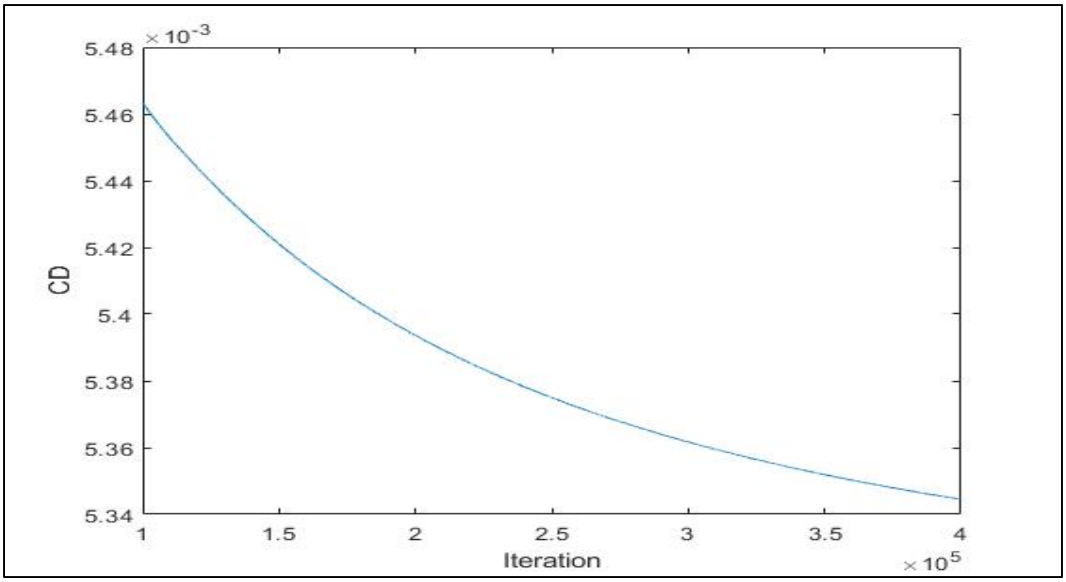

Figure 3-33 Drag coefficient vs. number of iterations for smooth NACA 0012 at $Re = 2.25 \times 10^6$

Table 3.5 Drag coefficient variation at different iterations

Iteration variation	Drag coefficient variation
$10^5 - 3.6 \times 10^5$	2.05%
$2.5 \times 10^5 - 3.6 \times 10^5$	0.46%
$3 \times 10^5 - 3.6 \times 10^5$	0.2%

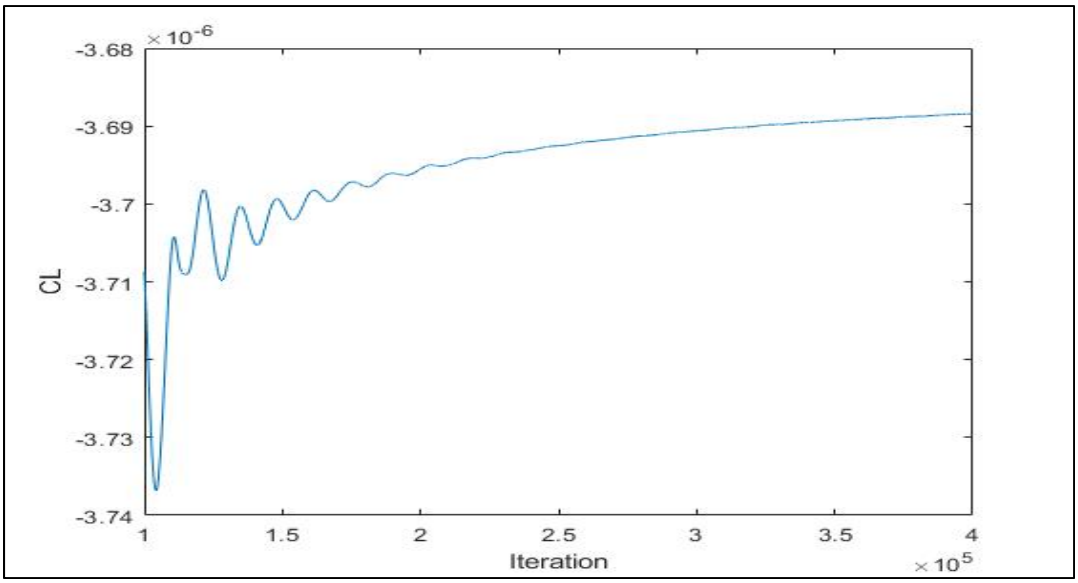

Figure 3-34 Lift coefficient vs. number of iterations for smooth NACA 0012 at $Re = 2.25 \times 10^6$

Table 3.6 Lift coefficient variation at different iterations

Iteration variation	Lift coefficient variation
$1.5 \times 10^5 - 3.6 \times 10^5$	0.3%
$2.5 \times 10^5 - 3.6 \times 10^5$	0.08%
$3 \times 10^5 - 3.6 \times 10^5$	0.04%

Figure 3-33 shows that the drag coefficient does not change considerably, decreasing from 0.00546 at 100000 to 0.005345 at 400000. The lift coefficient oscillates, as shown in figure 3-34. The fluctuation's magnitude, however, is rather minor and stops at 250000. After that point, the lift coefficient slightly increases to peak above -0.00000369. The variation of the drag and lift coefficients over several iterations is seen in Tables 5 and 6, respectively. Since the variations in the lift and drag coefficients are minimal, it is reasonable to assume that these values have converged.

3.3.4.2 Smooth NACA 0012 transition point

Figures 3-35 and 3-36 depict the pressure coefficient and Mach number iso-contours, respectively. The highest value of the pressure coefficient occurs around the stagnation point, as shown in figure 3-35. The stagnation point in figure 3-36 is at the leading edge of the airfoil. The same trend has been seen for the lower Reynolds number ($Re = 1.25 \times 10^6$).

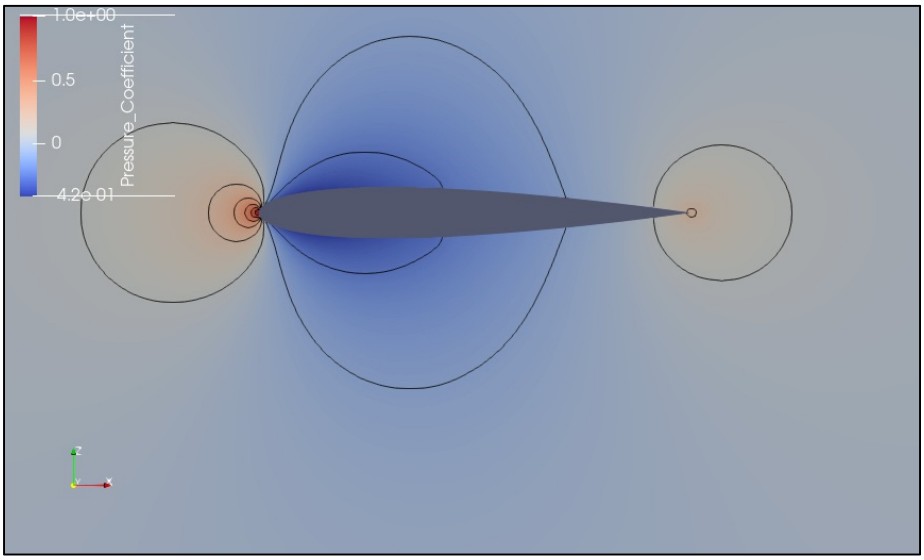

Figure 3-35 Pressure coefficient iso-contour for smooth NACA 0012 at $Re = 2.25 \times 10^6$

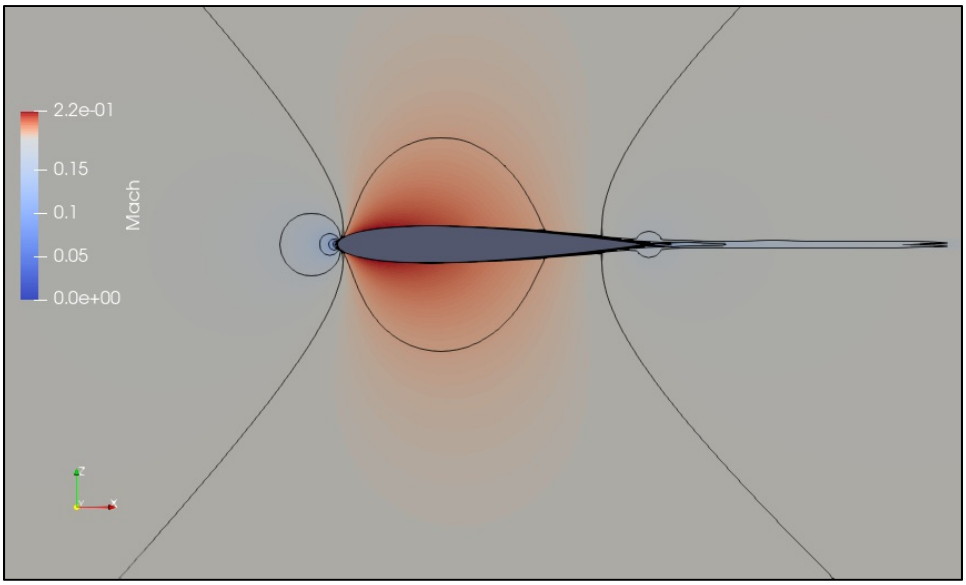

Figure 3-36 Mach number iso-contour for smooth NACA 0012 at $Re = 2.25 \times 10^6$

The skin friction coefficient on the top surface against $\frac{x}{c}$ is shown in Figure 3-37. The flow is laminar until it hits the transition point at $\frac{x}{c} = 0.40$, as can be observed. After $\frac{x}{c} = 0.482$, the skin friction coefficient stops growing, the flow becomes turbulent, and the transition area ends.

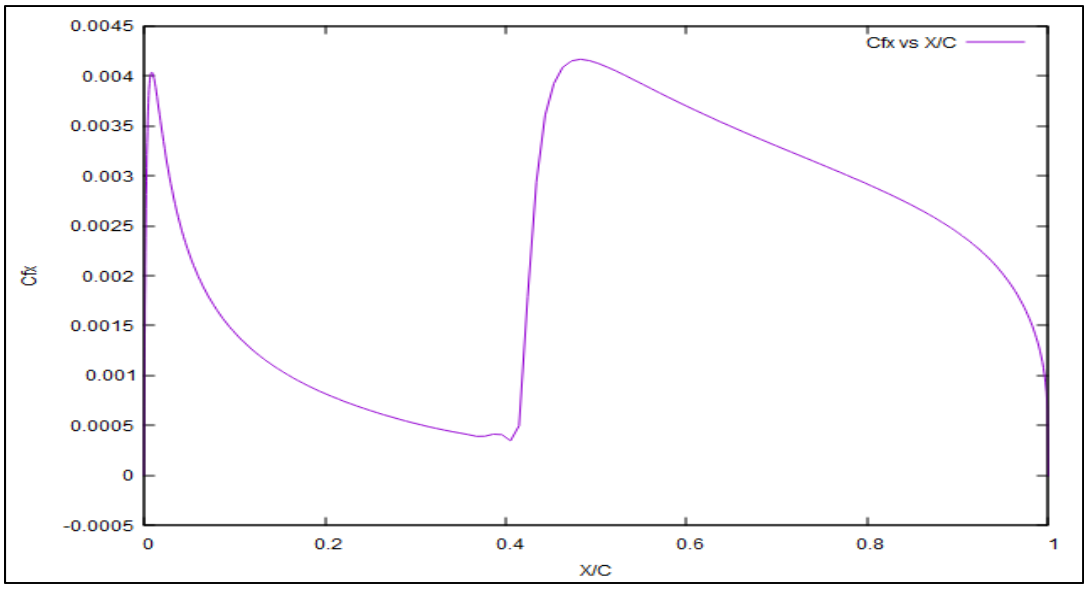

Figure 3-37 Skin friction coefficient in x direction vs. x/c for smooth NACA 0012 at $Re = 2.25 \times 10^6$

In figure 3-38, the pressure coefficient is shown versus $\frac{x}{c}$. The transition point at $\frac{x}{c} = 0.4$ is captured by the SA-BCM model, demonstrating the transition onset position.

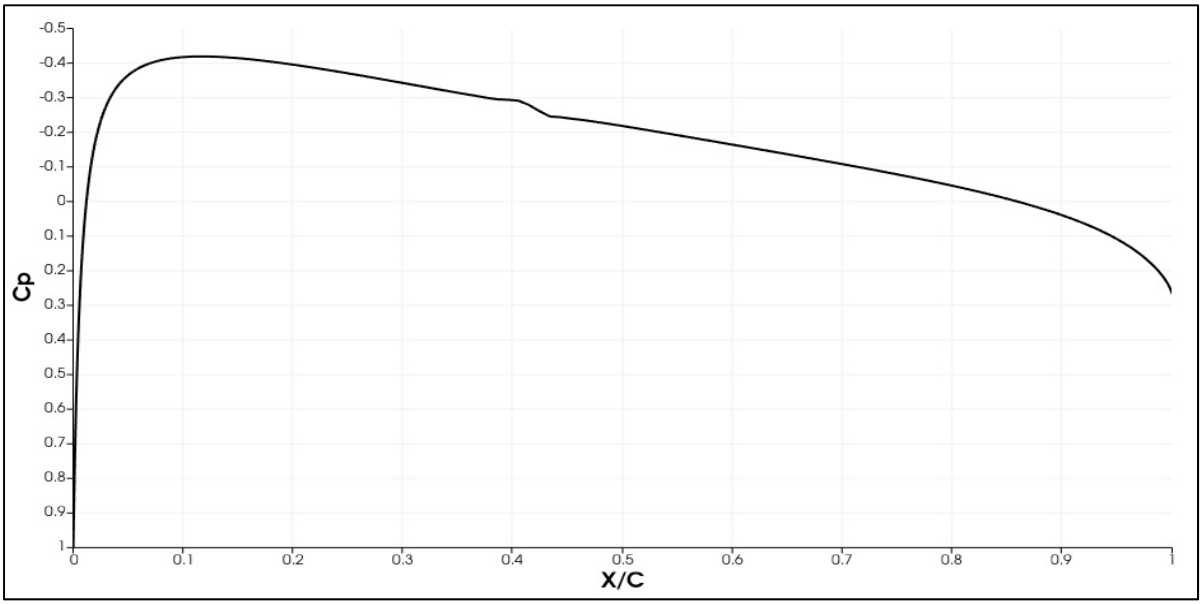

Figure 3-38 pressure coefficient distribution over smooth NACA 0012 at $Re = 2.25 \times 10^6$

The different flow zones on the airfoil are represented in figure 3-39. In terms of anticipating the transition position, the SA-BCM model agrees with the experiment results. In addition, the turbulent flow prediction matches the experimental data of (Kerho & Bragg, 1997).

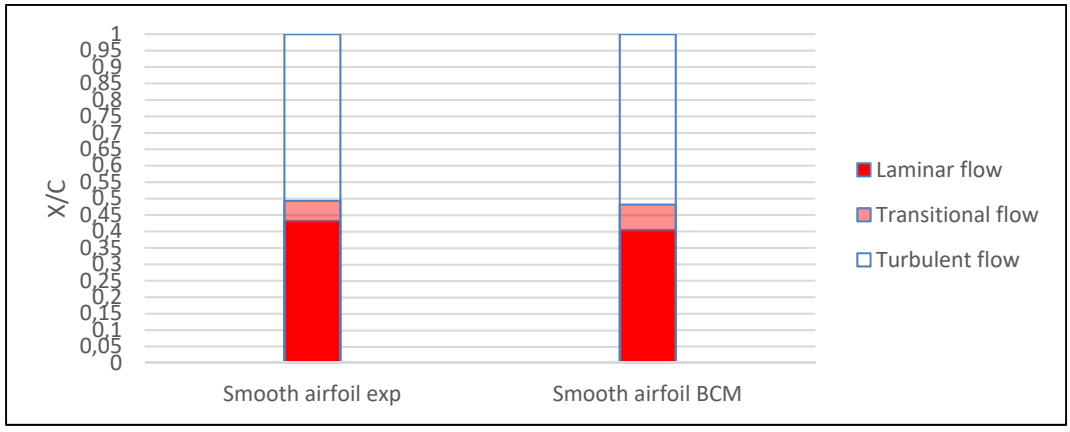

Figure 3-39 Comparison of different flow regions of the smooth NACA 0012 with the experimental data at $Re = 2.25 \times 10^6$

3.3.4.3 Rough NACA 0012 convergence

Before showing the results of the airfoil with distributed roughness, the simulation's convergence is studied. In this study, the roughness transition correlation is activated, and $k_s = 6.94 \times 10^{-4}\ m$ ($Re_{k_s} = 2926$) over the same grid size ($2 \times 897 \times 257$) is applied. The log-residual convergence including density, momentum, and energy are shown in figure 3-40. It is clear that after 10000 cycles, the residuals are constant.

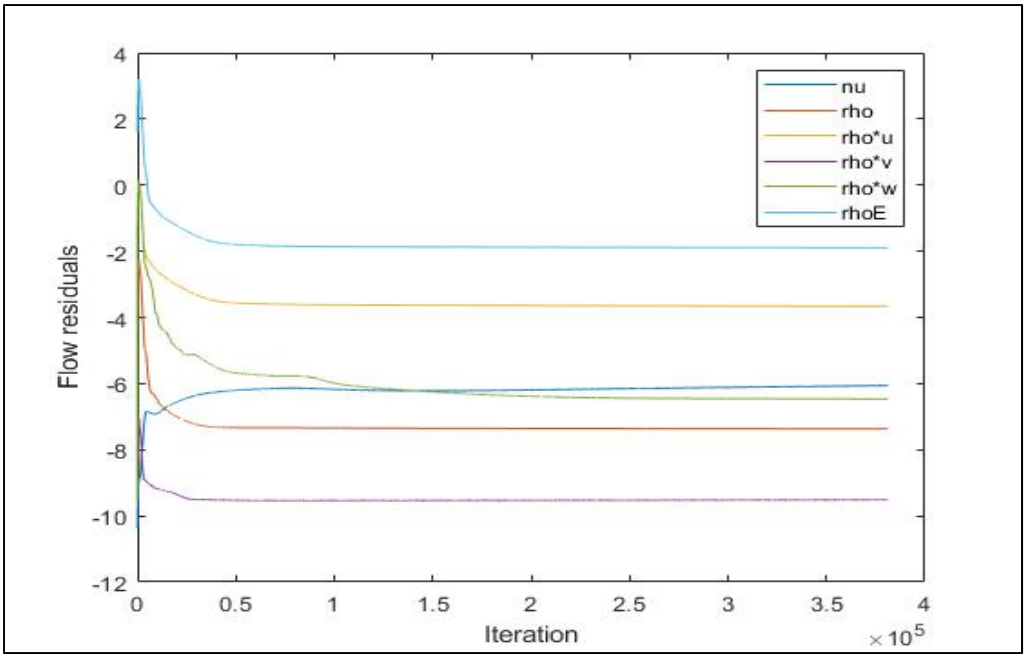

Figure 3-40 Flow residuals vs. number of iterations for rough NACA 0012 at $Re = 2.25 \times 10^6$

Figures 3-41 and 3-42 show the evolution of the drag and lift coefficients, respectively, in addition to the residual flows. The number of iterations is plotted on the X-axis, while the drag and lift coefficients are plotted on the Y-axis.

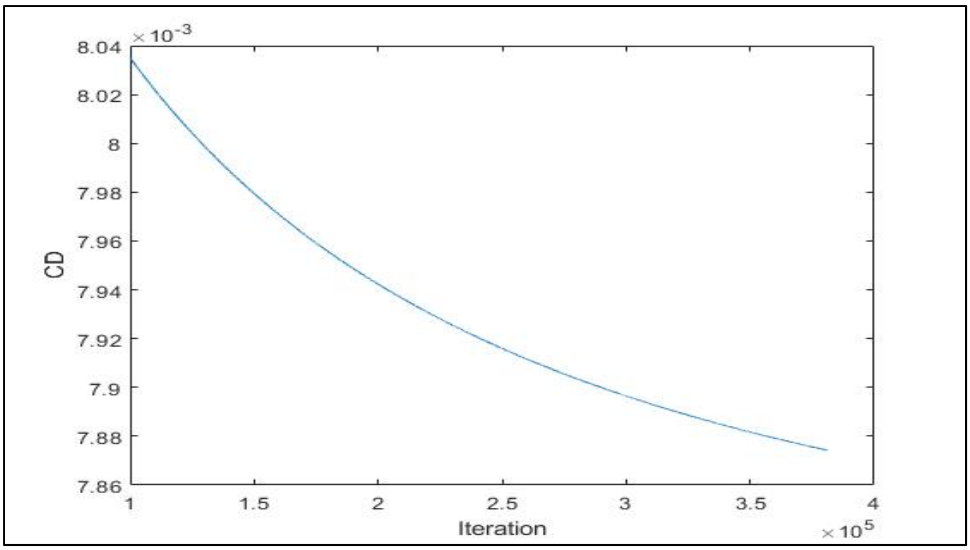

Figure 3-41 The evolution of the drag coefficient for rough NACA 0012 at $Re = 2.25 \times 10^6$

Table 3.7 Drag coefficient variation at different iterations

Iteration variation	Drag coefficient variation
$10^5 - 3.6 \times 10^5$	1.92%
$2.5 \times 10^5 - 3.6 \times 10^5$	0.46%
$3 \times 10^5 - 3.6 \times 10^5$	0.21%

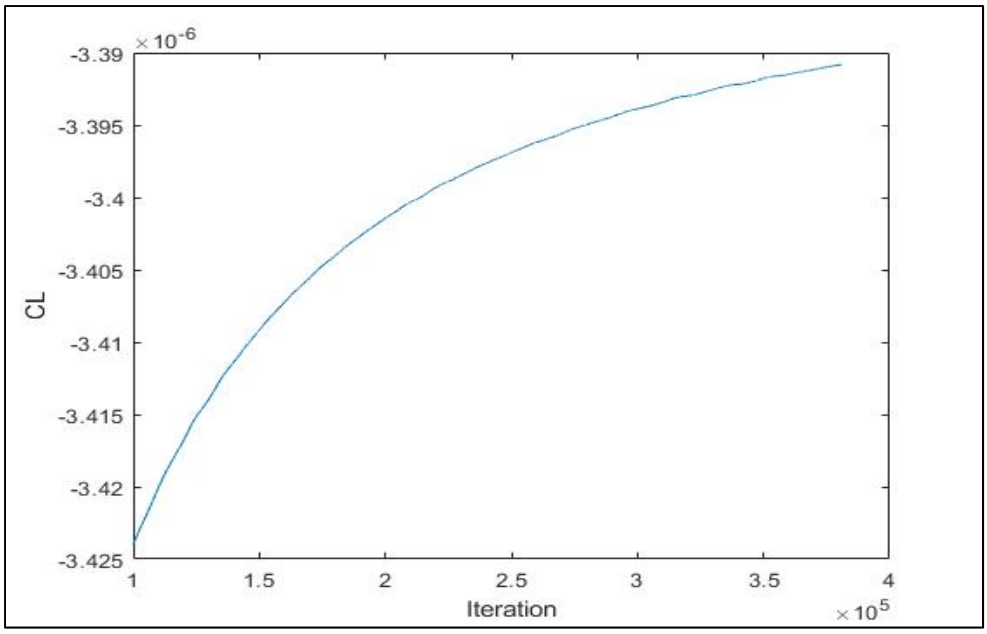

Figure 3-42 The evolution of the lift coefficient for rough NACA 0012 at $Re = 2.25 \times 10^6$

Table 3.8 Lift coefficient variation at different iterations

Iteration variation	Lift coefficient variation
$10^5 - 3.6 \times 10^5$	0.94%
$2.5 \times 10^5 - 3.6 \times 10^5$	0.16%
$3 \times 10^5 - 3.6 \times 10^5$	0.07%

The drag coefficient changes from 0.00803 to 0.00788 after more than 250000 iterations, as seen in figure 3-41. Over the same number of iterations, the lift coefficient changes from -0.000003424 to -0.000003391 in figure 3-42. Tables 7 and 8 show how the drag and lift coefficients changes after a number of iterations, respectively. It is reasonable to assume that the lift and drag coefficients have converged since the variation in these values are small.

3.3.4.4 Rough NACA 0012 transition point

The pressure coefficient and Mach number iso-contours are shown in figures 3-43 and 3-44, respectively. As illustrated in figure 3-43, the pressure coefficient reaches its maximum value around the stagnation point. The airfoil's leading edge is the stagnation point in figure 3-44. The lower Reynolds number ($Re = 1.25 \times 10^6$) has shown the same trend.

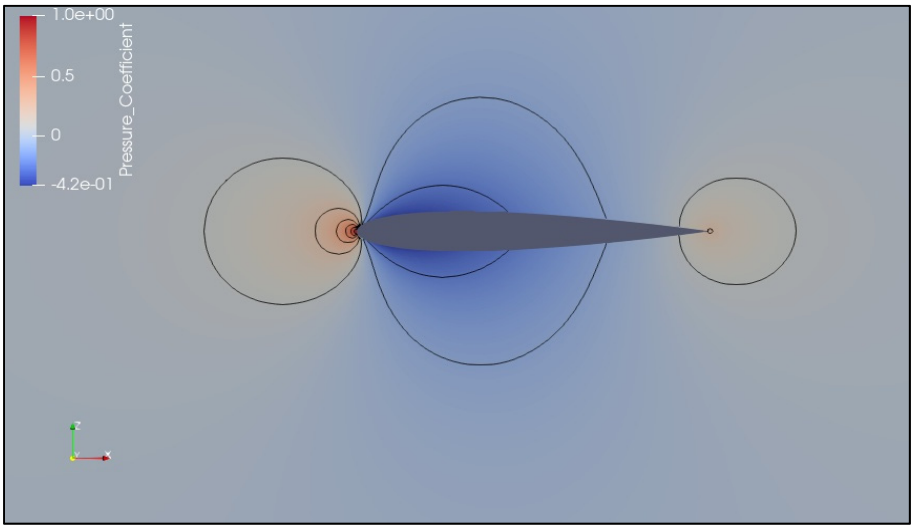

Figure 3-43 Pressure coefficient iso-contour for rough NACA 0012 at $Re = 2.25 \times 10^6$

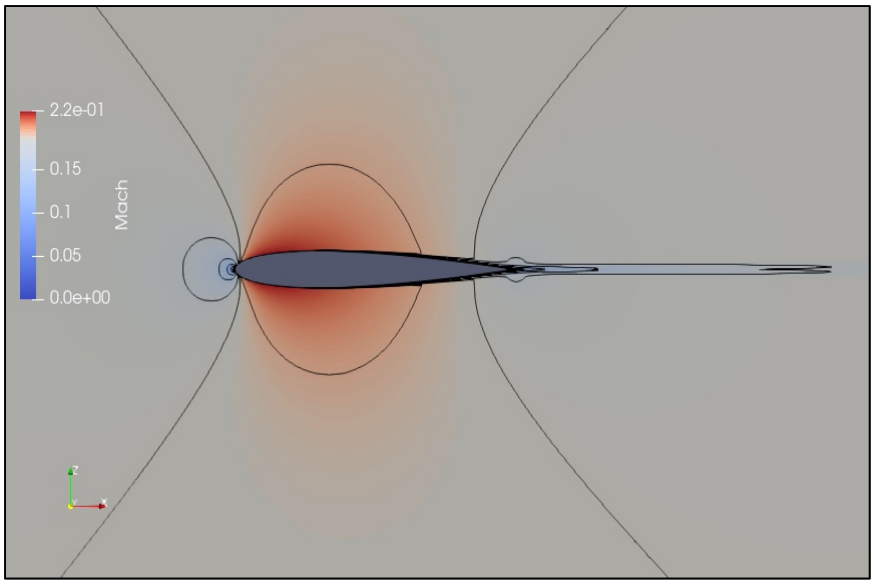

Figure 3-44 Mach number iso-contour for rough NACA 0012 at $Re = 2.25 \times 10^6$

Figure 3-45 depicts the top surface's skin friction coefficient in the x direction versus $\frac{x}{c}$. As can be seen, the flow is laminar until it reaches the transition point at $\frac{x}{c} = 0.106$. The transition zone ends at $\frac{x}{c} = 0.14$, beyond which the flow becomes turbulent.

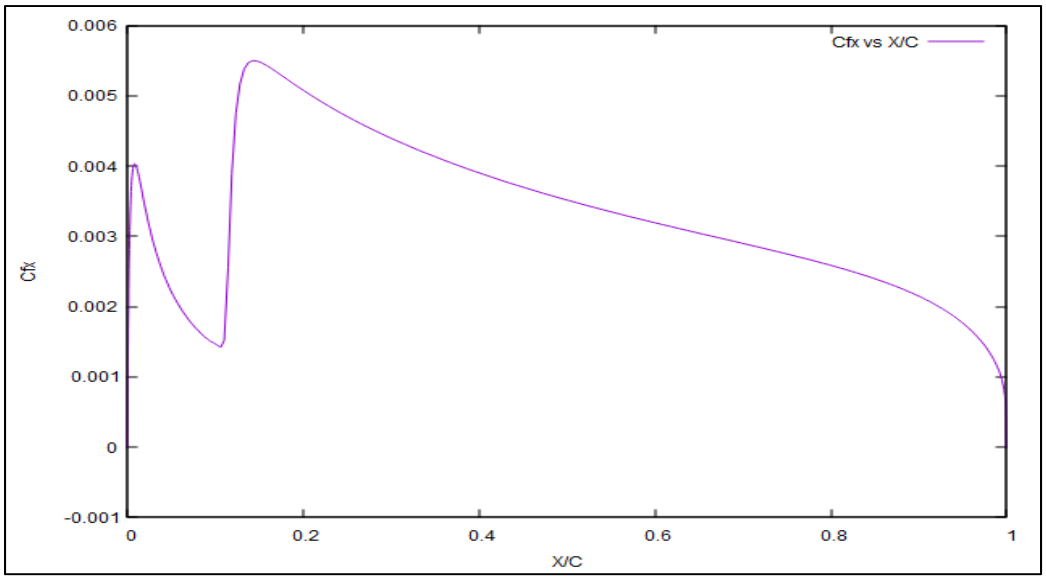

Figure 3-45 Skin friction coefficient vs. x/c over rough NACA 0012 at $Re = 2.25 \times 10^6$

The pressure coefficient is plotted against x/c in figure 3-46. The SA-BCM model captures the transition point at $\frac{x}{c} = 0.1$, illustrating the transition onset position.

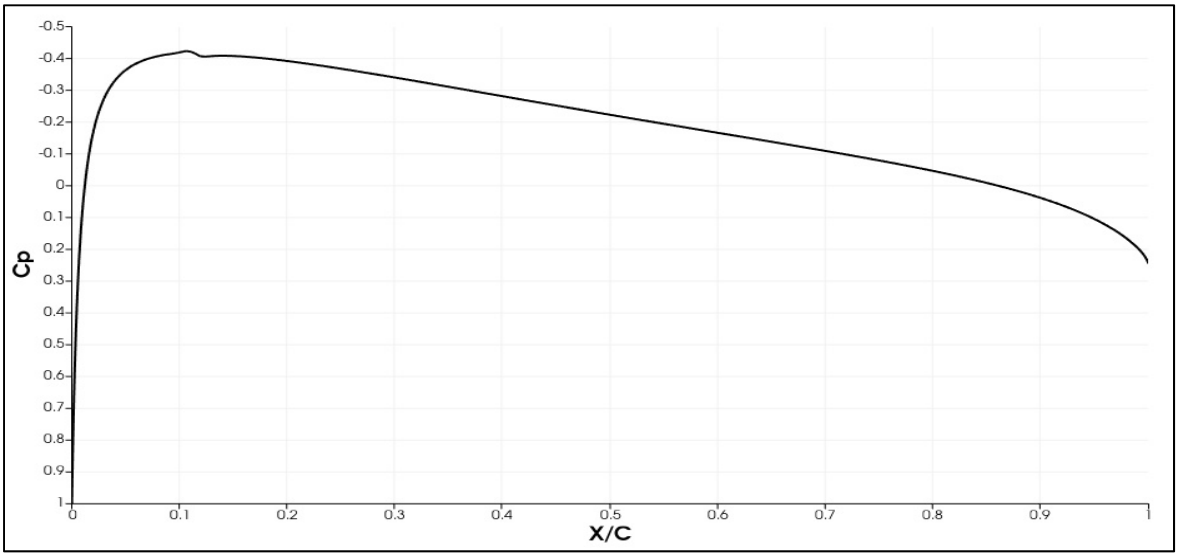

Figure 3-46 Pressure coefficient distribution over rough NACA 0012 at $Re = 2.25 \times 10^6$

Figure 3-47 compares the flow regions between rough simulation and experimental data. Although the roughness correlation does not well predict the start of the turbulent flow region, it does a good job in anticipating the onset of the transition region. As it has already been mentioned, the base model (SA-BCM) does not take the transition length into account. Due to this, the roughness model is struggling to predict the transition length and hence the onset of the turbulent flow.

Moreover, it is clear from figure 3-47 that the transition location is unaffected by the roughness length and the roughness location at higher Reynolds numbers. However, the transition length seems to decrease by increasing the roughness length. Thus, as the roughness length increases, a fully rough airfoil is having less transitional regions.

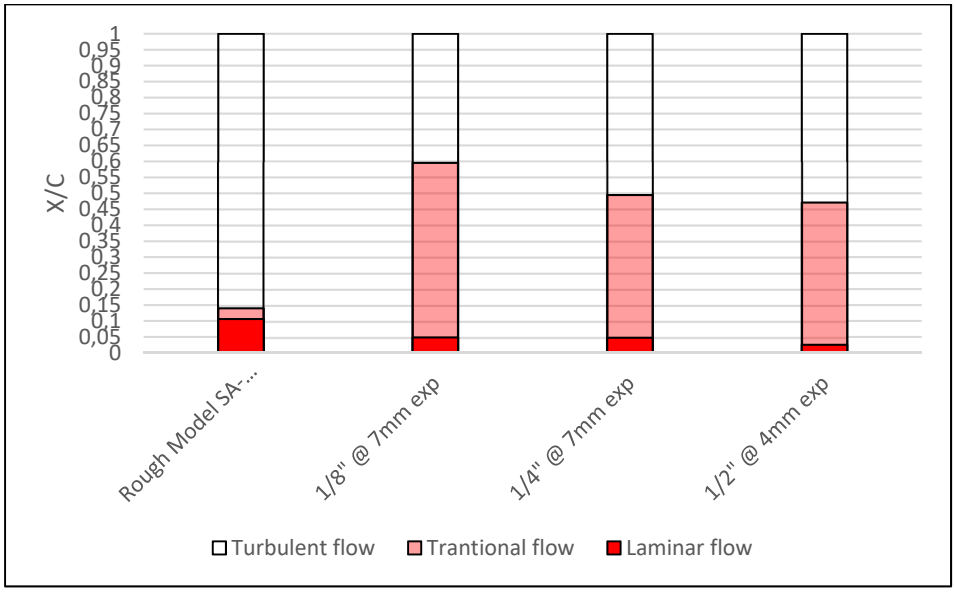

Figure 3-47 Comparison of the flow regions over rough NACA 0012 with the experimental data at $Re = 2.25 \times 10^6$

3.4 Summary

First, the results obtained with the SU2 source code changes to overcome the Galilean invariancy of the SA-BCM model were presented to ensure that the transition model is working

properly. In the next step, the model has been calibrated against a zero-pressure gradient flat plate and the outcomes of the roughness correlation calibration were shown. Figures have shown that the roughness correlation has been successfully calibrated and implemented into the SU2 source code. Finally, the roughness correlation has been validated at two Reynolds numbers ($Re = 1.25 \times 10^6$ and 2.25×10^6) over the NACA 0012 airfoil. Plots have shown that the model does not struggle with convergence. However, it was clear that the model has problem to predict the transitional length. The lack of a parameter to take the transitional length into account in the base model has been reported to be the reason for this shortcoming. Overly, the roughness correlation predicts the onset of the transition location. However, some parameters need to be recalibrated or introduced in the underlying model to overcome the transitional length issue.

CONCLUSION

In this thesis, a correlation to take the surface roughness into account is proposed and validated against a flat plate and a NACA 0012 airfoil. It is started by defining the icing and the problems it caused on the aircraft. The importance of this problem in the aviation industry is discussed. In the literature review chapter, we covered some of the researches that have been done in understanding the transition process. Additionally, some of the RANS-based numerical models to predict the transition point are studied and the main feature of each model is highlighted. In the third section of the literature review chapter, the effect of the surface roughness such as ice over on the transition process and the boundary layer is explained. This is followed by an overview of the available numerical models which take the roughness into account. The Spalart-Allmaras (SA) turbulence model has been introduced as one of the robust RANS numerical models for simulating the turbulent flow. This model is further developed to capture the transition point over smooth surfaces without solving any extra transport equation. However, in these researches, the lack of a model to capture the transition point over rough surfaces is determined and it motivated us to further develop the above-mentioned model.

By reading the related literature similar methodology is used here as the previous researchers used to develop the transition models over rough surfaces. Since the underlying transition model is correlation-based, it is decided to mimic the transition points using the experimental data and build a new correlation that can be activated over the rough surfaces to predict the transition onset location. This has been done by using a flat plate as the reference. After calibrating the model, the roughness correlation was able to successfully trigger the transition process based on the equivalent sand grain roughness height over a rough flat plate.

The NACA 0012 airfoil has been chosen to validate the roughness correlation. The validation is done using the same geometry and two Reynolds numbers. First, for the Reynolds number of $Re = 1.25 \times 10^6$, the model was able to set the transition point in between the transition region compared to the experimental and other CFD results. However, it was unable to exactly predict the transition onset location and also the end of the transition region. This has been

found to be an issue with the underlying model since there is no extra parameter for the transition length compared to the other CFD models. Additionally, correlation-based transition models are sensitive to the turbulence intensity and since the underlying turbulent model does not calculate the local turbulence intensity, free-stream turbulence intensity as an input by the user is used in both underlying and current models. In other words, applying the free-stream turbulence intensity instead of a locally calculated one can cause an error in the onset of the transition process. Second validation is done for a $Re = 2.25 \times 10^6$ over the same geometry. Using a higher Reynolds number, caused the transition point to move upstream. Similar to the previous result, the model was able to predict the transition point among the transition region compared to the experimental data. However, due to the above-mentioned issues, it had difficulty locating the exact transition point and length.

From the author's point of view, future studies could be done about the following subjects:

- The proposed model needs to be validated against more experimental data from different geometries. This will certainly always be the case, given the fact that the model is based on experimental data.
- Improving the model by defining and calibrating a transition length parameter in the base transition model, to be enabled whenever surface roughness is expected.
- Coupling the model with SA turbulent model with roughness and validating the model with aerodynamic parameters of an airfoil such as lift and drag coefficients at different angles of attack. This could potentially build a model which can be used to predict the ice accretion.

LIST OF BIBLIOGRAPHICAL REFERENCES

Abu-Ghannam, B. J., & Shaw, R. (1980). Natural Transition of Boundary Layers—The Effects of Turbulence, Pressure Gradient, and Flow History. *Journal of Mechanical Engineering Science, 22*(5), 213-228. doi:http://doi.org/10.1243/jmes_jour_1980_022_043_02

Acarlar, M., & Smith, C. (1987). A study of Hairpin Vortices in a Laminar Boundary Layer. Part 1. Hairpin vortices generated by a hemisphere protuberance. *Journal of Fluid Mechanics, 175*, 1-41. doi:http://doi.org/10.1017/S0022112087000272

AOPA. (2008). Safety Advisor. *Weather, 88*, 2842. Retrieved from https://www.faasafety.gov/files/events/GL/GL17/2014/GL1758840/sa11-Icing.pdf

Aupoix, B. (2014). Roughness Corrections for the k–ω Shear Stress Transport Model: Status and Proposals. *Journal of Fluids Engineering, 137*(2). doi:https://doi.org/10.1115/1.4028122

Aupoix, B., & Spalart, P. (2003). Extensions of the Spalart–Allmaras Turbulence Model to account for Wall Roughness. *International Journal of Heat and Fluid Flow, 24*(4), 454-462. doi:https://doi.org/10.1016/S0142-727X(03)00043-2

Blazek, J. (2015). *Computational Fluid Dynamics: Principles and Applications* (Third edition ed.). Oxford, U.K.: Butterworth-Heinemann.

Çakmakçıoğlu, S. C., Bas, O., & Kaynak, U. (2018). A Correlation-based Algebraic Transition Model. *Proceedings of the Institution of Mechanical Engineers, Part C: Journal of Mechanical Engineering Science, 232*(21), 3915-3929. doi:https://doi.org/10.1177/0954406217743537

Cao, Y., Tan, W., & Wu, Z. (2018). Aircraft icing: An ongoing Threat to Aviation Safety. *Aerospace science and technology, 75*, 353-385. doi:https://doi.org/10.1016/j.ast.2017.12.028

Cao, Y., Wu, Z., Su, Y., & Xu, Z. (2015). Aircraft Flight Characteristics in Icing Conditions. *Progress in Aerospace Sciences, 74*, 62-80. doi:https://doi.org/10.1016/j.paerosci.2014.12.001

Cho, J. R., & Chung, M. K. (1992). A K-ε-γ Equation Turbulence Model. *Journal of Fluid Mechanics, 237*, 301-322. doi:http://doi.org/10.1017/S0022112092003422

Cole, J., & Sand, W. (1991). *Statistical Study of Aircraft Icing Accidents*. Paper presented at the 29th Aerospace Sciences Meeting, Reno, NV, U.S.A.

Corke, T. C., Bar-Sever, A., & Morkovin, M. V. (1986). Experiments on Transition Enhancement by Distributed Roughness. *Physics of Fluids, 29*(10), 3199-3213. doi:https://doi.org/10.1063/1.865838

Dassler, P., Kozulovic, D., & Fiala, A. (2012). *An Approach for Modelling the Roughness-induced Boundary Layer Transition using Transport Equations*. Paper presented at the Europ. Congress on Comp. Methods in Appl. Sciences and Engineering, ECCOMAS, Vienna, Austria.

Dassler, P., Kozulovic, D., & Fiala, A. (2010). *Modelling of Roughness-induced Transition using Local Variables.* Paper presented at the V European Conference on CFD, ECCOMAS CFD, Lisbon, Portugal.

De Brito Siqueira Tagawa, G. (2021). *CFD Investigation of Iced-wing Performance Degradation using DDES with the Spalart-Allmaras Extension to Consider Roughness Effects.* (PhD). École de technologie supérieure. Retrieved from http://espace.etsmtl.ca/2721/1/DE_BRITO_SIQUEIRA_TAGAWA_Gitsuzo.pdf

Dhawan, S., & Narasimha, R. (1958). Some Properties of Boundary Layer Flow during the Transition from Laminar to Turbulent Motion. *Journal of Fluid Mechanics, 3*(4), 418-436. doi:http://doi.org/10.1017/S0022112058000094

Dirling, J., R. (1973). *A Method for Computing Roughwall Heat Transfer Rates on Reentry Nosetips*. Paper presented at the 8th Thermophysics Conference, Palm Springs, CA, U.S.A. doi: https://doi.org/10.2514/6.1973-763

Drela, M., & Giles, M. B. (1987). Viscous-inviscid Analysis of Transonic and Low Reynolds number Airfoils. *AIAA Journal, 25*(10), 1347-1355. doi:https://doi.org/10.2514/3.9789

Dryden, H. L. (1958). Combined Effects of Turbulence and Roughness on Transition. *Zeitschrift für angewandte Mathematik und Physik ZAMP, 9*(5), 249-258. doi:https://doi.org/10.1007/BF02424749

Economon, T. D., Palacios, F., Copeland, S. R., Lukaczyk, T. W., & Alonso, J. J. (2016). SU2: An Open-Source Suite for Multiphysics Simulation and Design. *AIAA Journal, 54*(3), 828-846. doi:https://doi.org/10.2514/1.J053813

Elsner, W., & Warzecha, P. (2013). Numerical Study of Transitional Rough Wall Boundary Layer. *Journal of Turbomachinery, 136*(1). doi:https://doi.org/10.1115/1.4023467

Ergin, F. G., & White, E. B. (2006). Unsteady and Transitional Flows Behind Roughness Elements. *AIAA Journal, 44*(11), 2504-2514. doi:https://doi.org/10.2514/1.17459

Feindt, E. G. (1957). *Untersuchungen über die Abhängigkeit des Umschlages laminar-turbulent von der Oberflächenrauhigkeit und der Druckverteilung.* Technische Hochschule Carolo-Wilhelmina zu Braunschweig,

Gregory, N., & Walker, W. (1956). *The effect on transition of isolated surface excrescences in the boundary layer*. London, U.K, Retrieved from: https://citeseerx.ist.psu.edu/viewdoc/download?doi=10.1.1.226.8010&rep=rep1&type=pdf

Hall, D. J., & Gibbings, J. C. (1972). Influence of Stream Turbulence and Pressure Gradient upon Boundary Layer Transition. *Journal of Mechanical Engineering Science, 14*(2), 134-146. doi:https://doi.org/10.1243/jmes_jour_1972_014_019_02

Hellsten, A., & Laine, S. (1998). Extension of $k-\omega$ Shear-Stress Transport Turbulence Model for Rough-Wall Flows. *AIAA Journal, 36*(9), 1728-1729. doi:https://doi.org/10.2514/2.7543

Kendall, J. M. (1990). *The Effect of Small-Scale Roughness on the Mean Flow Profile of a Laminar Boundary Layer*, New York, NY, U.S.A. doi:https://doi.org/10.1007/978-1-4612-3430-2_35

Kerho, M. F., & Bragg, M. B. (1997). Airfoil Boundary-Layer Development and Transition with Large Leading-Edge Roughness. *AIAA Journal, 35*(1), 75-84. doi:https://doi.org/10.2514/2.65

Klebanoff, P. S., & Tidstrom, K. D. (1972). Mechanism by Which a Two-Dimensional Roughness Element Induces Boundary-Layer Transition. *Physics of Fluids, 15*(7), 1173-1188. doi:https://doi.org/10.1063/1.1694065

Knopp, T., Eisfeld, B., & Calvo, J. B. (2009). A new Extension for k–ω Turbulence Models to Account for Wall Roughness. *International Journal of Heat and Fluid Flow, 30*(1), 54-65. doi:https://doi.org/10.1016/j.ijheatfluidflow.2008.09.009

Langel, C. M., Chow, R., Dam, C. P. V., Rumsey, M. A., Maniaci, D. C., Ehrmann, R. S., & White, E. B. (2014). *A Computational Approach to Simulating the Effects of Realistic Surface Roughness on Boundary Layer Transition*. Paper presented at the 52nd Aerospace Sciences Meeting, National Harbor, Maryland. doi: https://doi.org/10.2514/6.2014-0234

Langel, C. M., Chow, R. C., Van Dam, C., & Maniaci, D. C. (2017). *RANS based Methodology for Predicting the Influence of Leading Edge Erosion on Airfoil Performance*: Sandia National Lab.(SNL-NM), Albuquerque, NM. (SAND-2017-11289657911). doi:https://doi.org/10.2172/1404827

Langtry, R. B., & Menter, F. R. (2005). *Transition Modeling for General CFD Applications in Aeronautics.* Paper presented at the 43rd AIAA Aerospace Sciences Meeting and Exhibit, Reno, Nevada, U.S.A. doi: https://doi.org/10.2514/6.2005-522

Langtry, R. B., & Menter, F. R. (2009). Correlation-based Transition Modeling for Unstructured Parallelized Computational Fluid Dynamics Codes. *AIAA Journal, 47*(12), 2894-2906. doi:https://doi.org/10.2514/1.42362

Mayda, E. A. (2007). *Boundary-layer Transition Prediction for Reynolds-averaged Navier-Stokes Methods.* (PhD). University of California, Davis, Retrieved from https://www.proquest.com/docview/304901403/fulltextPDF/8B5588F03C443E6PQ/1?accountid=27231

Mayle, R. E. (1991). The 1991 IGTI Scholar Lecture: The Role of Laminar-Turbulent Transition in Gas Turbine Engines. *Journal of Turbomachinery, 113*(4), 509-536. doi:https://doi.org/10.1115/1.2929110

Mayle, R. E., & Schulz, A. (1997). Heat Transfer Committee and Turbomachinery Committee Best Paper of 1996 Award: The Path to Predicting Bypass Transition. *Journal of Turbomachinery, 119*(3), 405-411. doi:https://doi.org/10.1115/1.2841138

Medida, S. (2014). *Correlation-based Transition Modeling for External Aerodynamic Flows.* (PhD). University of Maryland, College Park, Retrieved from https://drum.lib.umd.edu/handle/1903/15150

Menter, F. R., Esch, T., & Kubacki, S. (2002). *Transition Modelling Based on Local Variables.* Paper presented at the 5th International Symposium on Engineering Turbulence Modelling and Experiments. Mallorca, Spain. doi: https://doi.org/10.1016/B978-008044114-6/50053-3

Menter, F. R., Langtry, R. B., Likki, S. R., Suzen, Y. B., Huang, P. G., & Völker, S. (2004). A Correlation-Based Transition Model Using Local Variables—Part I: Model Formulation. *Journal of Turbomachinery, 128*(3), 413-422. doi:https://doi.org/10.1115/1.2184352

Menter, F. R., Smirnov, P. E., Liu, T., & Avancha, R. (2015). A One-equation Local Correlation-based Transition Model. *Flow, Turbulence and Combustion, 95*(4), 583-619. doi:https://doi.org/10.1007/s10494-015-9622-4

Min, S., & Yee, K. (2021). New Roughness-Induced Transition Model for Simulating Ice Accretion on Airfoils. *AIAA Journal, 59*(1), 250-262. doi:https://doi.org/10.2514/1.J059222

Mochizuki, M. (1961). Smoke Observation on Boundary Layer Transition Caused by a Spherical Roughness Element. *Journal of the Physical Society of Japan, 16*(5), 995-1008. doi:https://doi.org/10.1143/JPSJ.16.995

Morkovin, M. (1994). Transition in Open Flow Systems-a Reassessment. *Bull. Am. Phys. Soc., 39*, 1882.

Morkovin, M. V. (1969). *On the Many Faces of Transition.* Paper presented at the Viscous Drag Reduction, Dallas, TX, U.S.A. doi:https://doi.org/10.1007/978-1-4899-5579-1_1

Mura, R., & Çakmakçıoğlu, S. C. (2020). *A Revised One-Equation Transitional Model for External Aerodynamics - Part I: Theory, Validation and Base Cases*. Paper presented at the AIAA Aviation 2020 Forum, Virtual event. doi:https://arc.aiaa.org/doi/abs/10.2514/6.2020-2714

Nikuradse, J. (1950). *Laws of Flow in Rough Pipes*. U.S.A, Retrieved from: https://ntrs.nasa.gov/citations/19930093938

Palacios, F., Alonso, J., Duraisamy, K., Colonno, M., Hicken, J., Aranake, A., . . . Taylor, T. (2013). *Stanford University Unstructured (SU2): An Open-source Integrated Computational Environment for Multi-physics Simulation and Design*. Paper presented at the 51st AIAA Aerospace Sciences Meeting including the New Horizons Forum and Aerospace Exposition, Grapevine (Dallas/Ft. Worth Region), Texas. doi:https://doi.org/10.2514/6.2013-287

Prandtl, L. (1904). Über Flussigkeitsbewegung bei sehr kleiner Reibung. *Verhandl. III, Internat. Math.-Kong., Heidelberg, Teubner, Leipzig, 1904*, 484-491

Ratvasy, T., & Ranaudo, R. (1993). *Icing Effects on Aircraft Stability and Control Determined from Flight Data - Preliminary Results*. Paper presented at the 31st Aerospace Sciences Meeting, Reno, NV, U.S.A. doi:https://doi.org/10.2514/6.1993-398

Rayleigh, L. (1879). On the Stability, or Instability, of Certain Fluid Motions. *Proceedings of the London Mathematical Society, 1*(1), 57-72.

Reehorst, A., Brinker, D., & Ratvasky, T. (2005). *NASA Icing Remote Sensing System Comparisons from AIRS II*. Retrieved from https://arc.aiaa.org/doi/abs/10.2514/6.2005-253

Reshotko, E., & Leventhal, L. (1981). *Preliminary Experimental Study of Disturbances in a Laminar Boundary Layer due to Distributed Surface Roughness.* Paper presented at the 14th Fluid and Plasma Dynamics Conference, Palo Alto, CA, U.S.A. doi:https://doi.org/10.2514/6.1981-1224

Reynolds, O. (1883). XXIX. An Experimental Investigation of the Circumstances which Determine Whether the Motion of Water Shall be Direct or Sinuous, and of the Law of Resistance in Parallel Channels. *Philosophical Transactions of the Royal Society of London*(174), 935-982. doi:https://doi.org/10.1098/rstl.1883.0029

Roe, P. L. (1981). Approximate Riemann Solvers, Parameter Vectors, and Difference Schemes. *Journal of computational physics, 43*(2), 357-372. doi:https://doi.org/10.1016/0021-9991(81)90128-5

Rumsey, C. (2019). Grids - NACA 0012 Airfoil Case [online]. Retrieved from https://turbmodels.larc.nasa.gov/naca0012_grids.html

Saric, W. S., Reed, H. L., & Kerschen, E. J. (2002). Boundary-layer Receptivity to Freestream Disturbances. *Annual review of fluid mechanics, 34*, 291.

Schlichting, H. (1937). *Experimental Investigation of the Problem of Surface Roughness*: National Advisory Commitee for Aeronautics. (NACA-TM-823). Retrieved from https://ntrs.nasa.gov/citations/19930094593

Schlichting, H., & Kestin, J. (1961). *Boundary Layer Theory* (Vol. 121). New York, NY, U.S.A: Springer.

Schubauer, G. B., & Klebanoff, P. S. (1955). *Contributions on the Mechanics of Boundary-layer Transition*. (NACA-TR-1289). Retrieved from https://ntrs.nasa.gov/citations/19930092285

Schubauer, G. B., & Skramstad, H. K. (1947). Laminar Boundary-Layer Oscillations and Stability of Laminar Flow. *Journal of the Aeronautical Sciences, 14*(2), 69-78. doi:https://doi.org/10.2514/8.1267

Smith, A. M. O., & Gamberoni, N. (1956). *Transition, Pressure Gradient and Stability Theory*. (ES 26388). Retrieved from https://engineering.purdue.edu/~aae519/BAM6QT-Mach-6-tunnel/otherpapers/smith-amo-eN-douglas-es26388-1956.pdf

Spalart, P., & Allmaras, S. (1992). *A One-Equation Turbulence Model for Aerodynamic Flows*. Paper presented at the 30th Aerospace Sciences Meeting and Exhibit, Reno, NV, U.S.A. doi:https://doi.org/10.2514/6.1992-439

Spalart, P. R., & Venkatakrishnan, V. (2016). On the Role and Challenges of CFD in the Aerospace Industry. *Aeronautical Journal, 120*(1223), 209-232. doi:http://doi.org/10.1017/aer.2015.10

Steelant, J., & Dick, E. (1996). Modelling of Bypass Transition with Conditioned Navier–Stokes Equations Coupled to an Intermittency Transport Equation. *International Journal for Numerical Methods in Fluids, 23*(3), 193-220. doi:https://doi.org/10.1002/(SICI)1097-0363(19960815)23:3<193::AID-FLD415>3.0.CO;2-2

Stripf, M., Schulz, A., Bauer, H.-J., & Wittig, S. (2009). Extended Models for Transitional Rough Wall Boundary Layers With Heat Transfer—Part I: Model Formulations. *Journal of Turbomachinery, 131*(3). doi:https://doi.org/10.1115/1.2992511

Suluksna, K., & Juntasaro, E. (2008). Assessment of Intermittency Transport Equations for Modeling Transition in Boundary Layers Subjected to Freestream Turbulence. *International Journal of Heat and Fluid Flow, 29*(1), 48-61. doi:https://doi.org/10.1016/j.ijheatfluidflow.2007.08.003

Suzen, Y. B., & Huang, P. G. (2000). Modeling of Flow Transition Using an Intermittency Transport Equation. *Journal of Fluids Engineering, 122*(2), 273-284. doi:https://doi.org/10.1115/1.483255

Tagawa, G. D., Morency, F., & Beaugendre, H. (2018). *CFD Study of Airfoil Lift Reduction Caused by Ice Roughness*. Paper presented at the 2018 Applied Aerodynamics Conference, Atlanta, Georgia. doi:https://doi.org/10.2514/6.2018-3010

Van Ingen, J. (1956). *A Suggested Semi-Empirical Method for the Calculation of the Boundary Layer Transition Region*. (VTH-74) Retrieved from http://resolver.tudelft.nl/uuid:cff1fb47-883f-4cdc-ad07-07d264f3fd10

Van Leer, B. (1979). Towards the Ultimate Conservative Difference Scheme. V. A Second-Order Eequel to Godunov's Method. *Journal of computational physics, 32*(1), 101-136. doi:https://doi.org/10.1016/0021-9991(79)90145-1

Walters, D. K., & Cokljat, D. (2008). A Three-Equation Eddy-Viscosity Model for Reynolds-Averaged Navier–Stokes Simulations of Transitional Flow. *Journal of Fluids Engineering, 130*(12). doi:https://doi.org/10.1115/1.2979230

Walters, D. K., & Leylek, J. H. (2004). A New Model for Boundary Layer Transition Using a Single-Point RANS Approach. *Journal of Turbomachinery, 126*(1), 193-202. doi:https://doi.org/10.1115/1.1622709

White, F., & Majdalani, J. (2006). *Viscous Fluid Flow* (Vol. 3). New York, NY, U.S.A.

Wilcox, D. C. (1988). Multiscale Model for Turbulent Flows. *AIAA Journal, 26*(11), 1311-1320. doi:https://doi.org/10.2514/3.10042

Wilcox, D. C. (1993). Comparison of Two-Equation Turbulence Models for Boundary Layers with Pressure Gradient. *AIAA Journal, 31*(8), 1414-1421. doi:https://doi.org/10.2514/3.11790